

Methods for the Detection of the Epoch of Reionization
by Interferometers Measuring the 21 cm Signal

By

Carina Cheng

A dissertation submitted in partial satisfaction of the

requirements for the degree of

Doctor of Philosophy

in

Astrophysics

in the

Graduate Division

of the

University of California, Berkeley

Committee in charge:

Professor Aaron Parsons, Chair

Professor Stuart Bale

Professor Mariska Kriek

Spring 2019

Methods for the Detection of the Epoch of Reionization
by Interferometers Measuring the 21 cm Signal

Copyright 2019
by
Carina Cheng

Abstract

Methods for the Detection of the Epoch of Reionization by Interferometers Measuring the 21 cm Signal

by

Carina Cheng

Doctor of Philosophy in Astrophysics

University of California, Berkeley

Professor Aaron Parsons, Chair

The Epoch of Reionization is one of the last unexplored eras of our Universe's history. Beginning about a billion years after the Big Bang, this epoch is characterized by the births of the first stars and galaxies, whose light subsequently altered the nature of the gas surrounding them. There are several experiments aiming to detect the phase transition of this gas as it changes from neutral hydrogen to ionized hydrogen. Such a detection would open a wealth of information about our early Universe, revealing details about the nature of the first luminous sources and the evolution of structure formation.

Interferometers such as the Precision Array for Probing the Epoch of Reionization (PAPER) and the Hydrogen Epoch of Reionization Array (HERA) seek to measure the 21 cm signal from neutral hydrogen and map its evolution over spatial and temporal scales. A successful detection of reionization, however, is a difficult measurement. Though the 21 cm signal is a powerful topological probe of the intergalactic medium, it is easily buried underneath bright foreground signals and instrumental systematics. A clean detection of reionization is ambitious and requires analysis methods that maximize data sensitivity and increase confidence in results.

The work presented in this thesis addresses many of the key challenges that face the current field of 21 cm cosmology. This includes algorithms to locate contaminated data, methods to ensure accurate power spectrum measurements, and techniques for removing unwanted systematics while preserving the reionization signal. These developments serve as the foundation of the latest 21 cm measurements from the PAPER-64 and PAPER-128 arrays, whose results lie at the forefront of the field. These methods are also fundamental to HERA and future experiments, as they provide a strong foundation for the continued exploration of our cosmic dawn.

to my parents

Contents

List of Figures	iv
List of Tables	ix
Acknowledgments	x
1 Introduction	1
1.1 The Epoch of Reionization	1
1.1.1 Cosmic History	1
1.1.2 CMB and Galaxy Measurements	2
1.1.3 Measurements of HI	4
1.1.4 This Thesis	8
1.2 Interferometry	8
1.2.1 The Visibility Equation	8
1.2.2 The 21 cm Power Spectrum	9
1.2.3 Calibration	10
1.2.4 Foreground Filtering	12
1.2.5 Fringe-rate Filtering	14
1.3 Instruments	14
1.3.1 The Precision Array for Probing the Epoch of Reionization	15
1.3.2 The Hydrogen Epoch of Reionization Array	17
1.3.3 Other Experiments and Status of Field	19
2 Power Spectrum Methods	22
2.1 Power Spectrum Themes and Techniques	22
2.2 Signal Loss Toy Model	25
2.2.1 The Quadratic Estimator Method	25
2.2.2 Empirical Inverse Covariance Weighting	28
2.2.3 Fringe-Rate Filtering	32
2.2.4 Other Weighting Options	36
2.3 Signal Loss Mathematical Framework	39
2.3.1 A Toy Model for Inverse Covariance Weighting	40

2.3.2	A Toy Model for Signal Loss	41
2.4	Error Estimation Toy Model	43
2.5	Bias Toy Model	46
2.5.1	Foreground and Noise Bias	47
2.5.2	Jackknife Tests	48
3	PAPER-64 Case Study	52
3.1	Overview	52
3.1.1	Observations	52
3.1.2	Data Processing	53
3.1.3	Case Study Data	54
3.2	Signal Loss	55
3.3	Error Estimation	55
3.4	Bias	55
4	PAPER-64 Results	57
5	PAPER-128	58
5.1	Overview	58
5.2	Quality Assurance	59
5.2.1	Flagging Julian Dates	60
5.2.2	Flagging Antennas	62
5.3	Data Processing	65
5.4	Power Spectrum Limits	67
6	HERA	70
7	Conclusion	71
	Bibliography	72

List of Figures

1.1	Timeline of the history of the Universe. The Epoch of Reionization marks the era when the first stars and galaxies formed and ionized the neutral hydrogen in the Universe. Image credit: NAOJ.	2
1.2	A cartoon diagram of the observable Universe, centered on us. Close-by, galaxy observations have mapped out cosmic web structure in our nearby Universe (image credit: SDSS). Far-away, the cosmic microwave background is observed at a redshift of $z \sim 1100$ (image credit: WMAP). The Epoch of Reionization represents a largely unexplored era between the two, and can be probed by measuring red-shifted 21 cm radiation from neutral hydrogen.	5
1.3	The evolution of the global 21 cm signal, starting with the Dark Ages, through galaxy formation and reionization (image credit: Pritchard & Loeb (2012)). The work in this thesis mainly focuses on a redshift range of $6 < z < 12$ when reionization is expected to progress and complete.	6
1.4	The theoretical evolution of the cross-21 cm power spectrum for a specific model (image credit: Barkana (2009)), where the neutral fraction $x_{HI} = 10\%, 30\%, 50\%, 70\%, 90\%$, and 98% from top to bottom at large k . This figure shows the expected evolution of the power spectrum which interferometers seek to measure.	11
1.5	A cartoon diagram of the “EoR Window” and “wedge” of foreground contamination in Fourier space (image credit: Dillon et al. (2015b)). A foreground avoidance approach makes power spectrum measurements in the window, while a foreground subtraction approach subtracts out foregrounds so that measurements can be made in the wedge. The overall power spectrum measurement space is limited by an interferometer’s field of view and angular resolution along the horizontal axis, and spectral resolution and intrinsic foregrounds along the vertical axis.	13
1.6	A PAPER antenna in the Karoo Desert in South Africa. A dual-polarization dipole sits at the center, surrounded by wire mesh panels that measure 2 m on each side.	16

1.7	A HERA dish in the Karoo Desert in South Africa. Wire-mesh, PVC pipes, and wooden structures serve as the foundation for the 14 m diameter parabola. A PA-PER dipole is suspended upside-down with a wire pulley-system and surrounded by a prototype wire-mesh skirt structure. HERA-350 will use an updated design for its feed; however, HERA’s initial data releases use the old PAPER infrastructure as depicted here.	18
1.8	The full HERA-350 array (image credit: DeBoer et al. (2017)). The array is comprised of a segmented densely-packed core (to optimize redundancy for a foreground avoidance approach) and surrounding outrigger elements (for imaging capabilities).	18
1.9	Published upper limits on the EoR placed by different 21 cm experiments, prior to the work in this thesis. All PAPER results shown (PAPER-32 is in cyan and magenta, and PAPER-64 is in gray) are suspect to the errors discussed throughout this work and are superseded by the ones presented in Chapter 3.	20
2.1	Our toy model dataset to which we apply different weighting schemes to in order to investigate signal loss. We model a mock foreground-only visibility with a sinusoid signal that varies smoothly in time and frequency. We model a mock visibility of an EoR signal as a random Gaussian signal. We add the two together to form $\mathbf{x} = \mathbf{x}_{\text{FG}} + \mathbf{x}_{\text{EoR}}$. Real parts are shown here.	29
2.2	The estimated covariance matrices (top row) and inverse covariance-weighted data (bottom row) for FG only (left), EoR only (middle), and FG + EoR (right). Real parts are shown here.	30
2.3	Resulting power spectrum estimates for the toy model simulation described in Chapter 2.2.2 — foregrounds only (blue), EoR only (red), and the weighted FG + EoR dataset (green). The power spectrum of the foregrounds peaks at a k -mode based on the frequency of the sinusoid used to create the mock FG signal. In the two panels, we compare using empirically estimated inverse covariance weighting where \mathbf{C} is derived from the data (left), and projecting out the zeroth eigenmode only (right). In the former case, signal loss arises from the coupling of the eigenmodes of $\hat{\mathbf{C}}$ to the data. There is negligible signal loss when all eigenmodes besides the foreground one are no longer correlated with the data.	31
2.4	The convergence level, as defined by Equation (2.12), of empirically estimated covariances of mock EoR signals with different numbers of independent samples. In red, the mock EoR signal is comprised entirely of independent samples (100 of them). Subsequent colors show time-averaged signals. As the number of realizations increases, we see that the empirical covariances approach the true covariances. With more independent samples, the quicker an empirical covariance converges (i.e., the quicker it decouples from the data), and the less signal loss we would expect to result.	34

2.5	The convergence level, as defined by Equation (2.13), of empirically estimated eigenvectors for different numbers of mock data realizations. The colors span from the 0th eigenmode (has the highest eigenvalue) to the 19th eigenmode (has the lowest eigenvalue), where they are ordered by eigenvalue in descending order. This figure shows that the zeroth eigenmode converges the quickest, implying that eigenvectors with eigenvalues that are substantially different than the rest (the FG-dominated mode has a much higher eigenvalue than the EoR modes) are able to converge to the true eigenvectors the quickest. On the other hand, eigenmodes 1-19 have similar eigenvalues and are slower to converge because of degeneracies between them.	35
2.6	Our “fringe-rate filtered” (time-averaged) toy model dataset. We average every four samples together, yielding 25 independent samples in time. Real parts are shown here.	35
2.7	Resulting power spectrum estimate for the “fringe-rate filtered” (time-averaged) toy model simulation — foregrounds only (blue), EoR only (red), and the weighted FG + EoR dataset (green). We use empirically estimated inverse covariance weighting where \mathbf{C} is computed from the data. There is a larger amount of signal loss than for the non-averaged data, a consequence of weighting by eigenmodes that are more strongly coupled to the data due to there being fewer independent modes in the data.	37
2.8	Resulting power spectra estimates for our “fringe-rate filtered” (time-averaged) toy model simulation — foregrounds only (blue), EoR only (red), and the weighted FG + EoR dataset (green). We show four alternate weighting options that each minimize signal loss, including modeling the covariance matrix of EoR (upper left), regularizing $\widehat{\mathbf{C}}$ by adding an identity matrix to it (upper right), using only the first three eigenmodes of $\widehat{\mathbf{C}}$ (lower left), and keeping only the diagonal elements of $\widehat{\mathbf{C}}$ (lower right). The first case (upper left) is not feasible in practice since we do not know \mathbf{C}_{FG} and \mathbf{C}_{EoR} like we do in the toy model.	38
2.9	Error estimation from bootstrapping as a function of the number of elements drawn per bootstrap when sampling with replacement. The star represents the standard deviation of $N_{\text{boot}} = 500$ bootstraps, each created by drawing 1000 elements (with replacement) from a length 1000 array of a Gaussian random signal. The black points correspond to time-averaged data (correlated data) which has 100 independent samples. They illustrate how errors can be under-estimated if drawing more elements than there are independent samples in the data. The estimated errors match up with the theoretical prediction only at $N = 100$	45
2.10	A null jackknife test shown as the power spectrum difference between two measurements (black), compared to the power spectrum of noise alone (green). Because the null test is not consistent with noise, it suggests the presence of a systematic in either \mathbf{x}_1 or \mathbf{x}_2 . Null tests of clean measurements should be consistent with thermal noise.	50

2.11 Power spectrum estimates for \mathbf{x}_1 and \mathbf{x}_2 , two jackknives of the toy model. They suggest the presence of a systematic in \mathbf{x}_2 only, illustrating how jackknives can be used to tease out excesses. Clean measurements should remain consistent despite the jackknife taken.	50
3.1 The PAPER-64 antenna layout. We use only 10 of the 30 m East/West baselines for the analysis in this chapter (i.e., a subset of the shortest horizontal spacings).	53
3.2 Top: the normalized optimal power-spectrum sensitivity weighting in fringe-rate space for our fiducial baseline and Stokes I polarization beam. Bottom: the time domain convolution kernel corresponding to the top panel. Real and imaginary components are illustrated in cyan and magenta, respectively, with the absolute amplitude in black. The fringe-rate filter acts as an integration in time, increasing sensitivity but reducing the number of independent samples in the dataset.	56
5.1 The PAPER-128 antenna layout. There are 112 antennas arranged in a grid layout which are used for power spectrum analyses. The addition of 16 outrigger antennas is used to increase <i>uv</i> -plane sampling for imaging analyses.	59
5.2 Visibility amplitudes as a function of LST for different Julian days of data (colors). The left column shows the data before (top) and after (bottom) the flagging of outlier days for Epoch 1. The right column shows similar data for Epoch 2. After flagging, visibilities show good day-to-day agreement across an epoch.	61
5.3 Waterfall plots of visibility amplitudes for a “good” reference day (left) in Epoch 2 and “bad” day (right). We exclude corrupted data for specific days found with our metric.	62
5.4 Waterfall plots of visibility amplitudes for four different polarizations and two different baselines. Antenna 26 is found to be cross-polarized because its feed was rotated by 90 degrees, and hence its “X” and “Y” polarization states are mislabeled. Equation (5.2) captures visibility amplitudes like the ones shown here in order to automatically detect cross-polarized antennae.	63
5.5 Flagged antennas, found using Equation (5.1), are marked in black for each antenna number (x-axis) and Julian date (y-axis). The left column shows flags for XX polarization, and the right column shows flags for YY polarization. The top row shows flags for Epoch 1 and the bottom row shows flags for Epoch 2. We remove antennas that are flagged greater than 50% of the time per epoch.	64
5.6 <code>FirstCal</code> phase solutions for Antenna 1 (Epoch 1, XX polarization) where no antennas are flagged (top left) and some antennas are flagged (via the methods described in Chapter 5.2.2, top right). Omnical χ^2 results are also shown for the two cases (bottom). We do not include any of the 16 dead antennas associated with correlator FX2. It is crucial to flag misbehaving antennas (especially extreme outlier antennas) prior to redundant calibration, motivating the development of automated quality assessment tools prior to the post-processing of data.	66

- 5.7 Power spectrum results for PAPER-128 season 1 data for two redshifts (rows) and two epochs (columns), using one baseline separation-type only (30 m East/West baselines). Black and gray points represent positive and negative power spectrum values, respectively, with 2σ error bars determined from bootstrapping. The 2σ theoretical noise sensitivity prediction is shown in green. Gray shaded regions correspond to theoretical errors on each data point. 69

List of Tables

5.1 An overview of the PAPER-128 data used for power spectrum analysis in this thesis.	60
--	----

Acknowledgments

This thesis may be filled with new scientific methods, exciting astronomical insights, and technical jargon. But what it doesn't capture, is what I'm most proud of — the life lessons I've learned about what it means to be a scientist, what it means to do good science, and how to learn and preservere despite challenges. For that, I must thank many people.

Chapter 1

Introduction

1.1 The Epoch of Reionization

Our Universe has a complex, rich history, of which enormous progress has been made in the past few decades to unravel its story. Much has been learned about the very beginnings of the Universe, from the Big Bang's large explosion of energy to the relatively smooth and simple cosmic background radiation that was leftover. Additionally, observational feats have revealed the status of the present-day Universe and the intricate *cosmic web*, or large scale structure, of galaxies today.

The Epoch of Reionization (EoR) ties these two bookends together, occurring about a billion years after the Big Bang when the very first stars and galaxies formed. How did the tiny density fluctuations from the cosmic microwave background develop into the structure we see today? How did the first luminous structures form, and how did they evolve and influence the gas around them? Exploring the reionization era opens up a new chapter of our Universe's story - a chapter that promises to connect the dots between our past and present.

1.1.1 Cosmic History

As the Universe expanded and cooled after the Big Bang, electrons and protons eventually combined to form neutral hydrogen atoms. At the young age of $\sim 380,000$ years, the Universe's ordinary baryonic content was almost entirely neutral hydrogen, while most of its total matter was dark matter ([Loeb & Furlanetto 2013](#)). Then, for the next several hundred million years, the *Dark Ages* proceeded, with concentrations of dark matter setting the foundations for the formation of the first luminous structures. More specifically, the tiny, primordial density fluctuations that were established at the release of the CMB grew with inflation and the expansion of the Universe. The densest regions then collapsed to form dark matter halos, inside of which hydrogen gas could cool, condense, and fragment into stars ([Dodelson 2003](#)).

The first luminous structures are thought to have formed at an age of ~ 200 million

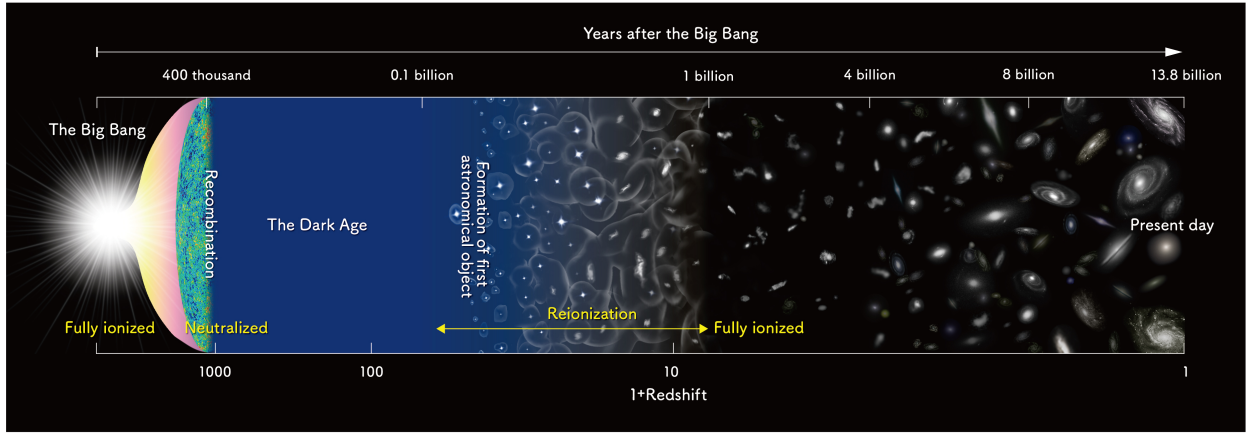


Figure 1.1: Timeline of the history of the Universe. The Epoch of Reionization marks the era when the first stars and galaxies formed and ionized the neutral hydrogen in the Universe. Image credit: NAOJ.

years ($z \sim 20$) and are predicted to have been massive stars with high luminosities and large ionizing powers (Loeb & Furlanetto 2013). The ionizing photons from the first stars carved out pockets of ionized hydrogen gas around the densest, most massive dark matter halos, and as the number of sources grew, an increased number of ionized bubbles emerged and overlapped. Eventually, the first generations of stars and galaxies succeeded in ionizing most all of the neutral hydrogen in the Universe, with reionization complete by about one billion years after the Big Bang ($z \sim 6$) (Furlanetto et al. 2006).

The exact timescale and details of the reionization process, which are shown within the context of the history of the Universe in Figure 1.1, are current research questions in the field of cosmology. The physics of reionization depends on several factors, including the nature of the first stars (masses, luminosities, ionizing photons) and the surrounding gas (efficiency of the ionizing photons, feedback effects). Turning the argument around, deep investigations of the reionization era would lead to new understandings about the properties of the first stars and the intergalactic medium (IGM). There are several ways to approach the study of this epoch, with CMB measurements working to constrain the duration of reionization, galaxy measurements unveiling the end of reionization, and direct hydrogen measurements attempting to map out the changing nature of the gas over time. All of these probes serve to illuminate this watershed era between a Universe dominated by darkness and a Universe defined by light.

1.1.2 CMB and Galaxy Measurements

There are several observational probes of the reionization epoch, and we highlight two broad categories in this section. The first is the study of CMB anisotropies, which carry with them an imprint of the early Universe from the time of its release. But that's not the only

imprint it has - CMB photons can scatter off of free electrons after reionization, and these scatterings leave behind polarization and temperature imprints (Haiman & Knox 1999). For example, the amplitude of the CMB is sensitive to scatterings, as an increased number of scatterings is akin to mixing different parts of the CMB together as photons are scattered in all directions. In other words, this scattering washes out anisotropies in the CMB and lowers its overall amplitude.

A useful parameter to quantify the amount of electron scattering that occurs is the optical depth, τ_{es} , defined as:

$$\tau_{es} = \int n_e \sigma_T dl, \quad (1.1)$$

where n_e is the number density of free electrons, σ_T is the Thompson cross-section, and the integral is taken over a proper length dl . Once reionization begins, the number of free electrons increases, contributing to increasingly higher values of τ_{es} . Hence, an earlier start for reionization would yield higher optical depths than a late reionization scenario.

Observations of the CMB by WMAP and Planck have placed constraints on the optical depth parameter (Hinshaw et al. 2013; Planck Collaboration et al. 2016), with the more recent Planck result suggesting a value of $\tau_{es} \sim 0.07$. This value suggests that reionization ends at a redshift of $z \sim 6$, with instantaneous reionization (“mean” reionization) at $z \sim 8.8$ (Planck Collaboration et al. 2016).

Currently, the results from CMB measurements are in agreement with a second powerful probe of EoR — broadly speaking, that of galaxy observations. This probe comes in many flavors. For example, the spectra of distant quasars at high redshifts can illuminate the end of reionization. Quasars, being extraordinarily bright and energetic objects, are detectable at very far distances and their spectra reveal the amount of absorption their light has undergone due to neutral hydrogen. While nearby quasar spectra exhibit sharp absorption lines, distant ones show the Gunn-Peterson trough, implying that the quasar light was entirely suppressed by hydrogen absorption (i.e., neutral hydrogen existed). Studying the absorption features of quasars at different redshifts implies that reionization has indeed ended by $z \sim 6$ (Becker et al. 2001).

In addition to quasar observations, high-redshift galaxy observations can also reveal important characteristics about the state of the IGM. Namely, distant star-forming galaxies can be detected using a variety of techniques, such as narrow-band imaging to find Lyman- α emitters (radiation that is produced by recombination near young stars) or broad-band observations to find Lyman-break galaxies (spectral breaks associated with absorption by neutral hydrogen). High-redshift galaxy observations can then be used to construct luminosity functions (number of stars per luminosity interval) and star formation histories, which in turn impact the evolution of the IGM.

More specifically, if star-forming galaxies dominated the reionization process, then the ionization rate can be related to the following star-formation parameters:

$$\dot{n}_{\text{ion}} = f_{\text{esc}} \xi_{\text{ion}} \rho_{\text{SFR}}, \quad (1.2)$$

where \dot{n}_{ion} is the cosmic ionization rate, f_{esc} is the escape fraction of photons into the IGM, ξ_{ion} is the rate of production of ionizing photons for a stellar population, and ρ_{SFR} is the star formation rate density. All three parameters influence the rate at which the IGM is ionized, and the star formation rate density is able to be constructed from galaxy luminosity functions. For example, [Robertson et al. \(2015\)](#) used data from the Hubble Space Telescope to construct a star formation rate history out to high redshifts, backing out an optical depth parameter that is consistent with that of Planck.

While galaxy measurements can be used to constrain the EoR, they are ultimately doing so by unveiling the properties of old, distant stars and galaxies. A similar, new technique that also aims to reconstruct the histories of the first luminous structures is observing nearby, metal-poor Local Group galaxies. Called “galactic archaeology,” observations of nearby star-forming ancestors can be used to constrain the faint-end slope of the luminosity function. Determining the shape of this function has important implications on the number of galaxies needed to drive reionization and the types of sources dominating this epoch ([Weisz & Boylan-Kolchin 2017](#)). Additionally, studies of nearby metal-poor stars and galaxies can provide insight into the contents of the first generation of stars and the dynamics of high-redshift star formation, as observations of ultrafaint dwarf galaxies around the Milky Way suggest they are relatively clean tracers of the first generations of stars ([Loeb & Furlanetto 2013](#)).

Galaxy observations for reionization studies have been primarily driven by observations taken by the Hubble Space Telescope. In the coming years, the James Webb Space Telescope (JWST), a 6.5 m infrared space telescope, will be optimally primed for the detection of faint galaxies, including galaxies whose roots extend as far back as the cosmic dawn and who may exhibit signatures of first generation Population III stars. In addition to JWST, several large infrared ground telescopes are also underway, including the European Extremely Large Telescope (EELT), the Giant Magellan Telescope (GMT), and the Thirty Meter Telescope (TMT).

Although both CMB measurements and galaxy observations have much to look forward to, they currently each have their limitations. For example, CMB measurements can only reveal the integrated quantity of τ_{es} , therefore unable to provide insight into the evolution of reionization as it progresses over time. Similarly, galaxy observations are currently limited by sensitivity, able to hover only around the tail end of the reionization era. A different, but complimentary, probe is needed to unlock the entire window into the EoR.

1.1.3 Measurements of HI

A direct measurement of neutral hydrogen gas over time would provide a fundamental way to track the IGM over the reionization process. Such a probe, which is made possible by the spin-flip transition of hydrogen, is a powerful technique that allows the tracing of gas over time, and it is this technique that serves as the basis for the remainder of this thesis ([Furlanetto et al. 2006; Barkana & Loeb 2008; Morales & Wyithe 2010; Pritchard & Loeb 2010; Pritchard & Loeb 2012](#)).

The spin-flip transition of neutral hydrogen occurs when a hydrogen atom changes energy

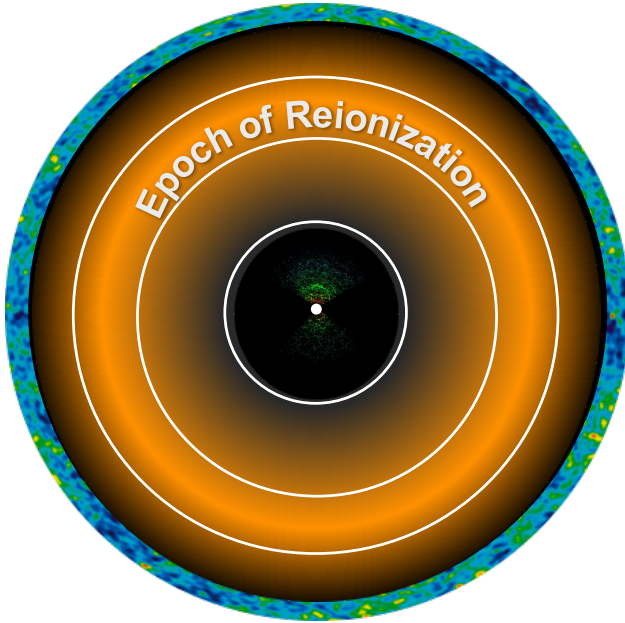


Figure 1.2: A cartoon diagram of the observable Universe, centered on us. Close-by, galaxy observations have mapped out cosmic web structure in our nearby Universe (image credit: SDSS). Far-away, the cosmic microwave background is observed at a redshift of $z \sim 1100$ (image credit: WMAP). The Epoch of Reionization represents a largely unexplored era between the two, and can be probed by measuring red-shifted 21 cm radiation from neutral hydrogen.

state between two hyperfine levels. Namely, if a hydrogen atom moves from an aligned energy state (the proton and electron have parallel spins) to an anti-aligned state (the proton and electron have antiparallel spins), the energy difference is released in the form of a photon with a wavelength of 21 cm.

Because this transition has a well-defined wavelength, the signal can be directly mapped to a distance, or redshift, by measuring its wavelength upon detection. For example, a 21 cm photon that was initially emitted at a redshift of $z = 6$ would have expanded by a factor of $(1 + z)$ due to the expansion of the Universe and be 1.5 m long when it arrives at our telescopes. Hence, observing longer wavelengths of the hydrogen signal means that it has traveled for a greater distance (and has stretched out more) and thus comes from farther away at a higher redshift. This means that the 21 cm signal is a powerful tracer of neutral hydrogen at any distance (i.e., as a function of time), as long as it exists. This technique is especially compelling because it allows the direct exploration of the EoR as reionization occurs, whereas CMB measurements and galaxy measurements surround this era from the beginning and end only, respectively (Figure 1.2).

In practice, the 21 cm signal is encapsulated by the quantity T_{spin} (spin temperature), which measures the relative number of hydrogen atoms in the excited (aligned) versus ground (anti-aligned) spin-flip state. A high spin temperature means that the hydrogen gas is more

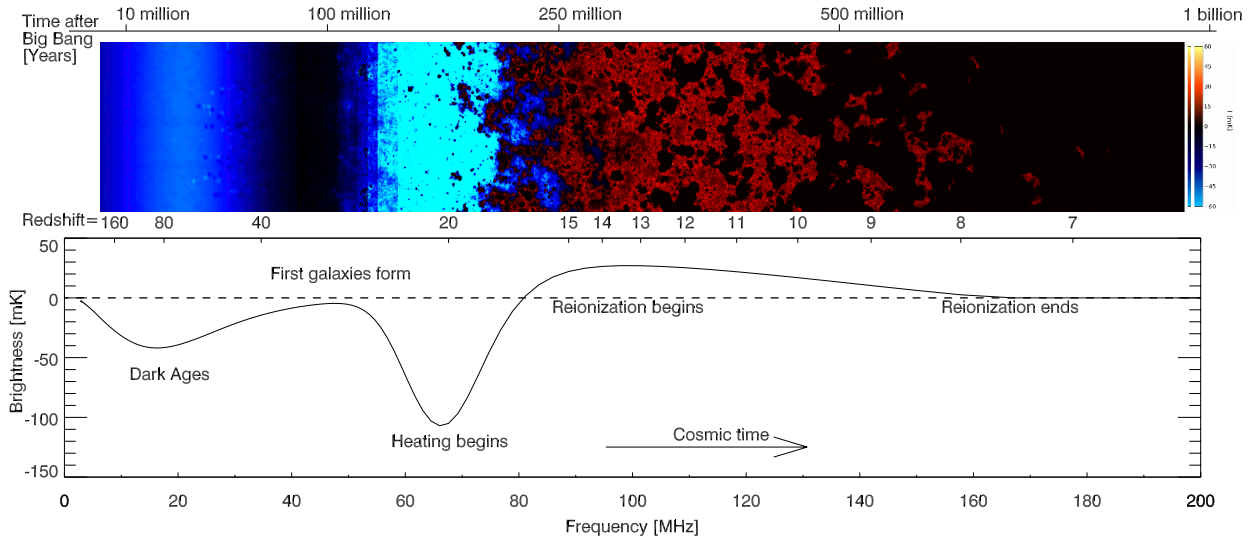


Figure 1.3: The evolution of the global 21 cm signal, starting with the Dark Ages, through galaxy formation and reionization (image credit: [Pritchard & Loeb \(2012\)](#)). The work in this thesis mainly focuses on a redshift range of $6 < z < 12$ when reionization is expected to progress and complete.

likely to emit 21 cm photons, whereas a low T_{spin} implies that the gas is more likely to absorb 21 cm photons.

The spin temperature is always measured with respect to the temperature of the CMB (T_{CMB}), which serves as a backlight for our measurement. During different stages of our cosmic history, T_{CMB} and T_{spin} take turns in the spotlight, with the *differential brightness temperature* δT_b describing their evolution:

$$\delta T_b \propto (1 + \delta_b)x_{HI} \left(1 - \frac{T_{\text{CMB}}}{T_{\text{spin}}}\right). \quad (1.3)$$

Equation (1.3) captures the EoR signal that 21 cm experiments seek to measure, where δ_b is the fractional over-density of matter and x_{HI} is the fraction of neutral hydrogen (1 if all neutral, 0 if all ionized). The differential brightness temperature can be measured in multiple ways — in Chapter 1.2 we explain how interferometry (multiple telescopes) can be used to measure the correlations of δT_b on various spatial scales on the sky. Here we describe the evolution of the sky-averaged δT_b , called the *global signal*, in order to summarize how it is expected to behave during our cosmic dawn and through reionization.

A theoretical prediction for the evolution of δT_b is shown in Figure 1.3. At the very far left, a cool, neutral IGM remains after recombination and the release of the CMB. Residual electrons collide off of both CMB photons and the hydrogen gas, driving couplings between T_{gas} and T_{CMB} , and T_{gas} and T_{spin} , respectively. Hence, we expect to see no signal ($\delta T_b = 0$) at this time.

During the Dark Ages, collisions still couple T_{gas} and T_{spin} , but Compton scattering

becomes rarer as the CMB dilutes with the expansion of the Universe. While the CMB dilutes as $T_{\text{CMB}} \propto 1/a$, where a is the scale factor, the gas now follows an adiabatic expansion ($T_{\text{gas}} \propto 1/a^2$). Thus, the gas cools quicker than the CMB, and since it is still coupled to the spin temperature, $T_{\text{spin}} < T_{\text{CMB}}$ and the signal is expected to be seen in absorption. By the time the first galaxies begin forming, however, the gas is expected to be so dilute that it is no longer coupled to the spin temperature. The spin temperature therefore couples once again to the CMB, and no signal is produced.

As the first stars in the first galaxies begin emitting Lyman- α photons, they are resonantly scattered off of hydrogen via the Wouthuysen-Field effect (the absorption and emission of Lyman- α photons redistributes the spin-flip states), coupling T_{spin} and T_{gas} (Pritchard & Loeb 2010). The gas, still cool from adiabatic expansion, implies that $T_{\text{spin}} < T_{\text{CMB}}$ and the signal is seen in absorption. Eventually, due to their long mean free paths, x-rays from the first sources are thought to be the primary drivers behind heating of the cooled, low-density gas (Furlanetto et al. 2006). This drives both the gas and spin temperatures above that of the CMB, where the signal is expected to be seen in emission for the first time.

Finally, even though the timing and details of reionization are unknown, UV photons from the first luminous structures are believed to eventually ionize all the neutral hydrogen, leaving no signal to be detected by a redshift of $z \sim 6$.

The shape of the global signal holds important science implications about our early Universe. For example, the timing of the heating trough reveals the types of sources responsible for heating (i.e., late heating implies harder x-ray spectra for x-ray binaries, as shown in Fialkov et al. (2014)). It also contains information regarding the sizes of the dark matter halos hosting those first sources and the cooling mechanisms responsible for star formation (Fialkov et al. 2014). The shape of the absorption feature is also dependent on a number of factors, such as x-ray and Lyman- α emissivities, which in turn are dependent on the nature of the first sources and properties of star formation. For high Lyman- α production rates, a deep trough would be present due to strong couplings between T_{spin} and T_{gas} as the gas cools. An even more pronounced absorption signature, such as the first tentative detection from the Experiment to Detect the Global Epoch of Reionization Signature (EDGES), requires additional physical explanations beyond known physics and commonly accepted scenarios (Bowman et al. 2018).

If the global signal’s primary absorption feature unlocks clues about the first sources, the reionization peak and its subsequent decay hold the key for understanding the evolution of the neutral fraction x_{HI} . Namely, a direct measurement of δT_b during this time would shed light about the duration and rate of the reionization process, which in turn can be translated into an evolution for x_{HI} . A long reionization duration, for example, would yield a slowly varying neutral fraction evolution, while a more instantaneous reionization would produce a sharp drop-off feature (Pritchard & Loeb 2010). One thing is for certain though — as the field continues to investigate our cosmic dawn and the EoR through HI measurements (both the global signal and statistical fluctuations), we can expect to learn much about the constituents that make up the Universe and their complex interactions during this era.

1.1.4 This Thesis

Although 21 cm observations promises an uninterrupted window into the EoR, from which we can learn much about galaxy formation and the properties of the IGM, there are many challenges facing this field of cosmology. In general, the 21 cm signal is extremely faint, with bright foregrounds (mostly synchrotron radiation from our own Galaxy) and radio interference easily overshadowing the target signal. As a consequence, instruments need to be extremely well-understood, precisely calibrated, and sensitive enough for a successful detection. In addition, analysis techniques must be innovative and rigorously construed so as to be able to extract clean and accurate measurements.

In this thesis, I present work associated with data from radio interferometers seeking to measure 21 cm fluctuations during the EoR. While a confirmed detection by an interferometer remains elusive at this time, this work serves as a huge leap forward in working with large datasets and extracting measurements of the cosmological signal with confidence. The rest of this thesis thus focuses on the characterization of data from large telescope arrays in order to place accurate, stringent limits on the EoR signal. This field is still young, and the work in this thesis serves as a foundation of what promises to be an eye-opening adventure to-come.

1.2 Interferometry

Multiple radio telescopes (i.e., an interferometer) can be used in combination to probe 21 cm fluctuations. Rather than a single element, or aperture, many antennas can be used to increase the effective aperture size of the telescope.

As a simplistic example, two antennas may observe the same sky but each receives the sky signal at slightly different times, with a time delay determined by the antenna spacing, or baseline orientation and length, with respect to the sky. The two voltage streams from the antennas can then be correlated to form an output response with an amplitude dependent on the sky's intensity and a phase dependent on the time delay between the two elements and the frequency of the light. The power received by this baseline, as we will see, represents one sample in the large "synthesized" aperture of the interferometer. Knowledge of the entire sky can be built up by having a large number of antennas and many different types, and copies, of baselines.

1.2.1 The Visibility Equation

The output measurement from correlating signals between two antennas is called a *visibility*. The visibility can be written as:

$$V_{ij}(\nu) = S(\nu) e^{-2\pi i \frac{\vec{b}_{ij} \cdot \hat{s}}{\lambda}}, \quad (1.4)$$

where i and j represent a pair of antennas, $S(\nu)$ is the sky flux density, \vec{b}_{ij} is the baseline vector, \hat{s} is a unit-vector in the direction of a source in the sky, and λ is the wavelength of the

signal. The fractional term in the exponential reflects the changing number of wavelengths between the two antennas as a signal goes in and out of phase as the source passes overhead. The entire exponential term represents the phase of the visibility, which can also be described as the fringe pattern, or diffraction, or interference pattern, between two antenna elements.

Equation (1.4) represents a visibility measurement for one direction on the sky. In practice, we compute the integrated visibility over the entire angular sky $d\Omega$:

$$V_{ij}(\nu, \Omega) = \int A(\nu, \Omega) I(\nu, \Omega) e^{-2\pi i \frac{\vec{b}_{ij} \cdot \hat{s}(\Omega)}{\lambda}} d\Omega, \quad (1.5)$$

where the amplitude component has been broken up into a primary beam component $A(\nu, \Omega)$ and sky intensity component $I(\nu, \Omega)$. The primary beam describes the power pattern of an antenna element and determines its field of view. The total power received by an antenna can therefore be thought of as a combination of the intensity distribution on the sky and how receptive the antenna is, or more specifically, the convolution between the two terms (Thompson et al. 2001).

The visibility equation can be re-interpreted as the 2-dimensional Fourier-transform of the sky, or a sample of the uv -plane, where u and v are sine-waves in a 2D image. In other words, every baseline measures a different Fourier-mode of the sky. To form an image, the Fourier-transform of a visibility would produce a *dirty image* of the sky, from which the true sky can be reconstructed by de-convolving out information from the antenna beam. In this thesis, however, we focus on the 3D Fourier-transform of the sky, or the power spectrum (Chapter 1.2.2), instead of making images. Hence, we work directly with visibilities as a starting point, which has already taken two Fourier-transforms for us.

1.2.2 The 21 cm Power Spectrum

In this thesis, we focus on cross-correlations, or power spectral measurements, of visibilities. Recalling that we seek to measure the differential brightness temperature on various spatial scales of the sky, we can form the quantity:

$$\langle \delta \tilde{T}_b(\vec{k})^* \delta \tilde{T}_b(\vec{k}) \rangle = (2\pi)^3 \delta^D(\vec{k} - \vec{k}') P_{21}(\vec{k}), \quad (1.6)$$

where $\delta \tilde{T}_b(\vec{k})$ is the Fourier-transform of the differential sky brightness as a function of cosmological wavenumber \vec{k} (i.e., our visibility measurement, up to scaling factors), δ^D is the Dirac-delta function, and P_{21} is the 21 cm power spectrum quantity we are interested in eventually forming.

Simply speaking, because our visibility measurements have already taken two spatial Fourier-transforms out of the three needed for a 3D power spectrum, we need only to take one last Fourier-transform (along frequency), and then multiply and average the visibilities together for a given baseline in order to compute a power spectral measurement. Having repeated baseline copies then increases the sensitivity to a given Fourier-mode on the sky, while having different types of baselines makes it possible to measure multiple Fourier-modes

and build up an image of the sky. Since the EoR signal is expected to be present everywhere on the sky, in this work we focus on the former technique in order to maximize our sensitivity to the cosmological signal.

We note that the wavenumber \vec{k} can be broken up into a perpendicular component \vec{k}_\perp and a parallel component k_\parallel , where \vec{k}_\perp is proportional to the (x,y) spatial coordinates on the sky and k_\parallel is proportional to the line-of-sight direction on the sky (i.e., frequency). Every unique baseline probes a single \vec{k}_\perp , and it's worth noting that, because we focus on redundant baselines in the analysis to follow, most of our power spectrum sensitivity comes from the frequency-direction. Accounting for cosmological distance, a 1D wavenumber has units of Mpc^{-1} , so that the 3D power spectrum has units of $\text{mK}^2 \cdot \text{Mpc}^3$. Visibility measurements typically have units of Janskys.

Just as the shape of the global signal provides insight about the early Universe, the shape of the cross-power spectrum, as defined by Equation (1.6), also delivers a wealth of information. Figure 1.4 shows the 21 cm “dimensionless” power spectrum $\Delta^2(k)$ (units of mK), defined as:

$$\Delta^2(k) = \frac{k^3}{2\pi^2} P_{21}(k), \quad (1.7)$$

as a function of the magnitude of k . This figure shows the expected evolution of the power spectrum, where the overall signal moves to small scales (large k) as more hydrogen becomes ionized (the large regions of neutral hydrogen turn into smaller and smaller pockets). This effect can be seen by both the steepening of the spectrum as the neutral fraction decreases, and the time-evolution of the spectrum at a specific (large) k .

The 21 cm power spectrum therefore encodes important information about the spatial and temporal evolution of reionization, and the shape of the spectrum can be directly mapped to sizes of the ionized bubbles as they grow. Additionally, the power spectrum, which is a function of the differential brightness temperature, can be used to constrain both T_{spin} (and T_{gas} , since they're coupled during this era) and x_{HI} via Equation (1.3). It is thus a powerful tool for unlocking the properties of the IGM.

1.2.3 Calibration

We now transition to a brief overview of key data processing steps that are often standard routines when going from visibilities to power spectra. We speak broadly about these steps in this chapter, and go into detail about them for specific experiments in later chapters.

As discussed previously, an interferometer measures a visibility for every baseline pair and every time integration. Repeated baseline types and multi-day observations can be stacked to gain sensitivity to Fourier-modes on the sky. However, ensuring clean measurements at EoR sensitivities requires many other crucial processing steps, including calibration, which we give an overview of in this section.

We've seen that the visibility measurement is dependent on the sky, baseline, and antenna beam, but it is also affected by instrumental systematics. For example, certain components

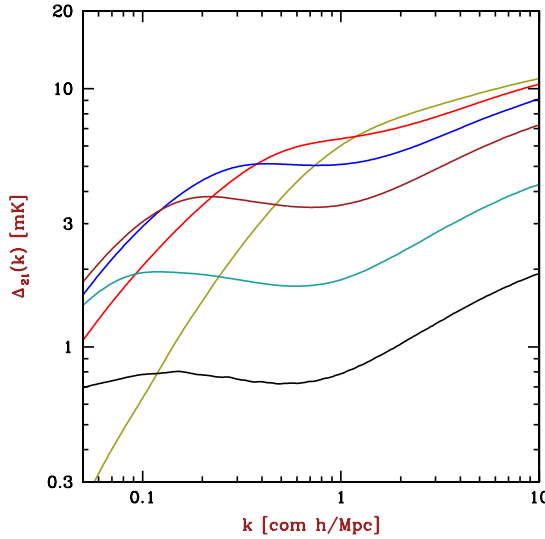


Figure 1.4: The theoretical evolution of the cross-21 cm power spectrum for a specific model (image credit: [Barkana \(2009\)](#)), where the neutral fraction $x_{HI} = 10\%, 30\%, 50\%, 70\%, 90\%$, and 98% from top to bottom at large k . This figure shows the expected evolution of the power spectrum which interferometers seek to measure.

in the signal chain of an instrument can contribute variable noise, losses can arise from reflections, and blockage and scattering may occur. These are all effects that must be considered in order to accurately extract the EoR signal.

Many of these effects can be mitigated through precise calibration. There are two main types of calibration used by 21 cm interferometers: *redundant* calibration and *absolute* calibration. We will briefly describe each here.

Redundant calibration is a type of calibration based on the redundant nature of baselines. For experiments like PAPER and HERA, which have many repeated copies of baselines, redundant calibration can be used to bring all identical baselines into agreement (i.e., it calibrates out deviations between baselines of the same type). This calibration is a powerful technique because it does not use any knowledge of the sky, yet can correct for instrumental-induced gain and phase effects brought on by differences in the signal chain attributable to antennas, cables, and receivers ([Liu et al. 2010](#)).

Mathematically, the visibility v_{ij} of every baseline can be written as:

$$v_{ij} = g_i^* g_j y_{ij} + n_{ij}, \quad (1.8)$$

where g_i and g_j are the complex gains of each antenna, y_{ij} is the “true” model visibility for that particular baseline type, and n_{ij} is noise. The goal of redundant calibration is to solve for the gain of each antenna and the “true” visibility of each baseline type. This can be accomplished by setting up a system of linear equations containing every visibility measurement (the method used by PAPER and HERA is detailed in Chapter [3.1](#)). If there

are more measurements than the sum of the number of unique baselines and antennae, then it is a solvable system.

The complex gains can be further broken down to be written as $g_i = e^{\eta_i + i\phi_i}$ (Liu et al. 2010). In other words, by solving for the gains, we are solving for both an amplitude component and a phase offset for each antenna. The gains can then be divided out of every visibility measurement, producing redundantly-calibrated measurements across the whole array.

While redundant calibration is a clever technique for the internal calibration of an interferometer, the calibrated visibility measurements are still on an arbitrary gain scale that has not been matched up to the sky. Hence, absolute calibration refers to using sources in the sky of known brightness (or sky models) in order to solve for the two remaining internal degrees of freedom: an overall gain and an overall phase. Interferometers typically use a standard self-calibration routine to accomplish this, where y_{ij} is known for specific sky sources.

Ultimately, calibration is a crucial step in preparing interferometric data for a power spectrum analysis. A precisely-calibrated instrument will result in cleaner data from which the EoR signal can be accessed.

1.2.4 Foreground Filtering

Arguably the largest challenge of processing 21 cm data is in removing bright foregrounds. There are several techniques to do this, which fall into two main categories: foreground subtraction and foreground avoidance. The former consists of modeling and subtracting out foreground sources, while the latter involves making EoR measurements in a domain where foregrounds are minimal.

For interferometers with imaging capabilities, foreground removal techniques include modeling approaches to spatially localize and remove contaminants (e.g., Santos et al. 2005; Wang et al. 2006; Jelić et al. 2008; Liu et al. 2009; Bowman et al. 2009; Harker et al. 2009; Chapman et al. 2016). This can be done by fitting polynomials to data or by using non-parametric methods, which make fewer assumptions about the form of the foregrounds. While foreground subtraction would be ideal if done accurately, modeling is difficult and subtraction poses the risk of cosmological signal loss.

The other method commonly used, foreground avoidance, is a strategy employed by both PAPER and HERA. Foreground avoidance was originally suggested as an alternate method to the subtraction method, which has stringent requirements in order to yield uncontaminated results. In order to understand foreground avoidance, we must first define the “EoR Window”.

A 3D power spectrum can be split into two directions along k_{\perp} and k_{\parallel} , which correspond to modes perpendicular to the line-of-sight and along the line-of-sight, respectively. In this two-dimensional space, there are two main regions — one relatively free of foregrounds (the “EoR Window”) and one contaminated by foregrounds (the “wedge”), as shown in Figure 1.5 (e.g., Datta et al. 2010; Vedantham et al. 2012). We can see this by thinking of the k_{\parallel} direction to be akin to the physical time delay associated with light hitting two antennas (a

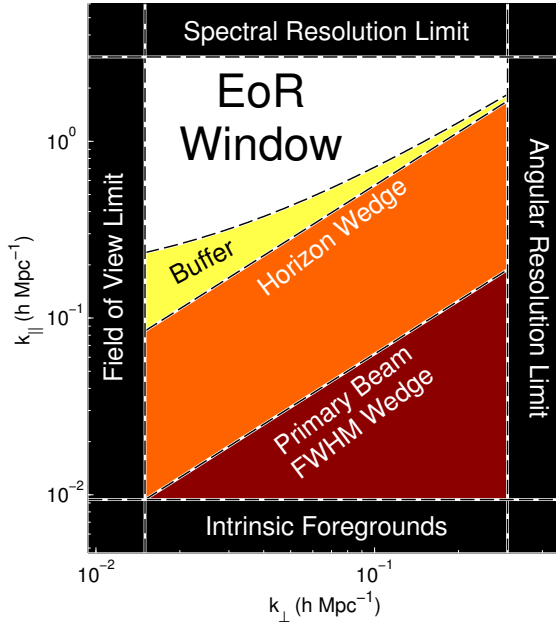


Figure 1.5: A cartoon diagram of the “EoR Window” and “wedge” of foreground contamination in Fourier space (image credit: [Dillon et al. \(2015b\)](#)). A foreground avoidance approach makes power spectrum measurements in the window, while a foreground subtraction approach subtracts out foregrounds so that measurements can be made in the wedge. The overall power spectrum measurement space is limited by an interferometer’s field of view and angular resolution along the horizontal axis, and spectral resolution and intrinsic foregrounds along the vertical axis.

good approximation, especially for short baselines). As k_{\perp} , which is proportional to baseline length, increases, the maximum time delay also increases because it is set by the length of the baseline (i.e., a maximum delay occurs when a source is at the horizon; therefore, the time delay is simply the time it takes for the light to travel the distance of the baseline). Hence, the “wedge” is formed, representing a region where smooth-spectrum foregrounds are expected to be contained. Said differently, foregrounds are expected to be bound by the light-crossing time between two antennas, and therefore there is a maximum limit for k_{\parallel} (time delay) given a k_{\perp} (baseline).

Delay-filtering is the process by which foregrounds within the wedge are filtered out, leaving a relatively clean window behind from which the cosmological signal can be extracted ([Parsons et al. 2012](#)). This approach limits the number of modes for which the measurement can be made and can suffer from some foreground leakage as explained in Chapter 2.5, but its advantages include its simplicity and conservativeness (i.e., it leaves all the cosmological signal within the window in tact).

Whether it’s avoidance or removal, there have been many approaches at tackling the challenge of foregrounds (summarized in [Chapman et al. \(2016\)](#)). But, regardless of the

method used, removing Galactic and extragalactic foregrounds from 21 cm data is absolutely a critical step for analyses seeking the EoR signal.

1.2.5 Fringe-rate Filtering

The final analysis technique to introduce in this section is fringe-rate filtering, a filtering scheme carried out in a domain which is the Fourier-dual to time. This type of filtering aims to optimize the process of combining time-ordered data and has been investigated in [Roshi & Perley \(2003\)](#), [Parsons & Backer \(2009\)](#), [Offringa et al. \(2012\)](#), and [Parsons et al. \(2016\)](#).

A “fringe-rate” is the rate at which the sky moves relative to the fringe pattern of an interferometer. As sources pass overhead, they walk in and out of the interference pattern of two antennas, and the rate at which this movement happens is dependent on the source’s declination and hour angle. For example, a source located near a celestial pole has a zero fringe-rate, as it does not appear to move in the sky as the Earth rotates. However, a source located on the celestial equator will have a maximum fringe-rate set by the rate of Earth’s rotation. The sky can therefore be decomposed into fringe-rate bins, each of which forms a concentric circle of constant fringe-rate around the celestial sphere.

One initial advantage of filtering in fringe-rate space is that it allows the filtering of noise that is not associated with movement locked on the sky (i.e., filtering out fringe-rates greater than the maximum allowed by the Earth’s rotation). This excess noise can come from the instrument itself or from signals with an origin not on the sky. Additionally, one can up-weight and down-weight certain portions of the sky by choosing different linear combinations of fringe-rates ([Parsons et al. 2016](#)). This allows what is effectively a beam-sculpting operation, where the most sensitive parts of one’s beam can be up-weighted compared to others.

A third advantage of this type of filtering is that it can also be used to integrate visibilities in time. Depending on the shape of the filter in the fringe-rate domain, the effect in the time domain can be an averaging operation along time. This is advantageous because it allows an optimal way of combining measurements (by weighting fringe-rates differently based on signal-to-noise ratios in each fringe-rate bin, for example) compared to a more traditional boxcar average, which does not use information from individual fringe-rate bins.

Broadly, fringe-rate filtering can be thought of as a tailored filtering step that can increase the sensitivity of a measurement by differentiating between noise- and signal-like modes in data. When carefully chosen, a fringe-rate filter can enhance modes containing emission from the celestial sphere, where the 21 cm signal lies.

1.3 Instruments

The recent exploration of our cosmic dawn has led to the development of multiple experiments that are aiming to detect the 21 cm signal from neutral hydrogen during reionization. In this section we will first highlight the two main radio interferometers whose data is used

in this thesis, and then discuss other similar experiments along with the current status of the field.

1.3.1 The Precision Array for Probing the Epoch of Reionization

The Precision Array for Probing the Epoch of Reionization (PAPER) is a first generation EoR experiment. Its history dates back to 2007, when an initial four dipole antennas observed the sky from Western Australia. A year later, the array increased to eight stations and moved to Green Bank, West Virginia. These first two deployments are summarized in [Parsons et al. \(2010\)](#) and were used to characterize important aspects of the instrument, including system performance, beam models, instrumental temperatures, and sensitivity to radio frequency interference (RFI).

PAPER then moved to the Karoo Desert in South Africa, near the Square Kilometre Array South Africa (SKA-SA). The PAPER array doubled in size each year, starting with 32 antennas in 2011 and ending with 128 a few years later. PAPER’s observing seasons using these three arrays (PAPER-32, PAPER-64, and PAPER-128) have primarily been used to develop analysis techniques, understand instrumental design, and begin to place limits on the EoR and connect them to science implications.

A brief overview of the PAPER instrument and digital backend follows. The PAPER dipole itself (Figure 1.6) is made from two rods of copper sandwiched between two aluminum disks. The sizes of each are fine-tuned to produce an antenna frequency response between 100-200 MHz. Each PAPER antenna is sensitive to two orthogonal polarizations, those being the East/West and North/South directions (XX and YY linear polarizations) given the antenna’s orientation on the ground. A grounding structure, made of wire-mesh and held in place by PVC pipes, is both underneath the dipole and surrounds it as four angled panels. The design of the antenna’s framework was driven by the desire to produce spectrally and spatially smooth beam responses as discussed in [Parsons et al. \(2010\)](#) and [Pober et al. \(2012\)](#). Altogether, an entire PAPER dipole measures about 2 m on each side and sits still while the Earth’s rotation moves the sky above (“drift-scan” mode). When photons hit the dipoles’ copper rods, electrons are excited and their movement turns the electric field into a voltage that can be measured.

In short, PAPER’s analog system consists of a balun attached to each dipole element (which measures the voltage and amplifies the signal) and coaxial cables which transport the antenna signals. The signals then travel to dual-channel receiver boards which are cooled inside thermal enclosures in order to prevent the introduction of high gains from temperature fluctuations. The receivers both amplify and filter (in frequency) the signals before sending them to the digital system.

PAPER’s digital system is housed inside a refrigerated container on the observing site. The bulk of the processing is carried out by a series of real-time digital FX correlators which cross-correlate pairs of antenna signals to form visibility measurements. More specifically, the FX correlators comprise of “F-engines” which digitize, down-convert, and channelize antenna inputs, a switch that divides the data into frequency subsets and routes the packets, GPUs



Figure 1.6: A PAPER antenna in the Karoo Desert in South Africa. A dual-polarization dipole sits at the center, surrounded by wire mesh panels that measure 2 m on each side.

which cross-multiply signals from all antenna pairs and integrate in time (“X-engines”), and finally another switch and computer which collect the data, writes it to disk, and sends the final products over an ethernet connection as “raw” visibility data products that are ready to be analyzed.

Much of PAPER’s digital signal processing (DSP) system has been made possible due to the development of hardware by the Center for Astronomy Signal Processing and Electronics Research (CAPSER). We rely on their Field-programmable Gate Array (FPGA) processors which can quickly perform the fast Fourier-transforms required to produce visibilities. The development of FPGA’s into PAPER’s DSP system has been critical in allowing for the scalable expansion of the array.

PAPER’s first power spectrum limits on the EoR came from its 32-element array ([Parsons et al. 2014](#)). PAPER-32 observed in a redundantly-configured layout from 2011-2012, producing a published 2σ upper limit on the 21 cm power spectrum of $(41 \text{ mK})^2$ for $k = 0.27 h \text{ Mpc}^{-1}$ at $z = 7.7$ ([Parsons et al. 2014](#)). This result, while orders of magnitude above predicted EoR signals, was used to generate constraints on the brightness temperature of 21 cm emission for various reionization models and rule out cold reionization scenarios (i.e., some heating of the IGM is necessary by $z = 7.7$ to be consistent with PAPER-32’s results).

PAPER expanded to 64 elements in 2012, keeping its redundant layout in order to maximize power spectrum sensitivity. The analysis and initial results for PAPER-64’s observing season is outlined in [Ali et al. 2015](#), where a 2σ upper limit on the EoR is published as $(22 \text{ mK})^2$ for $0.15 < k < 0.5 h \text{ Mpc}^{-1}$ at $z = 8.4$. A result at this sensitivity can begin to place more interesting limits on IGM heating models and on the temperature of the IGM during this time ([Pober et al. 2015](#)).

From 2013-2015, PAPER-128 marked the last era for the PAPER experiment. The data

collected with this array has not been published publicly and work is ongoing to process and analyze this data. While most of this thesis focuses on PAPER-64, specifically on analysis methods developed to revise the initial (incorrect) PAPER-64 results (Chapter 2) and what those new limits should be (Chapter 3), we also present a first-look at PAPER-128 and discuss how PAPER’s final observing season has influenced analysis metrics for next generation experiment HERA (Chapter 5).

The PAPER experiment as a whole has been absolutely fundamental to the growth of the field of 21 cm cosmology. This first generation experiment set a standard for other similar experiments and has provided countless lessons in all aspects of the signal chain. The array may be retired, but its influence will not be forgotten.

1.3.2 The Hydrogen Epoch of Reionization Array

The development of the Hydrogen Epoch of Reionization Array (HERA) was largely driven by the need for increased sensitivity, as even PAPER-128 lacked the collecting area for a significant detection of the EoR. HERA is a second generation EoR experiment currently being built in the Karoo. It features a staged build-out of parabolic dishes with 14 m diameters, with construction beginning in 2015 and an eventual 350 dishes planned to be completed by the end of 2019.

A HERA dish (Figure 1.7) is made up of wire-mesh, PVC pipes, and wooden support structures. The size, shape, and total number of the dishes were chosen in order to optimize sensitivity (i.e., minimize chromatic effects that would leak power into the EoR window), minimize costs, and be easily scalable and robust for a five year lifetime (DeBoer et al. 2017). While work on a new feed design (with a wider bandwidth) is ongoing, the first observations from HERA use recycled PAPER dipoles. Suspended upside-down with a wire pulley-system, the PAPER dipoles are surrounded by a wire-mesh backplane structure that minimizes cross-coupling between antennas while optimizing beam efficiency, frequency response, and polarization match (DeBoer et al. 2017). Similarly, the first stages of the HERA array are using the existing PAPER signal chain and hardware, while work is progressing towards an underground node-based architecture that will house the DSP system and minimize cable reflections by allowing for shorter cable paths.

The configuration of HERA, like PAPER, is highly redundant and optimized for a robust foreground avoidance approach. Because this power spectrum approach requires short baselines (which minimize the wedge), the HERA antennas are densely-packed next to each other into a main core. This core is segmented into three displaced sections, whose sectioning is designed to improve HERA’s imaging ability (Dillon & Parsons 2016). Additionally, there will be 30 outrigger elements joining the full array, allowing for a more complete *uv*-plane coverage and imaging capabilities that can be leveraged for a foreground removal approach. The full HERA array is depicted in Figure 1.8.

The primary science goal of HERA is to make a high-significance detection of the cosmological signal in order to constrain the timing and morphology of reionization. With precision constraints on the EoR, we can begin to understand the role of the first stars and



Figure 1.7: A HERA dish in the Karoo Desert in South Africa. Wire-mesh, PVC pipes, and wooden structures serve as the foundation for the 14 m diameter parabola. A PAPER dipole is suspended upside-down with a wire pulley-system and surrounded by a prototype wire-mesh skirt structure. HERA-350 will use an updated design for its feed; however, HERA’s initial data releases use the old PAPER infrastructure as depicted here.

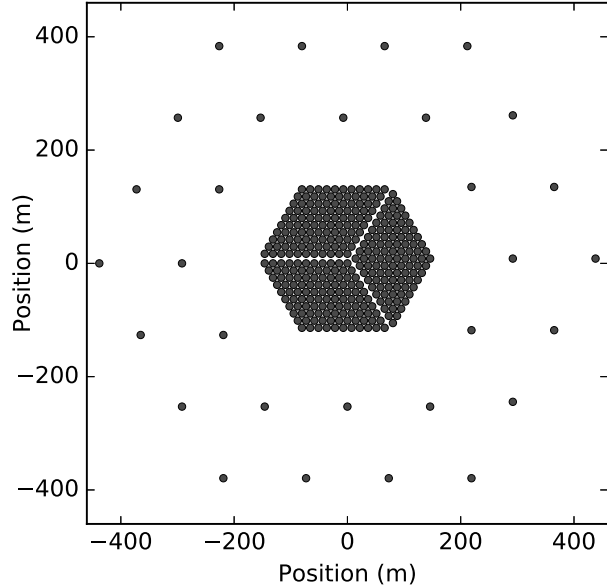


Figure 1.8: The full HERA-350 array (image credit: [DeBoer et al. \(2017\)](#)). The array is comprised of a segmented densely-packed core (to optimize redundancy for a foreground avoidance approach) and surrounding outrigger elements (for imaging capabilities).

galaxies in driving reionization, their complex interactions with their environments, and the evolution of cosmic structure. With the full array and an upgraded feed sensitive from 50–250 MHz, secondary science goals of the instrument include precision cosmology, imaging of the reionization epoch, and an investigation of the pre-reionization heating epoch (DeBoer et al. 2017). HERA, with a collecting area of $\sim 0.1 \text{ km}^2$, is well-poised for these challenges (Pober et al. 2014) and has already undergone numerous tests and simulations to ensure that its design meets specification (Neben et al. 2016; Ewall-Wice et al. 2017; Patra et al. 2018). As the fully realized HERA soon approaches, there is much to look forward to in the coming years from this array.

1.3.3 Other Experiments and Status of Field

Although this thesis focuses mostly on PAPER data and analysis methods that will be used by HERA, these two arrays are not alone in their quest for the EoR. Other radio interferometers which seek to measure statistical power spectra include the Giant Metre-wave Radio Telescope located in India (GMRT; Paciga et al. 2013a), the LOw Frequency ARray in Europe (LOFAR; van Haarlem et al. 2013), the Murchison Widefield Array in Australia (MWA; Tingay et al. 2013), the 21 Centimeter Array in China (21CMA; Peterson 2004; Wu 2009), and the Square Kilometre Array in South Africa (SKA; Koopmans et al. 2015).

Several of these experiments have succeeded in placing upper limits on the EoR, including results from the 32-tile MWA (Dillon et al. 2014), 128-tile MWA (Dillon et al. 2015a; Beardsley et al. 2016), GMRT (Paciga et al. 2013a), and LOFAR (Patil et al. 2017). PAPER has also previously published results using 32 antennas (Parsons et al. 2014; Jacobs et al. 2015) and 64 antennas (Ali et al. 2015), though we highlight the errors found in PAPER’s analysis pipeline throughout this thesis and thus refer the reader to Chapter 3 for updated results from PAPER.

The work in the 21 cm community that has led to these power spectrum limits (Figure 1.9) has largely revolved around the key challenge of controlling foregrounds and systematics. To accomplish this, significant progress has been made in all aspects of the experimental process, ranging from carefully designed interferometers (Lonsdale et al. 2009; Parsons et al. 2012; Dillon & Parsons 2016), to novel methods for understanding and dealing with foregrounds (e.g., Morales et al. 2006; Datta et al. 2010; Sullivan et al. 2012; Moore et al. 2013; Hazelton et al. 2013; Pober et al. 2013; Liu et al. 2014a; Liu et al. 2014b; Thyagarajan et al. 2015), to statistical analysis techniques for precise calibration and power spectrum estimation (e.g., Liu et al. 2010; Trott et al. 2012; Liu et al. 2014b; Zheng et al. 2014; Dillon et al. 2014; Jacobs et al. 2016a). PAPER’s foreground avoidance strategies have, in particular, led to detailed understandings of redundant calibration and the effects of filtering on the EoR window, while MWA’s foreground subtraction techniques have provided complementary improvements in imaging capabilities. While the experiments with published results currently lack the sensitivities needed for an EoR detection, both the delay-filtering and map-making methods, along with hybrid approaches (Trott et al. 2016), have set a strong foundation for

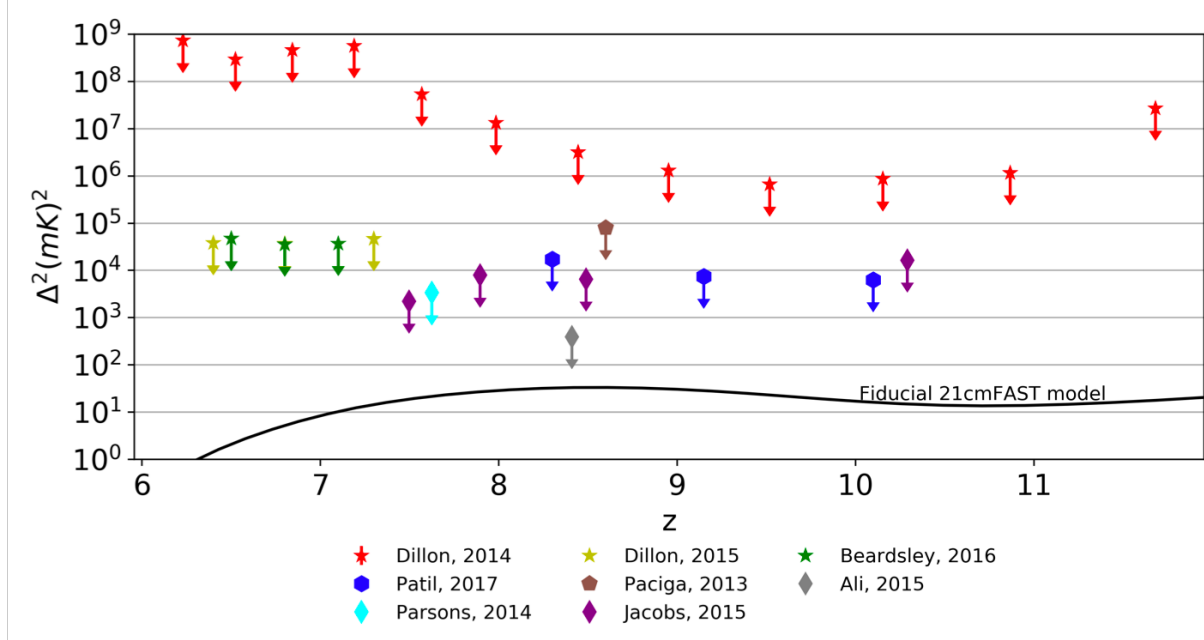


Figure 1.9: Published upper limits on the EoR placed by different 21 cm experiments, prior to the work in this thesis. All PAPER results shown (PAPER-32 is in cyan and magenta, and PAPER-64 is in gray) are suspect to the errors discussed throughout this work and are superseded by the ones presented in Chapter 3.

controlling foregrounds by future, more sensitive interferometers.

Related to the fundamental goal of simultaneously maximizing sensitivity and minimizing contaminants, some other challenges that face current 21 cm experiments include polarization leakage from Faraday-rotated emission (Moore et al. 2013; Kohn et al. 2016; Nunhokee et al. 2017), direction-dependent beam effects, and other low level sources of chromaticity induced by the instrument or calibration. These effects will require thorough investigations as experiments approach EoR sensitivities.

In addition to power spectrum experiments, there are several complementary experiments that aim to measure the sky-averaged global 21 cm signal (i.e., the mean brightness temperature of the EoR relative to the CMB). These include the Experiment to Detect the Global EoR Signature (EDGES; Bowman & Rogers 2010), the Large Aperture Experiment to Detect the Dark Ages (LEDA; Bernardi et al. 2016), the Dark Ages Radio Explorer (DARE; Burns et al. 2012), the Sonda Cosmológica de las Islas para la Detección de Hidrógeno NeutroSciHi (SCI-HI; Voytek et al. 2014), the Broadband Instrument for Global HydrOgen Reionisation Signal (BIGHORNS; Sokolowski et al. 2015), and the Shaped Antenna measurement of the background RAdio Spectrum (SARAS; Patra et al. 2015).

Like the power spectrum experiments, global signal experiments also face challenges of bright foregrounds and instrumental systematics. In particular, they require extremely precise calibration in order to avoid overfitting when subtracting foregrounds, and they

also face additional challenges when observing the lowest frequencies, such as ionospheric fluctuations and brighter foregrounds (Vedantham et al. 2014; Datta et al. 2014).

However, most global signal telescopes consist of single elements and can therefore be more easily constructed. Additionally, EoR sensitivities can be reached with relatively short observations. Thus, global signal experiments are actively being worked on as a complementary view into the evolution of the 21 cm signal. Accurate detections of the features of the global signal will delineate the different epochs in the early Universe, and their shapes will carry important implications about the nature of the IGM and the first sources.

For example, the first potential detection of the 21 cm signal has been made by the global signal experiment EDGES (Bowman et al. 2018). This exciting result suggests the presence of an absorption feature in the sky-averaged spectrum at 78 MHz, thought to be the result of the absorption of CMB photons by HI gas. Because the detected feature is best-fit by an amplitude much larger than what is consistent with expectations for the 21 cm signal during this epoch, alternate scientific explanations have been offered, such as the influence of dark matter on baryons and the effect of their interaction on the temperature of the gas (Barkana 2018; Slatyer & Wu 2018), . Measurements from other experiments in the future will certainly be informative in shaping the community’s confidence in this detection, and this result marks just the beginning of many more in the field to come.

Chapter 2

Power Spectrum Methods

2.1 Power Spectrum Themes and Techniques

The major challenge that faces all 21 cm experiments is isolating a small signal that is buried underneath foregrounds and instrumental systematics that are, when combined, four to five orders of magnitude brighter (e.g., Santos et al. 2005; Ali et al. 2008; de Oliveira-Costa et al. 2008; Jelić et al. 2008; Bernardi et al. 2009, 2010; Ghosh et al. 2011; Pober et al. 2013; Bernardi et al. 2013; Dillon et al. 2014; Kohn et al. 2016). A clean measurement therefore requires an intimate understanding of the instrument and a rigorous study of data analysis choices. With continual progress being made in the field and HERA on the horizon, it is becoming increasingly important to understand how the methods we choose interact with each other to affect power spectrum results. More specifically, it is imperative to develop techniques and tests that ensure the accuracy and reliability of a potential EoR detection. In this chapter and the next, we discuss three topics (signal loss, error estimation, and bias) that are essential to investigate for a robust 21 cm power spectrum analysis. We also highlight four power spectrum techniques (fringe-rate filtering, weighting, bootstrapping, jackknife testing) and their trade-offs, potential pitfalls, and connections to the themes. We first approach the themes from a broad perspective (Chapter 2), introducing the themes of our focus and using toy models to develop intuition into each one. We then perform a detailed case study (Chapter 3) using data from the 64-element configuration of PAPER, highlighting key changes from the methods used in the previously published result in Ali et al. (2015), henceforth known as A15, which have led to a revised PAPER-64 power spectrum result. In these two chapters we use a subset of PAPER-64 data to illustrate our revised analysis methods, while Chapter 4 builds off of the methods to finally present revised PAPER-64 results for multiple redshifts and baseline types.

We note that this thesis as a whole adds to the growing foundations of lessons which have been documented, for example, in Paciga et al. (2013b), Patil et al. (2016), and Jacobs et al. (2016b), by the GMRT, LOFAR, and MWA projects respectively. These lessons are imperative as the community as a whole moves towards higher sensitivities and potential EoR detections.

There are many choices a 21 cm data analyst must consider. How can time-ordered measurements be combined? How can the variance of the data be estimated? In what way(s) can the data be weighted to suppress contaminated modes while not destroying an EoR signal? How can a statistically significant detection of a signal be properly identified? Many common techniques, such as averaging data, weighting, bootstrapping, and jackknife testing, address these issues but harbor additional trade-offs. For example, an aggressive filtering method may succeed in eliminating interfering systematics but comes at the cost of losing some EoR signal. A chosen weighting scheme may theoretically maximize sensitivity but fail to suppress foregrounds in practice.

Though there are many data analysis choices, measuring the statistical 21 cm power spectrum ultimately requires robust methods for determining accurate confidence intervals and rigorous techniques to identify and control systematics. In this thesis, we focus on three 21 cm power spectrum themes that encapsulate this goal and discuss four techniques that interplay with each other and impact the themes. We will give brief definitions now, and build intuition for each theme in the sections to follow.

- **Signal Loss** (Chapter 2.2): Signal loss refers to attenuation of the target *cosmological* signal in a power spectrum estimate. Certain analysis techniques can cause this loss, and if the amount of loss is not quantified accurately, it could lead to false non-detections and overly aggressive upper limits. Determining whether an analysis pipeline is lossy, and estimating the amount of loss if so, has subtle challenges but is necessary to ensure the accuracy of any result.
- **Error Estimation** (Chapter 2.4): Confidence intervals on a 21 cm power spectrum result determine the difference between a detection and a null result, which have two very different implications. Additionally, accurate error estimation is crucial for the comparison of results to theoretical models. Errors can be estimated in a variety of ways, and we will discuss a few of them.
- **Bias** (Chapter 2.5): There are several possible sources of power offset in a visibility measurement that can show up as a detection in a power spectrum, such as bias from noise and foregrounds. In particular, a successful EoR detection would also imitate a bias. Proving that a bias is an EoR detection may be the most difficult challenge for future 21 cm analyses, as it is crucial to be able to distinguish a detection of foreground leakage, for example, from that of EoR. In this chapter, we will highlight some sources of bias, discuss ways to mitigate their effects, and describe example tests that a true EoR detection must pass.

The following techniques each have advantages when it comes to maximizing sensitivity and understanding systematics in data. However, some have limitations, and we will discuss circumstances in which there are trade-offs. We choose to focus on these four techniques because they represent major steps in PAPER’s power spectrum pipeline, with several of them also being standard steps in general 21 cm analyses.

- **Fringe-rate filtering:** Fringe-rate filtering is an averaging scheme for time-ordered data (Parsons et al. 2016). Broadly, a fringe-rate filter averages visibilities in time to produce a smaller number of more sensitive independent samples. However, such a filter also affects the presence of foregrounds and systematics. We explain the trade-offs of filtering in more detail in Chapter 2.2.3.
- **Weighting:** A dataset can be weighted to emphasize certain features and minimize others. One particular flavor of weighting employed by previous PAPER analyses is inverse covariance weighting in frequency, which is a generalized version of inverse variance weighting that also takes into account frequency correlations (Liu & Tegmark 2011; Dillon et al. 2013; Liu et al. 2014a; Liu et al. 2014b; Dillon et al. 2014; Dillon et al. 2015a). Using such a technique enables the down-weighting of contaminant modes that obey a different covariance structure from that of cosmological modes. However, a challenge of inverse covariance weighting is in estimating a covariance matrix that is closest to the true covariance of the data; the discrepancy between the two can have large impacts on signal loss. We investigate the impact of different types of weighting on signal loss in Chapter 2.2.
- **Bootstrapping:** In addition to using theoretical models for covariance matrices and theoretical error estimation methods, bootstrapping is one way to estimate errors. Namely, bootstrapping is a useful method for estimating errors of a dataset from itself (Andrae 2010). By randomly drawing many subsamples of the data, we obtain a sense of its inherent variance, though there are subtleties to consider such as the independence of values in a dataset. We explore this potential pitfall of bootstrapping in Chapter 2.4.
- **Jackknife testing:** A resampling technique useful for estimating bias, jackknives can be taken along different dimensions of a dataset to cross-validate results. In particular, null tests can be used to verify whether results are free of systematics, as done with CO power spectra (Keating et al. 2016) and CMB measurements (see e.g. Ade et al. 2008; Chiang et al. 2010; Bischoff et al. 2011; Das et al. 2011a; Araujo et al. 2012; Crites et al. 2015; BICEP2 Collaboration et al. 2016; Ade et al. 2017; Sherwin et al. 2017). An EoR detection must pass both jackknife and null tests, which we highlight in Chapter 2.5.2.

In the next three sections, we study each theme in depth, focusing on how power spectrum technique trade-offs affect each. We use toy data models to develop intuition into why certain analysis choices may be appealing and discuss ways in which they are limited. We highlight problems that can arise regarding each theme and offer suggestions to mitigate the issues. Ultimately, we show that rigorous investigations into signal loss, error estimation, and bias must be performed for robust 21 cm results.

2.2 Signal Loss Toy Model

Signal loss can arise in a variety of ways in an analysis pipeline, such as by fitting a polynomial during spectral calibration, applying a delay domain filter, or deriving weights from data and applying them to itself. Here we focus on signal loss associated with the use of an empirically estimated covariance matrix with the “optimal quadratic estimator” formalism. This loss was significantly under-estimated in the [A15](#) analysis.

2.2.1 The Quadratic Estimator Method

We begin with an overview of the quadratic estimator (QE) formalism used for power spectrum estimation. The goal of power spectrum analysis is to produce an unbiased estimator of the EoR power spectrum in the presence of both noise and foreground emission. Prior to power spectrum estimation, the data will often have been prepared to have minimal foregrounds by some method of subtraction, so this foreground emission may appear either directly (because it was not subtracted) or as a residual of some subtraction process not in the power spectrum domain. If an accurate estimate of the total covariance of the data is known, including both the desired signal and any contaminants, then the “optimal quadratic estimator” formalism provides a method of producing a minimum variance, unbiased estimator of the desired signal, as shown in [Liu & Tegmark \(2011\)](#), [Dillon et al. \(2013\)](#), [Liu et al. \(2014a\)](#), [Liu et al. \(2014b\)](#), [Trott et al. \(2012\)](#), [Dillon et al. \(2014\)](#), [Dillon et al. \(2015a\)](#), [Switzer et al. \(2015\)](#), and [Trott et al. \(2016\)](#).

Suppose that the measured visibilities for a single baseline in Jy are arranged as a data vector, \mathbf{x} . It has length $N_t N_f$, where N_t is the number of time integrations and N_f is the number of frequency channels. The covariance of the data is given by

$$\mathbf{C} \equiv \langle \mathbf{x} \mathbf{x}^\dagger \rangle = \mathbf{S} + \mathbf{U} \quad (2.1)$$

where the average over an ensemble of data realizations produces the true covariance, and we further assume it may be written as the sum of the desired cosmological signal \mathbf{S} and other terms \mathbf{U} .

We are interested in estimating the three-dimensional power spectrum of the EoR. Visibilities are measurements of the Fourier transform of the sky along two spatial dimensions (using the flat-sky approximation), and since we are interested in three-dimensional Fourier modes we only need to take one Fourier transform of our visibilities along the line-of-sight dimension. We consider band powers P^α of the power spectrum of \mathbf{x} over some range in cosmological \mathbf{k} , where α indexes a waveband in k_{\parallel} (a cosmological wavenumber k_{\parallel} is the Fourier dual to frequency under the delay approximation ([Parsons et al. 2012](#)), which is a good approximation for the short baselines that PAPER analyzes). The fundamental dependence of the covariance on the power spectrum band powers P^α is encoded as

$$\mathbf{S} = \sum_{\alpha} P^\alpha \frac{\partial \mathbf{C}}{\partial P^\alpha} \equiv \sum_{\alpha} P^\alpha \mathbf{Q}^\alpha \quad (2.2)$$

where we define $\frac{\partial \mathbf{C}}{\partial P^\alpha} \equiv \mathbf{Q}^\alpha$. In other words, \mathbf{Q} describes the response of the covariance to a change in the power spectrum, relating a quadratic statistic of the data (the covariance) to a quadratic statistic in Fourier-space (the power spectrum).

The optimal quadratic estimator prescription is then to compute

$$\hat{P}^\alpha = \sum_\beta (\mathbf{F}^{-1})^{\alpha\beta} (\hat{q}^\beta - \hat{b}^\beta) \quad (2.3)$$

where \mathbf{F} is the Fisher matrix (which determines errors on the power spectrum estimate)

$$F^{\alpha\beta} \equiv \frac{1}{2} \text{tr} (\mathbf{C}^{-1} \mathbf{Q}^\alpha \mathbf{C}^{-1} \mathbf{Q}^\beta), \quad (2.4)$$

\hat{q} is the un-normalized power spectrum estimate

$$\hat{q}^\alpha = \frac{1}{2} \mathbf{x}^\dagger \mathbf{C}^{-1} \mathbf{Q}^\alpha \mathbf{C}^{-1} \mathbf{x}, \quad (2.5)$$

and \hat{b} is the additive bias

$$\hat{b}^\alpha = \frac{1}{2} \text{tr} (\mathbf{U} \mathbf{C}^{-1} \mathbf{Q}^\alpha \mathbf{C}^{-1}). \quad (2.6)$$

The power spectrum estimator in Equation (2.3) is the minimum variance (smallest error bar) estimate of the power spectrum subject to the constraint that it is also unbiased; that is, the ensemble average of the estimator is equal to its true value

$$\langle \hat{P}^\alpha \rangle = P^\alpha \quad (2.7)$$

([Tegmark 1997](#); [Bond et al. 1998](#)).

Intuitively, the estimator must be capable of “suppressing” or “removing” the effects of contaminants in order to obtain an unbiased estimate of the power spectrum. By construction, the subtraction of the residual foreground and noise bias accomplishes this, removing any additive bias. However, the \mathbf{C}^{-1} piece of Equation (2.5) also has the effect of suppressing residual foregrounds and noise, in both the additive bias and any contributions the residuals may have to the variance. The way in which the optimal estimator accomplishes this is illustrated with a toy model in Chapter [2.3.1](#). In this chapter, we show that the effect of the weighting in Equation 2.5 is to project out the modes of \mathbf{U} with a different covariance structure than \mathbf{S} in the power spectrum estimate, and the effect of Equation 2.6 is to subtract out the remaining bias. Similar effects for a realistic model of the EoR and foregrounds are shown in [Liu & Tegmark \(2011\)](#).

The toy model in Chapter [2.3.1](#) also illustrates that if the covariance structure of the contaminants is sufficiently different from the desired power spectrum, then the linear bias term may be expected to be quite small, and it is only necessary to know \mathbf{C} and \mathbf{Q}^α , but not \mathbf{U} . Since the foregrounds are expected to be strongly correlated between frequencies whereas the EoR is not, we expect different covariance structures and therefore a small linear bias. Moreover, because the linear bias is always positive and there is no multiplicative bias, the

quadratic-only term will always produce an estimate which is *high* relative to the true value, and which can conservatively be interpreted as an upper limit. These considerations, and the difficulty of obtaining an estimate for \mathbf{U} , motivate the neglect of the linear bias in the rest of this analysis.

Motivated by the desire to retain the advantageous behavior of suppressing contributions of \mathbf{U} to estimates of the EoR power spectrum, we note that it is possible to define a modified version of the quadratic estimator where Equation (2.5) is replaced by

$$\hat{q}^\alpha = \frac{1}{2} \mathbf{x}^\dagger \mathbf{R} \mathbf{Q}^\alpha \mathbf{R} \mathbf{x} \quad (2.8)$$

where \mathbf{R} is a weighting matrix chosen by the data analyst. For example, inverse covariance weighting (the optimal form of QE) would set $\mathbf{R} \equiv \mathbf{C}^{-1}$ and a uniform-weighted case would use $\mathbf{R} \equiv \mathbf{I}$, the identity matrix. Again, the matrix \mathbf{Q}^α encodes the dependence of the covariance on the power spectrum but in practice also does other things, including implementing a transform of the frequency domain visibilities to \mathbf{k} -space, taking into account cosmological scalings, and converting the visibilities from Jansky to Kelvin.

With an appropriate normalization matrix \mathbf{M} , the quantity

$$\hat{\mathbf{P}} = \mathbf{M} \hat{\mathbf{q}} \quad (2.9)$$

is a sensible *estimate* of the *true* power spectrum \mathbf{P} .

To ensure that \mathbf{M} correctly normalizes our power spectrum, one may take the expectation value of Equation (2.9) to obtain

$$\begin{aligned} \langle \hat{P}^\alpha \rangle &= \frac{1}{2} \sum_{\beta\gamma} M^{\alpha\gamma} \text{tr}(\mathbf{R} \mathbf{Q}^\gamma \mathbf{R} \mathbf{Q}^\beta) P^\beta + \frac{1}{2} \sum_\gamma \text{tr}(\mathbf{U} \mathbf{R} \mathbf{Q}^\gamma \mathbf{R}) \\ &\equiv \sum_\beta W^{\alpha\beta} P^\beta + \frac{1}{2} \sum_\gamma \text{tr}(\mathbf{U} \mathbf{R} \mathbf{Q}^\gamma \mathbf{R}), \end{aligned} \quad (2.10)$$

where $W^{\alpha\beta}$ are elements of a window function matrix. Considering the first term of this expression (again, we are assuming that the linear bias term is significantly suppressed; and if this is not the case, we are simply assuming that we are setting a conservative upper limit), if \mathbf{W} ends up being the identity matrix for our choices of \mathbf{R} and \mathbf{M} , then we recover Equation (2.7) for the first term, and we have an estimator that has no multiplicative matrix bias. However, Equation (2.7) is a rather restrictive condition, and it is possible to violate it and still have a sensible (and correctly normalized) power spectrum estimate. In particular, as long as the rows of \mathbf{W} sum to unity, our power spectrum will be correctly normalized. Beyond this, the data analyst has a choice for \mathbf{M} , and for simplicity throughout this thesis we choose \mathbf{M} to be diagonal. In a preview of what is to come, we also stress that the derivation that leads to Equation (2.10) assumes that \mathbf{R} and \mathbf{x} are not correlated. If this assumption is violated, a simple application of the (now incorrect) formulae in this section can result in an improperly normalized power spectrum estimator that does not conserve power, i.e., one that has signal loss.

Given the advantages of inverse covariance weighting, a question arises of how one goes about estimating \mathbf{C} . One method is to empirically derive it from the data \mathbf{x} itself. Similar types of weightings that are based on variance information in data are done in [Chang et al. \(2010\)](#) and [Switzer et al. \(2015\)](#). In previous PAPER analyses, one time-averages the data to obtain:

$$\hat{\mathbf{C}} \equiv \langle \mathbf{x} \mathbf{x}^\dagger \rangle_t \approx \langle \mathbf{x} \mathbf{x}^\dagger \rangle, \quad (2.11)$$

assuming $\langle \mathbf{x} \rangle_t = 0$ (a reasonable assumption since fringes average to zero over a sufficient amount of time), where $\langle \cdot \rangle_t$ denotes a finite average over time. The weighting matrix for our empirically estimated inverse covariance weighting is then $\mathbf{R} \equiv \hat{\mathbf{C}}^{-1}$, where we use a hat symbol to distinguish the empirical covariance from the true covariance \mathbf{C} .

In the next three sections, we use toy models to investigate the effects of weighting matrices on signal loss by experimenting with different matrices \mathbf{R} and examining their impact on the resulting power spectrum estimates $\hat{\mathbf{P}}$. Our goal in experimenting with weighting is to suppress foregrounds and investigate EoR losses associated with it. We note that we purposely take a thorough and pedagogical approach to describing the toy model examples given in the next few sections. The specifics of how signal loss appears in PAPER’s analysis is later described in Chapter 3.

As a brief preview, we summarize our findings in the following sections here:

- If the covariance matrix is estimated from the data, a strong correlation between the estimated modes and the data will in general produce an estimate of the signal power spectrum which is strongly biased *low* relative to the true value. In this context, this is what we call “signal loss” (Chapter 2.2.2).
- The effect of the bias is worsened when the number of independent samples used to estimate the covariance matrix is reduced (Chapter 2.2.3).
- The rate at which empirical eigenvectors converge to their true forms depends on the sample variance in the empirical estimate and the shape of the empirical eigenspectrum. In general, larger sample variances lead to more loss (Chapter 2.2.3).
- Knowing these things, there are some simple ways of altering the empirical covariance matrix to decouple it from the data and produce unbiased power spectrum estimates (Chapter 2.2.4).

2.2.2 Empirical Inverse Covariance Weighting

Using a toy model, we will now build intuition into how weighting by the inverse of the empirically estimated covariance, $\hat{\mathbf{C}}^{-1}$, can give rise to signal loss. We construct a simple dataset that contains visibility data with 100 time integrations and 20 frequency channels. This model represents realistic dimensions of about an hour of PAPER data which might be used for a power spectrum analysis. For PAPER-64 (both the A15 analysis and our new

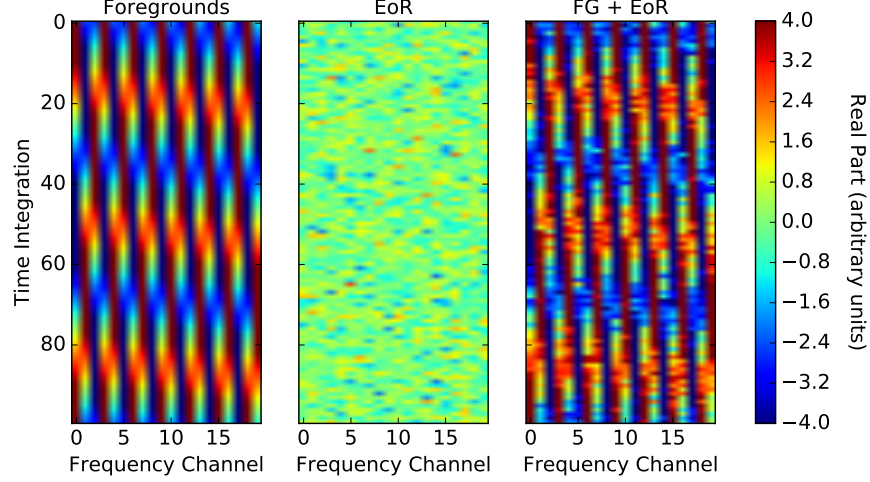


Figure 2.1: Our toy model dataset to which we apply different weighting schemes to in order to investigate signal loss. We model a mock foreground-only visibility with a sinusoid signal that varies smoothly in time and frequency. We model a mock visibility of an EoR signal as a random Gaussian signal. We add the two together to form $\mathbf{x} = \mathbf{x}_{\text{FG}} + \mathbf{x}_{\text{EoR}}$. Real parts are shown here.

analysis) we use ~ 8 hours of data (with channel widths of 0.5 MHz and integration times of 43 seconds), but here we scale it down with no loss of generality.

We create mock visibilities, \mathbf{x} , and assume a non-tracking, drift-scan observation. Hence, flat spectrum sources (away from zenith) lead to measured visibilities which oscillate in time and frequency. We therefore form a mock visibility measurement of a bright foreground signal, \mathbf{x}_{FG} , as a complex sinusoid that varies smoothly in time and frequency, a simplistic but realistic representation of a single bright source. We also create a mock visibility measurement of an EoR signal \mathbf{x}_{EoR} as a complex, Gaussian random signal. A more realistic EoR signal would have a sloped power spectrum in $p(k)$ (instead of flat, as in the case of white noise), which could be simulated by introducing frequency correlations into the mock EoR signal. However, here we treat all k 's separately, so a simplistic white noise approximation can be used. Our combined data vector is then $\mathbf{x} = \mathbf{x}_{\text{FG}} + \mathbf{x}_{\text{EoR}}$, to which we apply different weighting schemes throughout Chapter 2.2. The three data components are shown in Figure 2.1.

We compute the power spectrum of our toy model dataset \mathbf{x} using Equations (2.8) and (2.9), with $\mathbf{R} \equiv \widehat{\mathbf{C}}^{-1}$. Figure 2.2 shows the estimated covariances of our toy model datasets along with the $\widehat{\mathbf{C}}^{-1}$ weighted data. The foreground sinusoid is clearly visible in $\widehat{\mathbf{C}}_{\text{FG}}$. The power spectrum result is shown in green in the left plot of Figure 2.3. Also plotted in the figure are the uniform-weighted ($\mathbf{R} \equiv \mathbf{I}$) power spectrum of the individual components \mathbf{x}_{FG} (blue) and \mathbf{x}_{EoR} (red). As shown, our $\widehat{\mathbf{C}}^{-1}$ weighted result successfully suppresses foregrounds, demonstrated in Figure 2.3 by the missing foreground peak in the weighted

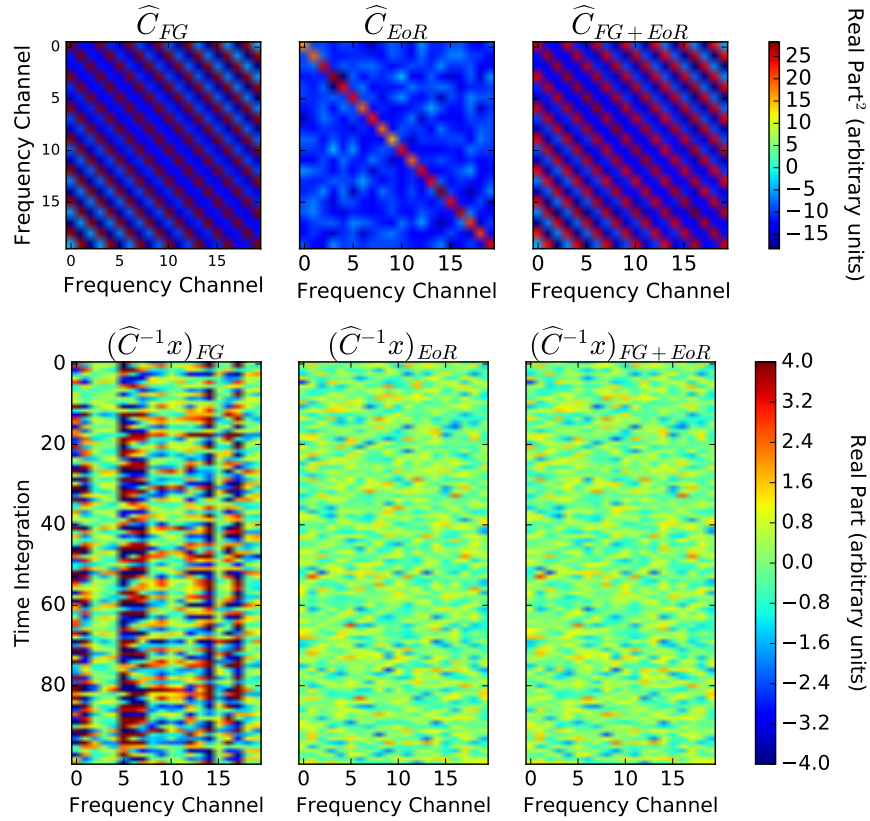


Figure 2.2: The estimated covariance matrices (top row) and inverse covariance-weighted data (bottom row) for FG only (left), EoR only (middle), and FG + EoR (right). Real parts are shown here.

power spectrum estimate (green). It is also evident that our result fails to recover the EoR signal — it exhibits the correct shape, but the amplitude level is slightly low. It is this behavior which we describe as signal loss.

As discussed in Chapter 2.2.1, this behavior is *not* expected in the case that we were to use a true \mathbf{C}^{-1} weighting. Rather, we would obtain the behavior shown in the toy model in Chapter 2.3.1¹, with suppression of the foreground mode resulting in a nearly unbiased estimate of the power spectrum. The key difference is that since $\widehat{\mathbf{C}}$ is estimated from the data, its eigenvectors and eigenvalues are strongly coupled to the particular data realization that was used to compute it, and this coupling leads to loss.

For the case of an eigenmode which can be safely assumed to be predominantly a foreground, its presence in the true covariance matrix will result in the desired suppression via a kind of projection; whether or not it is strongly correlated with the actual data vector is irrelevant. However, in the case of an empirically estimated covariance matrix, the eigen-

¹Note that there the true covariance matrix is also the sum of a diagonal portion describing the signal, and a single mode describing the contaminant (similar to Figure 2.2).

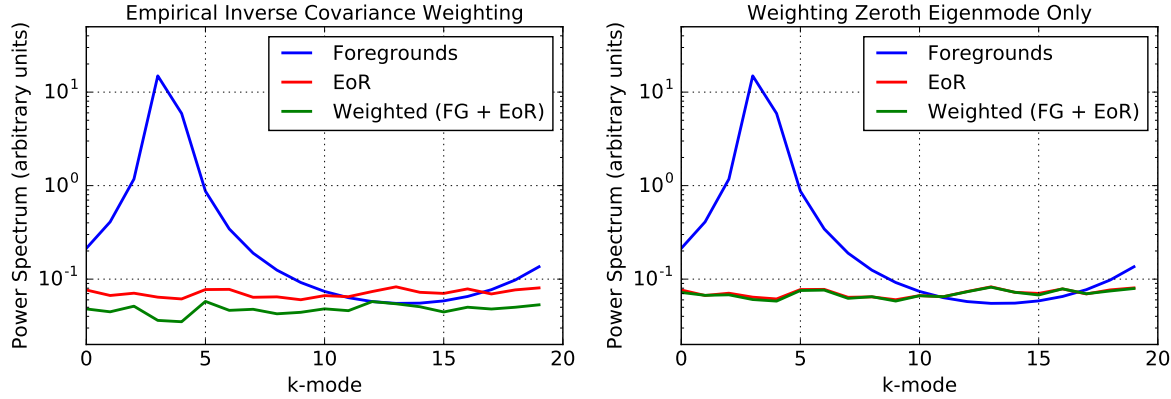


Figure 2.3: Resulting power spectrum estimates for the toy model simulation described in Chapter 2.2.2 — foregrounds only (blue), EoR only (red), and the weighted FG + EoR dataset (green). The power spectrum of the foregrounds peaks at a k -mode based on the frequency of the sinusoid used to create the mock FG signal. In the two panels, we compare using empirically estimated inverse covariance weighting where \mathbf{C} is derived from the data (left), and projecting out the zeroth eigenmode only (right). In the former case, signal loss arises from the coupling of the eigenmodes of $\widehat{\mathbf{C}}$ to the data. There is negligible signal loss when all eigenmodes besides the foreground one are no longer correlated with the data.

modes of $\widehat{\mathbf{C}}_{\text{EoR}}$ will both be incorrect and can be correlated with the data. If these incorrect eigenmodes are not correlated with the data, it will lead to non-minimum variance estimates but will not produce the suppression of the power spectrum amplitude as seen in the left plot of Figure 2.3. As shown mathematically in Chapter 2.3.2, however, if $\widehat{\mathbf{C}}_{\text{EoR}}$ is correlated with the data vector \mathbf{x} , there is a kind of projection of power in the *non*-foreground modes from the resulting power spectrum estimate, thus producing an estimate that is biased low. In short, *if the covariance is computed from the data itself, it carries the risk of overfitting information in the data and introducing a multiplicative bias (per k) to estimates of the signal.*

The danger of an empirically estimated covariance matrix comes mostly from not being able to describe the EoR-dominated eigenmodes of \mathbf{C} accurately, for which the EoR signal is brighter than foregrounds. In such a case, the coupling between these modes to the data realization leads to the overfitting and subtraction of the EoR signal. More specifically, the coupling between the estimated covariance and the data is anti-correlated in nature (which is explained in more detail in Chapters 2.3.2 and ??), which leads to loss. Mis-estimating \mathbf{C} for EoR-dominated eigenmodes is therefore more harmful than for FG-dominated modes, and since the lowest-valued eigenmodes of an eigenspectrum are typically EoR-dominated, using this part of the spectrum for weighting is most dangerous.

Armed with this information, we can tweak the covariance in a simple way to suppress foregrounds and yield minimal signal loss. Recall that our toy model foreground can be perfectly described by a single eigenmode. Using the full dataset's (foreground plus EoR

signal) empirical covariance, we can project out the zeroth eigenmode and then take the remaining covariance to be the identity matrix. This decouples the covariance from the data for the EoR modes. The resulting power spectrum estimate for this case is shown in the right plot of Figure 2.3. In this case we recover the EoR signal, demonstrating that if we can disentangle the foreground-dominated modes and EoR-dominated modes, we can suppress foregrounds with negligible signal loss.

Altering $\hat{\mathbf{C}}$ as such is one specific example of a regularization method for this toy model, in which we are changing $\hat{\mathbf{C}}$ in a way that reduces its coupling to the data realization. There are several other simple ways to regularize $\hat{\mathbf{C}}$, and we will discuss some in Chapter 2.2.4.

2.2.3 Fringe-Rate Filtering

We have shown how signal loss can arise due to the coupling of EoR-dominated eigenmodes to the data. We will next show how this effect is exacerbated by reducing the total number of independent samples in a dataset.

A fringe-rate filter is an analysis technique designed to maximize sensitivity by integrating in time (Parsons et al. 2016). Rather than a traditional box-car average in time, a time domain filter can be designed to up-weight temporal modes consistent with the sidereal motion on the sky, while down-weighting modes that are noise-like.

Because fringe-rate filtering is analogous to averaging in time, it comes at the cost of reducing the total number of independent samples in the data. With fewer independent modes, it becomes more difficult for the empirical covariance to estimate the true covariance matrix of the fringe-rate filtered data. We can quantify this effect by evaluating a convergence metric $\varepsilon(\hat{\mathbf{C}})$ for the empirical covariance, which we define as

$$\varepsilon(\hat{\mathbf{C}}) \equiv \sqrt{\frac{\sum_{ij}(\hat{C}_{ij} - C_{ij})^2}{\sum_{ij} C_{ij}^2}}, \quad (2.12)$$

where \mathbf{C} is the true covariance matrix. To compute this metric, we draw different numbers of realizations (different draws of Gaussian noise) of our toy model EoR measurement, \mathbf{x}_{EoR} , and take their ensemble average. We then compare this to the “true” covariance, which in our simulation is set to be the empirical covariance after a large number (500) of realizations. As shown in Figure 2.4, we perform this computation for a range of total independent ensemble realizations (horizontal axis) and number of independent samples in the data following time-averaging, or “fringe-rate filtering” (different colors). With more independent time samples (i.e., more realizations) in the data, one converges to the true fringe-rate filtered covariance more quickly.

The situation here with using a finite number of time samples to estimate our covariance is analogous to a problem faced in galaxy surveys, where the non-linear covariance of the matter power spectrum is estimated using a large — but finite — number of expensive simulations. There, the limited number of independent simulations results in inaccuracies in estimated covariance matrices (Dodelson & Schneider 2013; Taylor & Joachimi 2014),

which in turn result in biases in the final parameter constraints (Hartlap et al. 2007). In our case, the empirically estimated covariances are used for estimating the power spectrum, and as we discussed in the previous section (and will argue more thoroughly in Chapters ?? and ??), couplings between these covariances and the data can lead to power spectrum estimates that are biased *low*—which is precisely signal loss. In future work, it will be fruitful to investigate whether advanced techniques from the galaxy survey literature for estimating accurate covariance matrices can be successfully adapted for 21 cm cosmology. These techniques include the imposition of sparsity priors (Padmanabhan et al. 2016), the fitting of theoretically motivated parametric forms (Pearson & Samushia 2016), covariance tapering (Paz & Sánchez 2015), marginalization over the true covariance (Sellentin & Heavens 2016), and shrinkage methods (Pope & Szapudi 2008; Joachimi 2017).

The overall convergence of the covariance is important, but also noteworthy is the fact that different eigenvectors converge to their true forms at different rates. This is illustrated by Figure 2.5, which shows the convergence of eigenvectors in an empirical estimate of a covariance matrix. For this particular toy model, we construct a covariance whose true form combines the same mock foreground from the previous toy models with an EoR component that is modeled as a diagonal matrix with eigenvalues spanning one order of magnitude (more specifically, we construct the EoR covariance as a diagonal matrix in the Fourier domain, where the signal is expected to be uncorrelated; its Fourier transform is then the true covariance of the EoR in the frequency domain, or \mathbf{C}_{EoR}). For different numbers of realizations, we draw random EoR signals that are consistent with \mathbf{C}_{EoR} , add them to the mock foreground data, and compute the combined empirical covariance by averaging over the realizations. The eigenvectors of this empirical covariance are then compared to the true eigenvectors $\hat{\mathbf{v}}$, where we use as a convergence metric $\varepsilon(\hat{\mathbf{v}})$, defined as:

$$\varepsilon(\hat{\mathbf{v}}) \equiv \sqrt{\sum_i^{N_f} |\mathbf{v} - \hat{\mathbf{v}}|_i^2}, \quad (2.13)$$

where N_f is the number of frequencies (20) in the mock data. The eigenmode convergence curves in Figure 2.5 are ranked ordered by eigenvalue, such that “Eigenmode #0” illustrates the convergence of the eigenvector with the largest eigenvalue, “Eigenmode #1” for the second largest eigenvalue, and so on. We see that the zeroth eigenmode — the mode describing the foreground signal — is quickest to converge.

Our numerical test reveals that the convergence rates of empirical eigenvectors is related to the sample variance in our empirical estimate. In general, computing an empirical covariance from a finite ensemble average means that the empirical eigenmodes have sample variances. Consider first a limiting case where all eigenvalues are equal. In such a scenario, any linear combination of eigenvectors is also an eigenvector, and thus there is no sensible way to define the convergence of eigenvectors. In our current test, aside from the zeroth mode, the eigenvalues have similar values but are not precisely equal. Hence, there is a well-defined set of eigenvectors to converge to. However, due to the sample variance of our empirical covariance estimate, there may be accidental degeneracies between modes, where

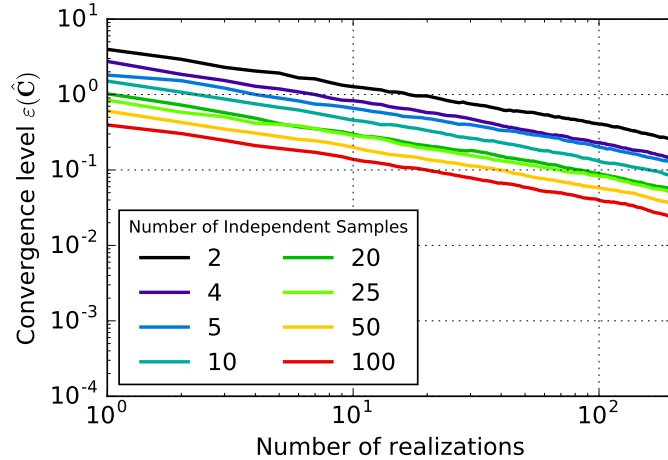


Figure 2.4: The convergence level, as defined by Equation (2.12), of empirically estimated covariances of mock EoR signals with different numbers of independent samples. In red, the mock EoR signal is comprised entirely of independent samples (100 of them). Subsequent colors show time-averaged signals. As the number of realizations increases, we see that the empirical covariances approach the true covariances. With more independent samples, the quicker an empirical covariance converges (i.e., the quicker it decouples from the data), and the less signal loss we would expect to result.

some modes are mixing and swapping with others. Therefore, the steeper an eigenspectrum, the easier it is for the eigenmodes to decouple from each other and approach their true forms. A particularly drastic example of this can be seen in the behavior of mode 0 (the foreground mode), whose eigenvalue differs enough from the others that it is able to converge reasonably quickly despite substantial sample variance in our empirical covariance estimate. To break degeneracies in the remaining modes, however, requires many more realizations.

While the connection between the rate of convergence of an empirical eigenvector with the sample variance of an eigenspectrum is interesting, it is also important to note that regardless of convergence rate, any mode that is coupled to the data is susceptible to signal loss. The true eigenvectors are not correlated with the data realizations; thus, if our empirical eigenvectors are converged fully, there will not be any signal loss. However, an unconverged eigenvector estimate will retain some memory of the data realizations used in its generation, leading to signal loss.

In the toy models throughout Chapter 2.2, we exploit the fact that the strongest eigenmode (highest eigenvalue mode) is dominated by foregrounds in order to purposely incur signal loss for that mode. Even for the case of real PAPER data (Chapter 3), we make the assumption that the strongest eigenmodes are likely the most contaminated by foregrounds. However, in general, foregrounds need not be restricted to the strongest eigenmodes, and as we have seen, it is really the degeneracies between modes that determines how quickly they converge, and hence how much signal loss can result.

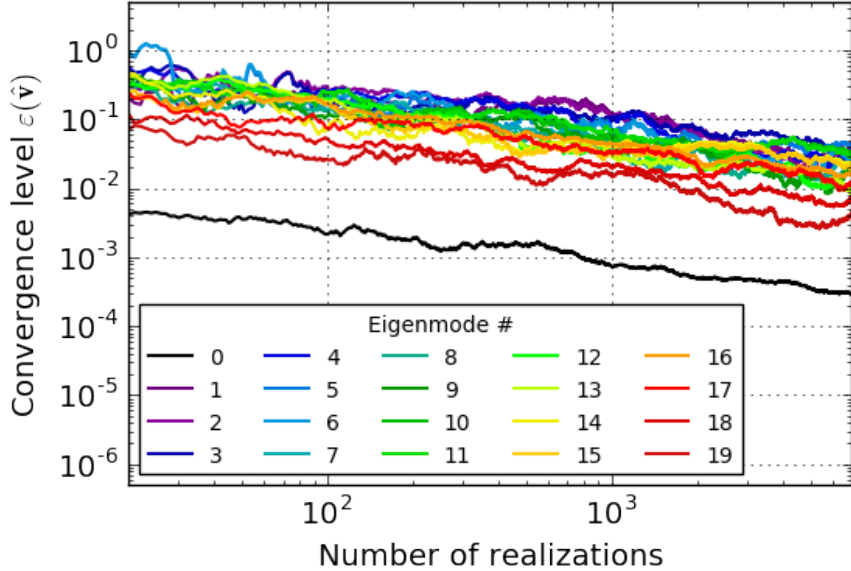


Figure 2.5: The convergence level, as defined by Equation (2.13), of empirically estimated eigenvectors for different numbers of mock data realizations. The colors span from the 0th eigenmode (has the highest eigenvalue) to the 19th eigenmode (has the lowest eigenvalue), where they are ordered by eigenvalue in descending order. This figure shows that the zeroth eigenmode converges the quickest, implying that eigenvectors with eigenvalues that are substantially different than the rest (the FG-dominated mode has a much higher eigenvalue than the EoR modes) are able to converge to the true eigenvectors the quickest. On the other hand, eigenmodes 1-19 have similar eigenvalues and are slower to converge because of degeneracies between them.

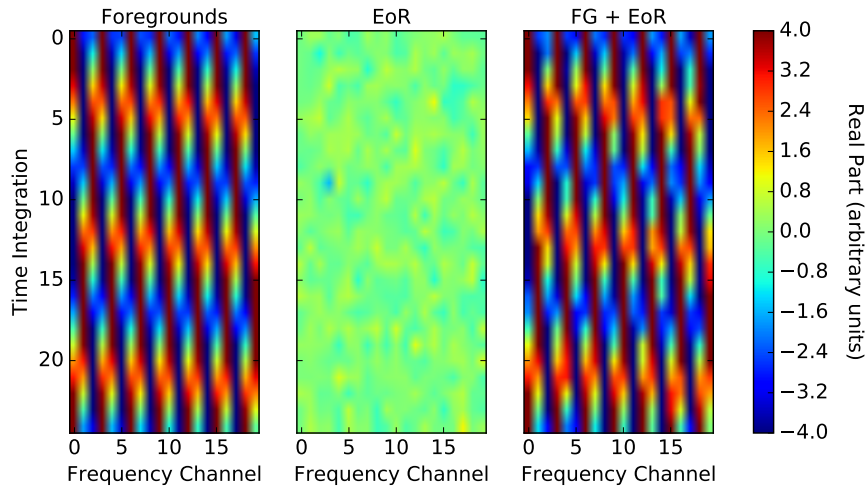


Figure 2.6: Our “fringe-rate filtered” (time-averaged) toy model dataset. We average every four samples together, yielding 25 independent samples in time. Real parts are shown here.

With Figures 2.4 and 2.5 establishing the connection between convergence rates (of empirical covariances and eigenvectors) and number of realizations, we now turn back to our original toy model used in Chapter 2.2.2, which is comprised of a mock foreground and mock EoR signal. We mimic a fringe-rate filter by averaging every four time integrations of our toy model dataset together, yielding 25 independent samples in time (Figure 2.6). We choose these numbers so that the total number of independent samples is similar to the number of frequency channels — hence our matrices will be full rank. We use this “fringe-rate filtered” mock data for the remainder of Chapter 2.2.

The power spectrum results for this model are shown in Figure 2.7, and as expected there is a much larger amount of signal loss for this time-averaged dataset since we do a worse job estimating the true covariance. In addition, as a result of having fewer independent samples, we obtain an estimate with more scatter. This is evident by noticing that the green curve in Figure 2.7 fails to trace the shape of the uniform-weighted EoR power spectrum (red).

Using our toy model, we have seen that a sensitivity-driven analysis technique like fringe-rate filtering has trade-offs of signal loss and noisier estimates when using data-estimated covariance matrices. Longer integrations increase sensitivity but reduce the number of independent samples, resulting in eigenmodes correlated with the data that can overfit signal greatly. We note that a fringe-rate filter does have a range of benefits, many described in Parsons et al. (2016), so it can still be advantageous to use one despite the trade-offs.

2.2.4 Other Weighting Options

In Chapter 2.2.2 we showed one example of how altering $\hat{\mathbf{C}}$ can make the difference between nearly zero and some signal loss. We will now use our toy model to describe several other ways to tailor $\hat{\mathbf{C}}$ in order to minimize signal loss. We choose four independent regularization methods to highlight in this section, which have been chosen due to their simplicity in implementation and straightforward interpretations. We illustrate the resulting power spectra for the different cases in Figure 2.8. These examples are not meant to be taken as suggested analysis methods but rather as illustrative cases.

As a first test, we model the covariance matrix of EoR as a proof of concept that if perfect models are known, signal loss can be avoided. We know that our simulated EoR signal should have a covariance matrix that mimics the identity matrix, with its variance encoded along the diagonal. We model \mathbf{C}_{EoR} as such (i.e., the identity), instead of computing it based on \mathbf{x}_{EoR} itself. Next, we add $\mathbf{C}_{\text{EoR}} + \hat{\mathbf{C}}_{\text{FG}}$ (where $\hat{\mathbf{C}}_{\text{FG}} = \langle \mathbf{x}_{\text{FG}} \mathbf{x}_{\text{FG}}^\dagger \rangle_t$) to obtain a final $\hat{\mathbf{C}}_{\text{reg}}$ (regularized empirical covariance matrix) to use in weighting. In Figure 2.8 (upper left), we see that there is negligible signal loss. This is because by modeling \mathbf{C}_{EoR} , we avoid overfitting EoR fluctuations in the data that our model doesn’t know about (but, an empirically derived $\hat{\mathbf{C}}_{\text{EoR}}$ would know about the fluctuations). In practice such a weighting option is not feasible, as it is difficult to model \mathbf{C}_{EoR} , and $\hat{\mathbf{C}}_{\text{FG}}$ is unknown because we do not know how to separate out the foregrounds from the EoR in our data.

The second panel (top right) in Figure 2.8 uses a regularization method of setting $\hat{\mathbf{C}}_{\text{reg}} \equiv$

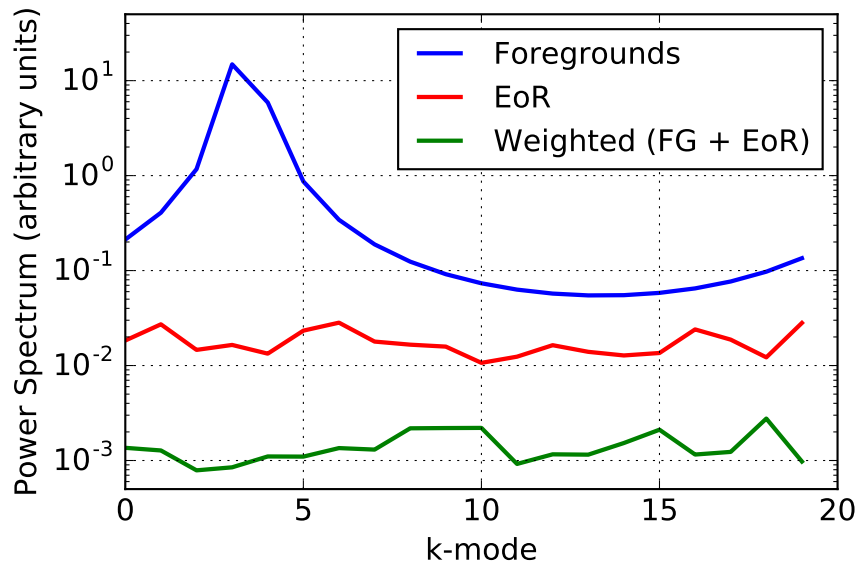


Figure 2.7: Resulting power spectrum estimate for the “fringe-rate filtered” (time-averaged) toy model simulation — foregrounds only (blue), EoR only (red), and the weighted FG + EoR dataset (green). We use empirically estimated inverse covariance weighting where \mathbf{C} is computed from the data. There is a larger amount of signal loss than for the non-averaged data, a consequence of weighting by eigenmodes that are more strongly coupled to the data due to there being fewer independent modes in the data.

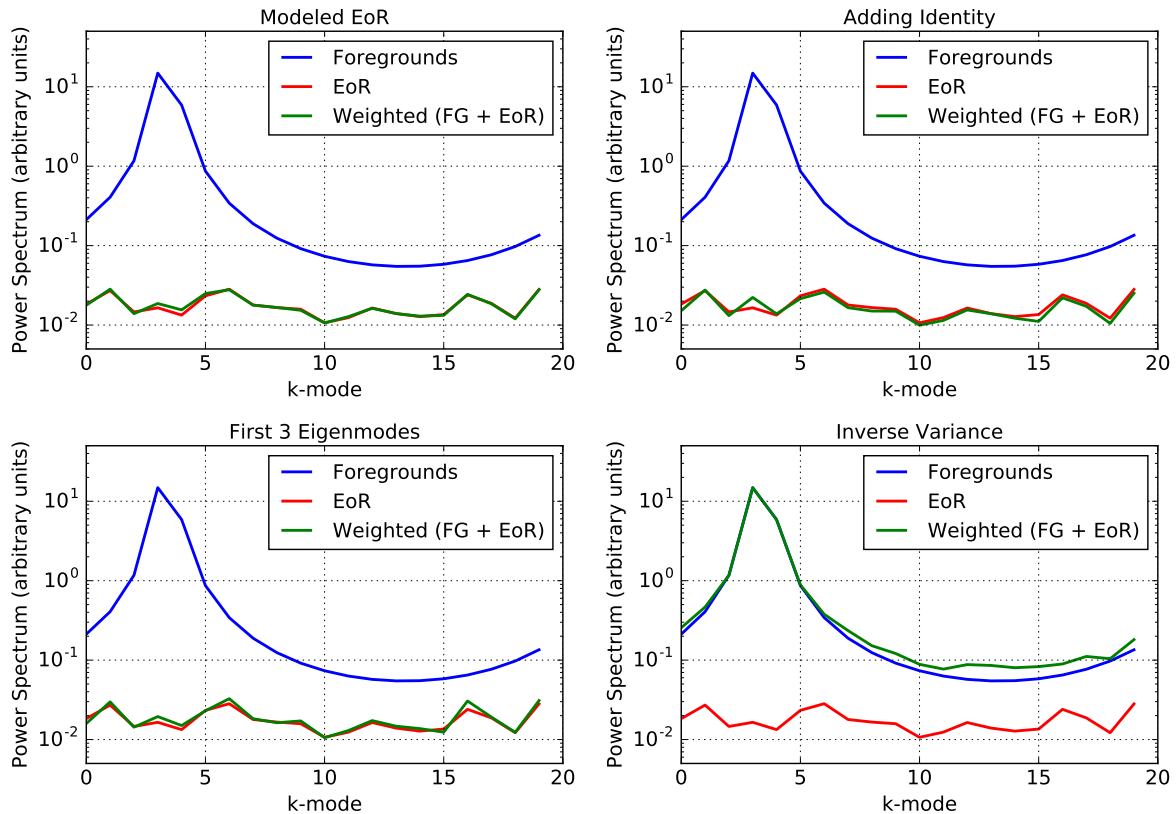


Figure 2.8: Resulting power spectra estimates for our “fringe-rate filtered” (time-averaged) toy model simulation — foregrounds only (blue), EoR only (red), and the weighted FG + EoR dataset (green). We show four alternate weighting options that each minimize signal loss, including modeling the covariance matrix of EoR (upper left), regularizing $\hat{\mathbf{C}}$ by adding an identity matrix to it (upper right), using only the first three eigenmodes of $\hat{\mathbf{C}}$ (lower left), and keeping only the diagonal elements of $\hat{\mathbf{C}}$ (lower right). The first case (upper left) is not feasible in practice since we do not know \mathbf{C}_{FG} and \mathbf{C}_{EoR} like we do in the toy model.

$\widehat{\mathbf{C}} + \gamma \mathbf{I}$, where $\gamma = 5$ (an arbitrary strength of \mathbf{I} for the purpose of this toy model). By adding the identity matrix, element-wise, we are weighting the diagonal elements of the estimated covariance matrix more heavily than those off-diagonal. Since the identity component does not know anything about the data realization, it alters the covariance to be less coupled to the data and there is no loss.

The third panel (bottom left) in Figure 2.8 minimizes signal loss by only using the first three eigenmodes of the estimated covariance. Recalling that our toy model foregrounds can be described entirely by the zeroth eigenmode, this method intentionally projects out the highest-valued modes only by replacing all but the three highest weights in the eigenspectrum with 1's (equal weights). Again, avoiding the overfitting of EoR-dominated modes which are coupled to the data results in negligible signal loss. While this case is illuminating for the toy model, in practice it is not obvious which eigenmodes are foreground or EoR dominated (and they could be mixed as well), so determining which subset of modes to down-weight is not trivial. We experiment with this idea using PAPER data in Chapter ??.

The last regularization scheme we are highlighting here is setting $\widehat{\mathbf{C}}_{\text{reg}} \equiv \widehat{\mathbf{C}} \circ \mathbf{I}$ (element-wise multiplication), or inverse variance weighting (i.e., keeping only the diagonal elements of $\widehat{\mathbf{C}}$). In the bottom right panel of Figure 2.8, we see that this method does not down-weight the foregrounds at all — this regularization altered $\widehat{\mathbf{C}}$ in a way where it is no longer coupled to *any* of the empirically estimated eigenmodes, including the FG-dominated one. To understand this, we recall that our foregrounds are spread out in frequency and therefore have non-negligible frequency-frequency correlations. Multiplying by the identity matrix, element-wise, results in a diagonal matrix, meaning we do not have any correlation information. Because of this, we do a poor job suppressing the foreground. But because we decoupled the whole eigenspectrum from the data, we also avoid signal loss. Although this method did not successfully recover the EoR signal for this particular simulation, it is important that we show that there are many options for estimating a covariance matrix, and some may down-weight certain eigenmodes more effectively than others based on the spectral nature of the components in a dataset.

In summary, we have shown how signal loss is caused by weighting a dataset by itself, and in particular how estimated covariances can overfit EoR modes when they are coupled to data and not converged to their true forms. We have also seen that there are trade-offs between a chosen weighting method, its foreground-removal effectiveness, the number of independent samples in a dataset, and the amount of resulting signal loss.

2.3 Signal Loss Mathematical Framework

In Chapter 2.2.1, we argued that the optimal quadratic estimator method has the effect of projecting out foreground modes that have a different covariance structure than the EoR signal. And in Chapter 2.2.2, we saw that *empirical* inverse covariance weighting can lead to loss via a multiplicative bias to estimates of the signal. To support these arguments, we now present two mathematical frameworks in which we use toy models in order to illustrate

these conclusions analytically.

2.3.1 A Toy Model for Inverse Covariance Weighting

In this section, we focus on the optimal quadratic estimator, Equation (2.3), and mathematically illustrate its role in estimating the power spectrum of EoR. While there exists detailed literature about quadratic estimators in general (e.g., Liu & Tegmark 2011; Trott et al. 2012; Liu et al. 2014b; Dillon et al. 2014), here we focus on two simple cases in order to outline one situation where the estimator successfully suppresses contamination and one where it does not. By describing these two cases, we hope to clarify and motivate the desire to use OQE while also understanding its limitations.

In our toy model, we specifically choose toy models where the data covariance is diagonal, as indeed we expect the EoR signal to be. We assume we have N data points Δ_i which are the sum of a desired signal σ_i and an undesired contaminant v_i

$$\Delta_i = \sigma_i + v_i \quad (2.14)$$

with

$$\langle \sigma_i \rangle = 0; \langle \sigma_i^2 \rangle = s; \text{ and } \langle \boldsymbol{\sigma} \boldsymbol{\sigma}^T \rangle = s \mathbf{I}_{N \times N} \equiv \mathbf{S}, \quad (2.15)$$

where we wish to estimate s . The contaminant in this first case has a similar structure (as the EoR) for its covariance, and is assumed uncorrelated with the signal

$$\langle v_i \rangle = 0; \langle v_i^2 \rangle = u; \langle \mathbf{v} \mathbf{v}^T \rangle = u \mathbf{I}_{N \times N} \equiv \mathbf{U}; \text{ and } \langle \sigma_i v_j \rangle = 0. \quad (2.16)$$

With the covariance matrix given by $\mathbf{C} = \mathbf{S} + \mathbf{U}$, the estimator for s using only the quadratic part of Equation 2.3 is

$$\hat{s} = \frac{\boldsymbol{\Delta}^T \boldsymbol{\Delta}}{N} \quad (2.17)$$

and its expectation is

$$\langle \hat{s} \rangle = s + u. \quad (2.18)$$

Thus, when the covariance structure of the contaminant is identical to the signal ($\frac{\partial \mathbf{S}}{\partial s} = \frac{\partial \mathbf{U}}{\partial u} = \frac{\partial \mathbf{C}}{\partial s}$), the information available to the quadratic portion of the estimator to distinguish between the two is degenerate, and knowledge only of \mathbf{C} and $\frac{\partial \mathbf{C}}{\partial s}$ is inadequate. In order to obtain an unbiased estimate of s , one must also use knowledge of \mathbf{U} . Indeed, computing the linear bias from Equation (2.6), one finds $b = u$.

Now consider a case, chosen to be very similar to the toy model in 2.2.2, in which the data again have an additive contaminant, now given by

$$\Delta_i = \sigma_i + v m_i \quad (2.19)$$

where the properties of σ_i are as before, but now v is a random variable and m_i is a fixed function of i with

$$\langle v \rangle = 0; \langle v^2 \rangle = u; \langle \mathbf{v} \mathbf{v}^T \rangle = u \mathbf{m} \mathbf{m}^T \equiv \mathbf{U}; \mathbf{m}^T \mathbf{m} = 1; \text{ and } \langle \sigma_i v \rangle = 0. \quad (2.20)$$

Here \mathbf{m} represents a mode which is correlated across many data points (i.e., we are assuming \mathbf{U} need *not* be diagonal), with amplitude given by v . The normalization of \mathbf{m} is a matter of convention, and can be absorbed in the variance u ; the choice above will be convenient for understanding the limiting case $u \gg s$.

We can calculate the quadratic portion of the estimator explicitly by using the Sherman-Morrison identity to invert the covariance matrix. Defining

$$\xi \equiv \frac{u/s}{1 + u/s}, \quad (2.21)$$

we have

$$\mathbf{C}^{-1} = \frac{1}{s} (\mathbf{I} - \xi \mathbf{m} \mathbf{m}^T) \quad (2.22)$$

and

$$\hat{s} = \frac{\Delta^T (\mathbf{I} + (\xi^2 - 2\xi) \mathbf{m} \mathbf{m}^T) \Delta}{N + \xi^2 - 2\xi} \quad (2.23)$$

with expectation

$$\langle \hat{s} \rangle = s + \frac{1 - 2\xi + \xi^2}{N + -2\xi + \xi^2} u. \quad (2.24)$$

It is worth observing immediately that there is no multiplicative bias on s , and that the additive bias is strictly $< u/N$.

An instructive limit is $u \gg s$, $\xi \rightarrow 1$, in which case the virtue of weighting by \mathbf{C}^{-1} becomes clearer, as it becomes

$$\mathbf{C}^{-1} = \frac{1}{s} (\mathbf{I} - \mathbf{m} \mathbf{m}^T) \quad (2.25)$$

where $\mathbf{I} - \mathbf{m} \mathbf{m}^T$ is the projection operator, projecting out \mathbf{m} from any vector it acts on, and further, the linear bias tends to 0 as $\xi \rightarrow 1$ (i.e., the projection is “perfect” and not “undone” by the Fisher matrix normalization).

This is the ideal case for the inverse covariance weighting performed in the PAPER analysis, where removal of contamination with a known covariance can be suppressed by a kind of projection of the offending modes. But even in this case, it is worth pointing out that the estimator still has a linear bias for finite u . We have also assumed that the contaminating mode \mathbf{m} is known perfectly; the next section takes up the case where the modes are estimated from the data.

2.3.2 A Toy Model for Signal Loss

In this section, we examine a toy model for signal loss. Our goal is to derive an analytic formula for power spectrum signal loss. While this model does not apply generally to all the scenarios presented in this work, it provides some analytic intuition for how the coupling between data and an empirical covariance can result in signal loss.

The minimum-variance quadratic estimator \widehat{P}^α for the α th bandpower of the power spectrum is given by

$$\widehat{P}^\alpha = \frac{1}{2\mathbf{F}^{\alpha\alpha}} \mathbf{x}^t \mathbf{C}^{-1} \mathbf{Q}^\alpha \mathbf{C}^{-1} \mathbf{x}, \quad (2.26)$$

where

$$F^{\alpha\alpha} \equiv \frac{1}{2} \text{tr} (\mathbf{C}^{-1} \mathbf{Q}^\alpha \mathbf{C}^{-1} \mathbf{Q}^\alpha) \quad (2.27)$$

is the α th diagonal element of the Fisher matrix. For this section only, with no loss of generality, we assume that the data \mathbf{x} are real. We also assume for simplicity that \mathbf{x} is the data from a single instant in time, so that it is of length N_f , where N_f is the number of frequency channels.

In our case, we do not have *a priori* knowledge of the covariance matrix. Thus, we deviate from the true minimum-variance quadratic estimator and replace \mathbf{C} with $\widehat{\mathbf{C}}$, its data-derived approximation. Our estimator then becomes

$$\widehat{P}_{\text{loss}}^\alpha = \frac{1}{2\widehat{F}^{\alpha\alpha}} \mathbf{x}^t \widehat{\mathbf{C}}^{-1} \mathbf{Q}^\alpha \widehat{\mathbf{C}}^{-1} \mathbf{x}, \quad (2.28)$$

where

$$\widehat{F}^{\alpha\alpha} \equiv \frac{1}{2} \text{tr} (\widehat{\mathbf{C}}^{-1} \mathbf{Q}^\alpha \widehat{\mathbf{C}}^{-1} \mathbf{Q}^\alpha), \quad (2.29)$$

with the label “loss” to foreshadow the fact that this will be an estimator with signal loss (i.e., a multiplicative bias of less than unity). We will now provide an explicit demonstration of this by modeling the estimated covariance as

$$\widehat{\mathbf{C}} = (1 - \eta) \mathbf{C} + \eta \mathbf{x} \mathbf{x}^t, \quad (2.30)$$

where η is a parameter quantifying our success at estimating the true covariance matrix. If $\eta = 0$, our covariance estimate has perfectly modeled the true covariance and $\widehat{\mathbf{C}} = \mathbf{C}$. On the other hand, if $\eta = 1$, then our covariance estimate is based purely on the one realization of the covariance that is our actual data, and we would expect a high level of overfitting and signal loss.

Our strategy for computing the signal loss will be to insert Equation (2.30) into Equation (2.28) and to express the resulting estimator $\widehat{P}_{\text{loss}}^\alpha$ in terms of \widehat{P}^α . We begin by expressing $\widehat{\mathbf{C}}^{-1}$ in terms of \mathbf{C}^{-1} using the Woodbury identity so that

$$\widehat{\mathbf{C}}^{-1} = \frac{\mathbf{C}^{-1}}{1 - \eta} \left[\mathbf{I} - \frac{\eta \mathbf{x} \mathbf{x}^t \mathbf{C}^{-1}}{1 + \eta(g - 1)} \right], \quad (2.31)$$

where we have defined $g \equiv \mathbf{x}^t \mathbf{C}^{-1} \mathbf{x}$. Inserting this into our Fisher estimate we have

$$\widehat{F}^{\alpha\alpha} = \frac{F^{\alpha\alpha}}{(1 - \eta)^2} \left[1 - \frac{\eta}{1 + \eta(g - 1)} \frac{h^{\alpha\alpha}}{F^{\alpha\alpha}} + \frac{1}{2} \left(\frac{\eta}{1 + \eta(g - 1)} \right)^2 \frac{(h^\alpha)^2}{F^{\alpha\alpha}} \right], \quad (2.32)$$

where $h^\alpha \equiv \mathbf{x}^t \mathbf{C}^{-1} \mathbf{Q}^\alpha \mathbf{C}^{-1} \mathbf{x}$ and $h^{\alpha\alpha} \equiv \mathbf{x}^t \mathbf{C}^{-1} \mathbf{Q}^\alpha \mathbf{C}^{-1} \mathbf{Q}^\alpha \mathbf{C}^{-1} \mathbf{x}$. Note that g , h^α , and $h^{\alpha\alpha}$ are all random variables, since they depend on \mathbf{x} . Inserting these expressions into our estimator gives

$$\widehat{P}_{\text{loss}}^\alpha = \frac{1}{2} \frac{h^\alpha}{F^{\alpha\alpha}} \left[1 - \frac{\eta g}{1 + \eta(g-1)} \right]^2 \left[1 - \frac{\eta}{1 + \eta(g-1)} \frac{h^{\alpha\alpha}}{F^{\alpha\alpha}} + \frac{1}{2} \left(\frac{\eta}{1 + \eta(g-1)} \right)^2 \frac{(h^\alpha)^2}{F^{\alpha\alpha}} \right]^{-1}. \quad (2.33)$$

Both for the purposes of analytical tractability and to provide intuition, we expand this expression to leading order in η . This approximates the limiting case where the covariance $\widehat{\mathbf{C}}$ is close to the ideal and the lossy covariance is a small perturbation. The result is

$$\widehat{P}_{\text{loss}}^\alpha \approx \frac{1}{2} \frac{h^\alpha}{F^{\alpha\alpha}} \left[1 - \eta \left(g - \frac{h^{\alpha\alpha}}{F^{\alpha\alpha}} \right) \right]. \quad (2.34)$$

Taking the ensemble average of both sides and noting that the true power spectrum P^α is equal to $\langle h^\alpha \rangle / 2F^{\alpha\alpha}$, we obtain

$$\langle \widehat{P}_{\text{loss}}^\alpha \rangle \approx (1 - \eta N_f) P^\alpha + 4\eta \frac{\text{tr}(\mathbf{C}^{-1} \mathbf{Q}^\alpha \mathbf{C}^{-1} \mathbf{Q}^\alpha \mathbf{C}^{-1} \mathbf{Q}^\alpha)}{[\text{tr}(\mathbf{C}^{-1} \mathbf{Q}^\alpha \mathbf{C}^{-1} \mathbf{Q}^\alpha)]^2} \approx (1 - \eta N_f) P^\alpha, \quad (2.35)$$

where recall that N_f is the length of \mathbf{x} , or the number of frequency channels. In the last step we dropped the final term, since it scales as ηP^α (without the factor of N) and is therefore typically small compared to the terms that have been retained.

Recalling that P^α is the *true* power spectrum, one sees that when the covariance in the optimal quadratic estimator is naively replaced by an empirical covariance, the resulting power spectrum estimate is biased low, i.e., there is signal loss. This occurs because of couplings between $\widehat{\mathbf{C}}$ and \mathbf{x} , which formally means that what was originally a quadratic estimator is no longer quadratic, but contains higher-order correlations. This violates the assumptions implicit in the derivation of $F^{\alpha\alpha}$ as the normalization factor for converting unnormalized bandpowers $\frac{1}{2} \mathbf{x}^t \mathbf{C}^{-1} \mathbf{Q}^\alpha \mathbf{C}^{-1} \mathbf{x}$ into properly normalized power spectrum estimates, where the unnormalized bandpowers are assumed to be two-point (i.e., quadratic) statistics (Liu & Tegmark 2011). The result is an improperly normalized—and thus lossy—power spectrum estimate.

2.4 Error Estimation Toy Model

Our second major 21 cm power spectrum theme is error estimation, as we desire robust methods for determining accurate confidence intervals for our measurements. Two popular ways of calculating errors on a power spectrum measurement are calculating the variance of power spectrum results, and computing a theoretical error estimate based on an instrument’s system temperature and observational parameters. In a perfect world, both methods would match up. However, in practice the two do not always agree due to a number of factors,

including possible non-Gaussianities in the noise properties of our instruments and possible systematics in the data.

A third option which acts as a middle ground between purely theoretical and purely empirical errors is using Gaussian error. This involves the assumption of Gaussianity, but allows the variance of the power spectrum estimator to be written as a function of the two-point estimator, or covariance. One could empirically calculate the covariance and then propagate it into an analytic expression to compute the errors, making this method fall somewhere between being fully empirical and fully modeled (see [Das et al. \(2011b\)](#) for an example of its implementation).

For PAPER’s analysis, we choose a data-driven method of error estimation that does not rely on assumptions of Gaussianity. Namely, we compute error bars that have been derived from the inherent variance of our measurements. A common technique used to do this is bootstrapping. For pedagogical purposes, we first define the technique of bootstrapping and then illustrate one of its pitfalls through a toy model.

Bootstrapping uses sampling with replacement to estimate a posterior distribution. For example, measurements (like power spectra) can be made from different samples of data. Each of these measurements is a different realization drawn from some underlying distribution, and realizations are correlated with each other to a degree set by the fraction of sampled points that are held in common between them. Through the process of re-sampling and averaging along different axes of a dataset, such as along baselines or times, we can estimate error bars for our results which represent the underlying distribution of values that are allowed by our measurements ([Efron & Tibshirani 1994](#); [Andrae 2010](#)).

Suppose we have N different measurements targeting the same quantity (for example, N power spectrum measurements). Bootstrapping means that we form N_{boot} (often a large number) bootstraps, where each bootstrap is a random selection of the N measurements. Bootstraps each have dimensions of N , and the values populated into each bootstrap are drawn from the original set of measurements with replacement (i.e., every n^{th} slot in N is filled randomly for each bootstrap). Next we take the mean of each bootstrap to collapse it from an array of length N to a single number (we are interested in the mean statistic here, but any function of interest can be applied to each bootstrap as long as it’s the same function for each one). The error (on the mean) is then computed as the standard deviation across all bootstraps.

We must be careful in distinguishing N_{boot} , the number of bootstraps, from N , the number of samples, or elements, or values, that comprise a bootstrap. In the toy models presented in this section, N_{boot} is typically large, and the standard deviation across bootstraps (the error we are computing) converges for large N_{boot} . Typically N is a straightforward value to set that just depends on the experiment. However, we will illustrate one case in which it is not simply the number of samples along the axis that is being re-sampled. More specifically, we will see that N depends on sample independence and may not always be straightforward to approximate.

For our toy model, suppose we have a Gaussian random signal dataset of length $N = 1000$ and unity variance (zero mean). This could represent 1000 power spectrum measurements,

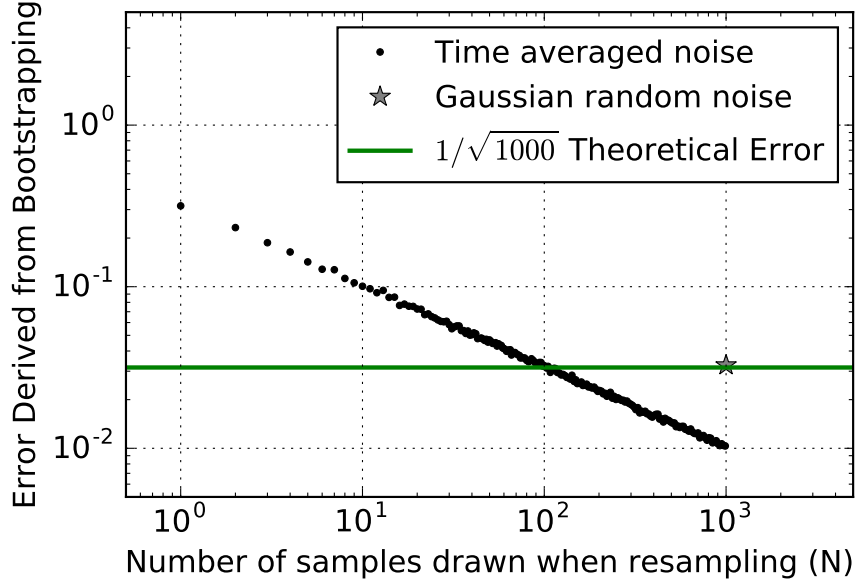


Figure 2.9: Error estimation from bootstrapping as a function of the number of elements drawn per bootstrap when sampling with replacement. The star represents the standard deviation of $N_{\text{boot}} = 500$ bootstraps, each created by drawing 1000 elements (with replacement) from a length 1000 array of a Gaussian random signal. The black points correspond to time-averaged data (correlated data) which has 100 independent samples. They illustrate how errors can be under-estimated if drawing more elements than there are independent samples in the data. The estimated errors match up with the theoretical prediction only at $N = 100$.

for which we are interested in its error. We predict that the error on the mean should obey $1/\sqrt{N}$, where N is the number of samples.

We next form 500 bootstraps ($N_{\text{boot}} = 500$). To create each bootstrap, we draw N samples, with replacement, of the original data, and take the mean over the N samples. The standard deviation over the 500 bootstraps gives an error estimate for our dataset. This error is indicated by the gray star in Figure 2.9 and matches our theoretical prediction (green).

One major caveat of bootstrapping arises when working with correlated data. If, for example, a dataset has many repeated values inside it, this would be reflected in each bootstrap. The same value would be present multiple times within a bootstrap and also be present between bootstraps, purely because it has a more likely chance of being drawn if there are repeats of itself. Therefore, bootstrapping correlated data results in a smaller variation between bootstraps, and hence, under-estimates errors. The use of a fringe-rate filter, which averages data in time to increase sensitivity, is one example which leads to a reduction in the number of independent samples, creating a situation in which errors can be under-estimated. We will now show this effect using our toy model.

Going back to our toy model, we apply a sliding boxcar average to 10 samples at a time,

thus reducing the number of independent data samples to $N/10 = 100$. Bootstrapping this time-averaged noise, using the same method as described earlier (drawing $N = 1000$ elements per bootstrap sample), under-estimates the error by a factor of ~ 3 (black points in Figure 2.9, at $N = 1000$). This occurs because we are drawing more samples than independent ones available, and thus some samples are repeated multiple times in all bootstraps, leading to less variation between the bootstraps. In fact, the error derived from bootstrapping is a strong function of the number of elements that are drawn per bootstrap (Figure 2.9, black points), and we can both under-estimate the error by drawing too many or over-estimate it by drawing too few. However, since we know that we have 100 independent samples in this toy model, the error associated with drawing $N = 100$ samples with replacement does match the theoretical prediction as expected (the black points cross the green line at $N = 100$ in Figure 2.9).

This example highlights the importance of understanding how analysis techniques (such as fringe-rate filtering) can affect a common statistical procedure like bootstrapping. Bootstrapping as a means of estimating power spectrum errors from real fringe-rate filtered data requires knowledge of the number of independent samples, which is not always a trivial task. For example, computing the effective number of independent samples of fringe-rate filtered data is not as simple as counting the number of averages performed. Down-sampling a time-averaged signal is straightforward using a boxcar average, but non-trivial with a more complicated convolution function that has long tails. Hence, we do not recommend bootstrapping unless the number of independent samples along the axis that is being re-sampled is well-determined. In Chapter ??, we explain how we under-estimated errors in the A15 analysis of PAPER and how our bootstrapping procedure has now changed to avoid the over-sampling of correlated data.

In summary, bootstrapping can be an effective and straightforward way to estimate errors of a dataset. However, we have illustrated a situation in which bootstrapping can lead to under-estimated errors and therefore under-estimated power spectrum limits. We have shown that bootstrapped error depends strongly on the number of elements drawn in a bootstrap sample. Estimated errors can drop to arbitrarily small values when the number of elements drawn exceeds the effective number of independent elements. While bootstrapping is convenient because it provides a way to estimate errors from the data itself, one must assess whether certain analysis choices have compromised the method and whether a variation or an avoidance of traditional re-sampling could be preferred instead.

2.5 Bias Toy Model

In a 21 cm power spectrum, detections could be the EoR signal, but they could also be attributed to other sources of bias. Connecting a detection to EoR as opposed to noise or foreground bias is a key challenge of future 21 cm data analyses (e.g. Petrovic & Oh 2011). In this section we will discuss possible sources of bias in a measurement, as well as techniques that can help mitigate their effects. We will also present a series of tests in a pedagogical

fashion which we suggest be used to help evaluate deep limits and/or detections.

2.5.1 Foreground and Noise Bias

In Chapter 2.2, we discussed signal loss as a form of multiplicative bias to estimates of the signal. Foregrounds are another type of bias, but an additive instead of a multiplicative one. Foreground bias is perhaps one of the main factors limiting 21 cm results, as foreground signals lie $\sim 4\text{-}5$ orders of magnitude above the cosmological signal. Though there are many techniques proposed for removing foregrounds (see e.g. [Vedantham et al. 2012](#); [Chapman et al. 2012](#); [Parsons et al. 2012](#); [Parsons et al. 2012](#); [Dillon et al. 2013](#); [Wang et al. 2013](#); [Parsons et al. 2014](#); [Liu et al. 2014a](#); [Wolz et al. 2014](#); [Liu et al. 2014b](#); [Dillon et al. 2015a](#); [Pober et al. 2016](#); [Trott et al. 2016](#)), most experiments currently remain limited by residuals rather than noise, especially at low k .

One common method to isolate and filter foregrounds is to exploit their behavior in k -space. For a particular baseline length, there is a maximum delay imposed on sources attached to the sky, which corresponds to the light-crossing time between two antennas in a baseline. For longer baselines, this value increases, producing what is known as “the wedge” ([Datta et al. 2010](#); [Parsons et al. 2012](#); [Vedantham et al. 2012](#); [Pober et al. 2013](#); [Thyagarajan et al. 2013](#); [Liu et al. 2014a,b](#); [Patil et al. 2017](#)). The wedge describes a region in k -space contaminated by smooth spectrum foregrounds, bounded by baseline length (which is proportional to k_{\perp}) and delay (which is proportional to k_{\parallel}). Properties of the wedge can be used to isolate and avoid foregrounds, as done by [A15](#), [Parsons et al. \(2014\)](#), [Dillon et al. \(2014\)](#), [Dillon et al. \(2015a\)](#), [Jacobs et al. \(2015\)](#), [Beardsley et al. \(2016\)](#), and [Trott et al. \(2016\)](#).

Although smooth-spectrum foregrounds preferentially show up at low delay, or low k -modes, their isolation within the wedge is not perfect. In deep measurements, power spectrum measurements at k_{\parallel} values beyond the delay associated with the length of a baseline are often still contaminated at a low level. This leakage, particularly at low k 's, can be attributed to convolution kernels associated with Fourier-transforming visibilities into delay-space. In other words, smooth-spectrum foregrounds appear as δ -functions in delay-space, convolved by the Fourier transform of the source spectrum, the signal chain, and the antenna response, all of which could smear out the foregrounds and cause leakage outside the wedge (e.g. [Ewall-Wice et al. 2017](#); [Kerrigan et al. 2018](#)).

There are analysis techniques to mitigate the effects of foreground leakage and prevent information from low k 's from spreading to high k values. For example, narrow window functions in delay-space can be used to minimize the leakage from a particular k value into other ones ([Liu et al. 2014b](#)). In other words, one can construct an estimator using QE that forces a window function to have a minimum response to low k values. The window function used in [A15](#) is constructed in such a way, specifically to prevent foregrounds that live at low k 's from contaminating higher k -modes (see Chapter ??).

Determining the source of positive non-EoR detections at higher k 's is more difficult. In previous power spectrum results, these detections have been explained as instrumental sys-

tematics, particularly time-variable cross talk, RFI, cable reflections, and calibration errors (A15; Parsons et al. 2014; Dillon et al. 2014; Beardsley et al. 2016; Patil et al. 2017). In the next section, we will present some tests that can help distinguish these excesses from that of EoR.

In addition to foreground bias, noise can also be responsible for positive power spectrum detections if thermal noise is multiplied by itself. Every 21 cm visibility measurement contains thermal noise that is comprised of receiver and sky noise. We expect this noise to be independent between antennas and thus we can beat it down (increase sensitivity) by integrating longer, using more baselines, etc. However, the squaring of noise can occur when cross-multiplying visibilities, which is shown by the two copies of \mathbf{x} in Equation (2.8). If both copies of \mathbf{x} come from the same baseline and time, it can result in power spectrum measurements that are higher than those predicted by the thermal noise of the instrument. One way to avoid this type of noise bias is to avoid cross-multiplying data from the same baselines or days. This ensures that the two quantities that go into a measurement have separate noises that don't correlate with each other. We also note that if the noise level is known, this type of bias can be subtracted off, though this procedure is argued to be dangerous (Dillon et al. 2014; Parsons et al. 2014).

Another type of noise bias can stem from the spurious cross-coupling of signals between antennas. This excess is known as instrumental crosstalk and is an inadvertent correlation between two independent measurements via a coupled signal path. Crosstalk varies on a time-scale much slower than the typical fringe-rates of sources. Because it is slow-varying, crosstalk can be suppressed using time-averages or fringe-rate filters. However, there remains a possibility that power spectrum detections that aren't the cosmological signal are caused by residual, low-level crosstalk which survived any suppression techniques.

2.5.2 Jackknife Tests

We now approach the difficult task of tracing excesses to foreground, noise, and EoR biases through a discussion of useful jackknife tests. Again, we first approach this topic pedagogically as an introduction to the related PAPER discussion in Chapter ??.

The jackknife is a resampling technique in which a statistic (i.e., power spectrum) is computed in subsets of the data (Quenouille 1949; Tukey 1958). These subsets are then compared to reveal systematics. In this section we define two main tests — the null test and the traditional jackknife — and explain how a power spectrum detection must pass each. We then highlight how these tests can be used to help distinguish between different sources of bias.

- **Null Test:** A null test is a type of jackknife test that removes the astronomical signal from data in order to investigate underlying systematics (see Keating et al. (2016) for examples from intensity mapping that are closely related to our current application). For example, one can divide data into two subsets by separating odd and even Julian dates, or the first half of the observing season from the second. Subtracting

the two removes signal that is common to both subsets, including foregrounds and the EoR signal. The resulting power spectrum should be consistent with thermal noise estimates; if it is not, it suggests the presence of a systematic that differs from one of the data subsets to the other (i.e., doesn't get subtracted perfectly).

- **Traditional Jackknife:** In a broader sense, it is important to perform many jackknife tests in order to instill confidence in a final result. A stable result must be steadfast throughout all jackknives no matter how the data is sliced. Jackknives can be taken along several different axes — for example, one could start with a full dataset, and compute a new power spectrum every time as a day of data is removed, or a baseline is removed. This type of jackknife would reveal bias present only at certain LSTs (such as a foreground source), for example, or misbehaving baselines.

While the null test hunts for deviations from thermal noise and the jackknife tests for deviations in subsamples, they are both closely related. We can highlight the connection between the two using a toy model dataset.

Suppose we have four independent measurements made along two different axes. As an example, we construct \mathbf{x}_{1a} , \mathbf{x}_{1b} , \mathbf{x}_{2a} , and \mathbf{x}_{2b} , where the numbers symbolize two different days of data and the letters represent two different baselines. Each of the measurements have dimensions of 100 time integrations and 20 frequency channels. They each have separate thermal noises constructed as a Gaussian random signal for each, and identical EoR signals.

To mimic the presence of a systematic, we add a toy sinusoid foreground, similar to the one used in Chapter 2.2.2, to only \mathbf{x}_{2a} and \mathbf{x}_{2b} . This represents a foreground signal present in only the second day of data, but not the first. Mathematically, if \mathbf{n} is noise, \mathbf{e} is the EoR signal, and \mathbf{f} is the foreground signal, the four measurements can be written as:

$$\mathbf{x}_{1a} = \mathbf{n}_{1a} + \mathbf{e} \quad (2.36)$$

$$\mathbf{x}_{1b} = \mathbf{n}_{1b} + \mathbf{e} \quad (2.37)$$

$$\mathbf{x}_{2a} = \mathbf{n}_{2a} + \mathbf{e} + \mathbf{f} \quad (2.38)$$

$$\mathbf{x}_{2b} = \mathbf{n}_{2b} + \mathbf{e} + \mathbf{f}. \quad (2.39)$$

We now take a jackknife along the day-axis, forming separate power spectrum estimates for each day:

$$\hat{\mathbf{P}}_1 \propto \mathbf{x}_{1a}\mathbf{x}_{1b}^\dagger \quad (2.40)$$

$$\hat{\mathbf{P}}_2 \propto \mathbf{x}_{2a}\mathbf{x}_{2b}^\dagger. \quad (2.41)$$

We do not perform a time-average or apply a fringe-rate filter to this toy model, since we are interested only in what jackknife tests can tell us about biases. For the same reason, we use a weighting matrix of \mathbf{I} for power spectrum estimation to avoid signal loss.

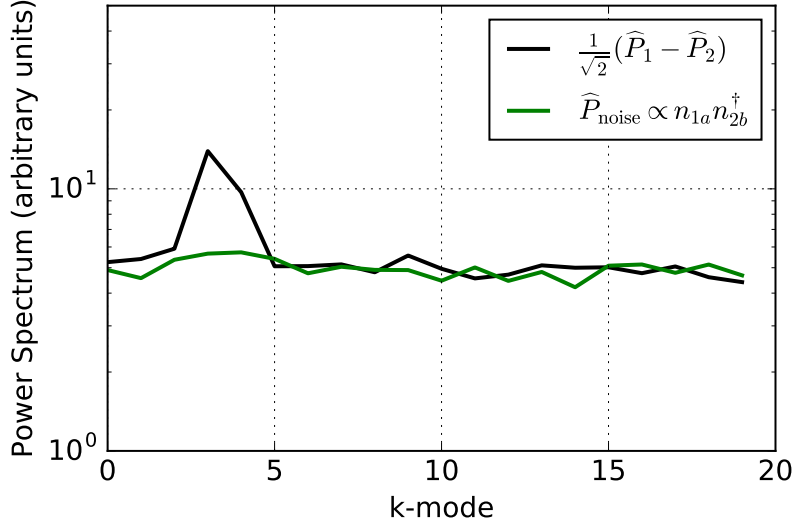


Figure 2.10: A null jackknife test shown as the power spectrum difference between two measurements (black), compared to the power spectrum of noise alone (green). Because the null test is not consistent with noise, it suggests the presence of a systematic in either \mathbf{x}_1 or \mathbf{x}_2 . Null tests of clean measurements should be consistent with thermal noise.

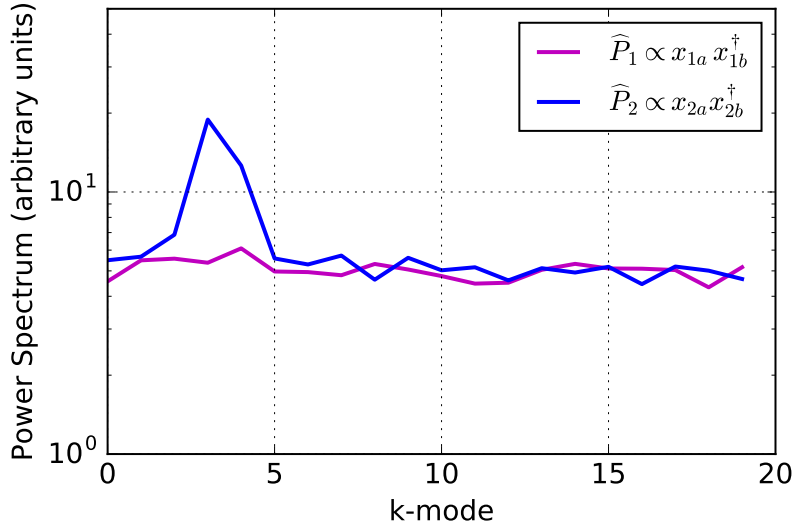


Figure 2.11: Power spectrum estimates for \mathbf{x}_1 and \mathbf{x}_2 , two jackknives of the toy model. They suggest the presence of a systematic in \mathbf{x}_2 only, illustrating how jackknives can be used to tease out excesses. Clean measurements should remain consistent despite the jackknife taken.

To construct a null test, we difference the two power spectra, with the result shown in Figure 2.10 (black) along with the power spectrum of noise only (green). Subtracting the two estimates removes sky signal that should ideally be present in both jackknives. However, we see a clear difference between the null test and the power spectrum of noise. This signifies a non-EoR bias that is only present in either \mathbf{x}_1 or \mathbf{x}_2 , but not both.

While the null test is useful for testing noise properties and the uniformity of a dataset, jackknives are useful in pinpointing which data subsets are contaminated by biases and which are not; in our toy model we see that the bias exists only in \mathbf{x}_2 (Figure 2.11). If foreground or noise biases exist in a dataset, jackknives can tease them out and provide insight into possible sources. For example, if jackknives along the time-axis reveal a bias present at a certain LST, a likely explanation would be excess foreground emission from a radio source in the sky at that time. A jackknife test involving data before and after the application of a fringe-rate filter can reveal whether crosstalk noise bias is successfully suppressed with the filter, or if similar-shaped detections in both power spectra suggest otherwise. There are many other jackknife axes of which we will not go into detail here, including baseline, frequency, and polarization. Ultimately, an EoR detection should persist through them all and a clean measurement should exhibit noise-like null spectra.

In this section we have highlighted how null tests and jackknife tests are key for determining the nature of a power spectrum detection. In Chapter ?? we perform some examples of these tests on PAPER-64 data in order to show that our excesses are not EoR and to identify their likely cause.

Chapter 3

PAPER-64 Case Study

3.1 Overview

In the previous chapter we have discussed three overarching 21 cm power spectrum themes — signal loss, error estimation, and bias. Understanding the subtleties and trade-offs involved in each is necessary for an accurate and robust understanding of a power spectrum result.

We now apply these lessons to data from the PAPER experiment in order to illustrate our revised analysis pipeline. We begin with a brief overview of PAPER’s data processing steps prior to power spectrum estimation before delving into each theme in detail.

3.1.1 Observations

As described in Chapter 1.3.1, PAPER is a dedicated 21 cm experiment located in the Karoo Desert in South Africa. The PAPER-64 configuration consists of 64 dual-polarization drift-scan elements that are arranged in a grid layout (Figure 3.1). While every unique baseline is used for calibration, only a subset of the baselines are used for the power spectrum analysis in A15 (the three baselines used are the 30 m East/West baselines and their off-diagonal companions where two antennas are in adjacent columns and neighboring rows) and only one baseline-type is used for the demonstrations in this chapter (only the 30 m East/West baselines).

PAPER-64 conducted nighttime observations from November 2012 to March 2013. Over the course of the season, LST-coverage varied slightly, with power spectrum analyses focusing on the “cold patch” range from $\sim 0\text{--}8$ hours when the Galaxy is below the horizon. The PAPER correlator processes a 100–200 MHz bandwidth that consists of 1024 channels, each of width 97.6 kHz. Visibilities are integrated for 10.7 s before being written to disk.

PAPER’s raw data is compressed by a factor of ~ 70 through the use of RFI, delay, and delay-rate filters. More specifically, radio frequency interference is flagged at the 6σ level. Next, a low-pass delay filter is applied to all the data in order to filter out delays greater than the maximum delay allowed by the longest baseline in the array. Similarly, a low-pass

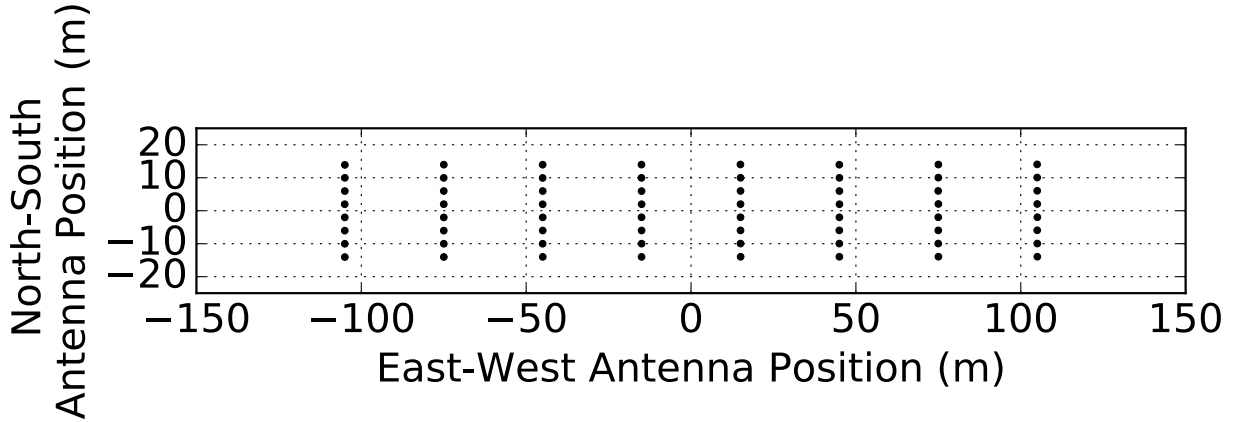


Figure 3.1: The PAPER-64 antenna layout. We use only 10 of the 30 m East/West baselines for the analysis in this chapter (i.e., a subset of the shortest horizontal spacings).

fringe-rate, or delay-rate filter is applied to limit fringe-rates to allowable scales set by the array. Finally, the data is decimated to critical Nyquist sampling rates of 493 kHz and 42.9 s. For more details about PAPER’s data acquisition and compression pipelines, we refer the reader to [Parsons et al. \(2010\)](#) and [A15](#).

3.1.2 Data Processing

As described in Chapters [1.2.3](#), [1.2.4](#), [1.2.5](#), the primary post-processing steps of PAPER’s compressed data is calibration, foreground-filtering, and fringe-rate filtering. We now give a brief overview of each, as applied to PAPER data.

We employ the package OMNICAL for redundant calibration ([Zheng et al. 2014](#)), which comprises of three steps. The first is `FirstCal`, which uses all baseline redundancies to generate a static gain solution for each antenna that will unwrap any phase wrapping between two identical baselines. We perform `FirstCal` because the next stage of OMNICAL cannot tell the difference between a phase of 0 and 2π , for example. The second step is `LogCal`, which takes the log of all the visibility equations (Equation [\(1.8\)](#)) and separates the real and imaginary components into two matrices. Coarse solutions are determined for both the antenna gains and “model” visibilities (one for each baseline type) simultaneously. The final step of OMNICAL is `LinCal`, which applies small perturbations to the `LogCal` solutions in an iterative fashion, honing in on the optimal solutions.

It is important to note that while OMNICAL is powerful for ensuring array redundancy, it is not able to solve for 4 calibration parameters - namely, the overall gain, phase, and tip/tilt of the array. For absolute calibration, we turn to a standard self-calibration routine which includes imaging Pictor A, Fornax A, and the Crab Nebula in order to fit for the overall phase solutions and the flux scale.

After calibration, we combine the XX and YY linear polarization data to form pseudo-Stokes I as defined as:

$$V_I = \frac{1}{2}(V_{XX} + V_{YY}) \quad (3.1)$$

(Moore et al. 2013).

Next, a delay-filter is used to filter out foregrounds contained inside the maximum delay set by each baseline. This is accomplished by de-convolving out our sampling function (which contains flags due to RFI) from our delay-domain visibilities using a CLEAN-like algorithm that restricts our clean components to inside the horizon limit, plus a 15 ns buffer. The Fourier-transformed clean components are then subtracted from our visibilities. This filtering process is performed on a per-baseline, per-integration basis, and we achieve a brightness suppression of ~ 4 orders of magnitude in our visibilities.

After delay-filtering, we perform a final round of RFI-removal by flagging visibilities that lie more than 3σ above the mean on a time, frequency, and baseline basis. Finally, we stack our data in LST into two datasets, alternating between even and odd Julian Dates to create an “even” and “odd” LST-binned dataset. A total of 124 days of data are included in the LST-binned dataset.

The final step before power spectrum estimation is fringe-rate filtering. The chosen filter (which is described in the next section) is applied on a per-baseline basis and weights the fringe-rate bins on the sky by the RMS of the primary beam at that same location. A smooth filter is constructed by fitting a Gaussian to the filter shape in the fringe-rate domain. Additionally, fringe-rates below 0.2 mHz are zeroed out, effectively removing slowly-varying signals such as crosstalk. We then convolve our time-domain visibilities by the Fourier-transform of the fringe-rate filter to yield time-averaged visibilities that have gained another order of magnitude in sensitivity.

3.1.3 Case Study Data

For the case study presented in the rest of this chapter, we focus on a subset of the PAPER-64 data used in A15, namely, on LST-binned, Stokes I estimated data (Moore et al. 2013) from PAPER’s 30 m East/West baselines (Figure 3.1). Hence, all data processing steps are identical to those in A15 until after the LST-binning step in Figure 3 of A15.

The previously best published 21 cm upper limit result from A15 placed a 2σ upper limit on $\Delta^2(k)$, defined as

$$\Delta^2(k) = \frac{k^3}{2\pi^2} \hat{P}(k), \quad (3.2)$$

of $(22.4 \text{ mK})^2$ in the range $0.15 < k < 0.5 h \text{ Mpc}^{-1}$ at $z = 8.4$. The need to revise this limit stems mostly from previously under-estimated signal loss and under-estimated error bars, both of which we address in the following sections.

For the analysis in this chapter, we use 8.1 hours of LST, namely an RA range of 0.5-8.6 hours ([A15](#) uses a slightly longer RA range of 0-8.6 hours; we found that some early LSTs were more severely foreground contaminated). We also use only 10 baselines, a subset of the 51 total East/West baselines used in [A15](#), in order to illustrate our revised methods. All power spectrum results are produced for a center frequency of 151 MHz using a width of 10 MHz (20 channels), identical to the analysis in [A15](#). In the case study in this chapter, we only use one baseline type instead of the three as in [A15](#), but Kolopanis et al. (*in prep.*) uses the full dataset presented in [A15](#) to revise the result and place limits on the EoR at multiple redshifts (using a straightforward and not lossy approach to avoid many of the issues presented in this chapter).

The most significant changes from [A15](#) occur in our revised power spectrum analysis, which is explained in the rest of this chapter, but we also note that the applied fringe-rate filter is also slightly different. In [A15](#), the applied filter was not equivalent to the optimal fringe-rate filter (which is designed to maximize power spectrum sensitivity). Instead, the optimal filter was degraded slightly by widening it in fringe-rate space. This was chosen in order to increase the number of independent modes and reduce signal loss associated with the quadratic estimator, though as we will explain in the next section, this signal loss was still under-estimated. With the development of a new, robust method for assessing signal loss, we choose to use the optimal filter in order to maximize sensitivity. This filter is computed for a fiducial 30 m baseline at 150 MHz, the center frequency in our band. The filter in both the fringe-rate domain and time domain is shown in Figure 3.2.

Finally, we emphasize that the discussion that follows is solely focused on signal loss associated with empirical covariance weighting. As mentioned in Chapter 2.2, there are several other ways the PAPER analysis pipeline can lead to loss, including through calibration and delay-filtering. We refer the reader to [Parsons et al. \(2010\)](#) and [A15](#) for discussions about these other types of signal loss, noting here that they are much less significant than the loss focused on in this chapter.

3.2 Signal Loss

3.3 Error Estimation

3.4 Bias

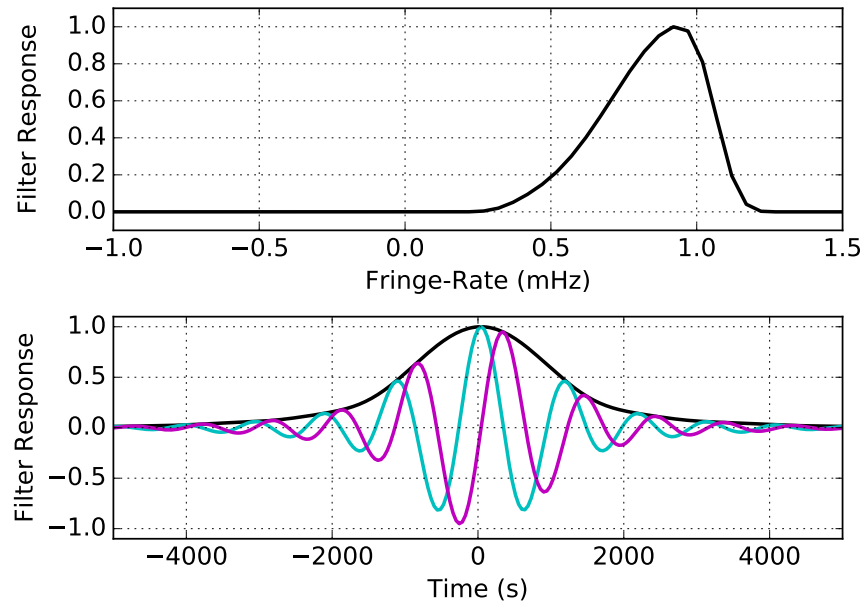


Figure 3.2: Top: the normalized optimal power-spectrum sensitivity weighting in fringe-rate space for our fiducial baseline and Stokes I polarization beam. Bottom: the time domain convolution kernel corresponding to the top panel. Real and imaginary components are illustrated in cyan and magenta, respectively, with the absolute amplitude in black. The fringe-rate filter acts as an integration in time, increasing sensitivity but reducing the number of independent samples in the dataset.

Chapter 4

PAPER-64 Results

Chapter 5

PAPER-128

5.1 Overview

The PAPER experiment expanded out to 128 antennas in 2013 and observed for two seasons. The first season began in November, 2013 and lasted until March, 2014. The second began in July, 2014 and ended in January, 2015. The PAPER-128 configuration consists of 112 core antennas arranged in a grid layout (7 rows and 16 columns), with neighboring East/West spacings being 15 m and neighboring North/South spacings being 4 m (Figure 5.1). Additionally, 16 outrigger antennas were placed in strategic locations in order to form long baselines and increase *uv*-plane sampling. These outrigger antennas are not used for the power spectrum analysis presented in this thesis, but are useful for imaging analyses.

In general, the signal chain of PAPER-128 is similar to that of PAPER-64. However, one major change is the addition of receiverators on site, which houses the receivers used to amplify and filter the antenna signals. Prior to this change, the receivers were located inside a cooled shipping container along with the rest of the DSP system. With the addition of more antennas, however, the receivers were moved outside the container to save space.

Although PAPER-128 doubled in number of antennas, the data collected by this array is typically found to be lower in quality than that of PAPER-64. There are many reasons for this, including general wear and tear on the instrument and the addition of the receiverators (which had no monitoring system and, as we will see, is one of the main reasons for missing and corrupted PAPER-128 data). Because of these issues, PAPER-128 requires the development of novel techniques in order to filter out contaminated data products prior to analysis. Using the entire season of data, without any filtering, would result in a power spectrum analysis severely dominated by systematics and (non-EoR) detections. Thus, one of the unique challenges facing PAPER-128 is how to automatically and accurately detect and remove bad data (i.e., misbehaving baselines, dead receiverators, criss-crossed signal paths, etc.) in order to curate a dataset as free of systematics as possible.

In this chapter, we present methods developed for the detection of corrupt data in PAPER-128. These methods represent the first routinely-used “quality assurance” steps for the PAPER experiment. They also represent the first generation of data assessment

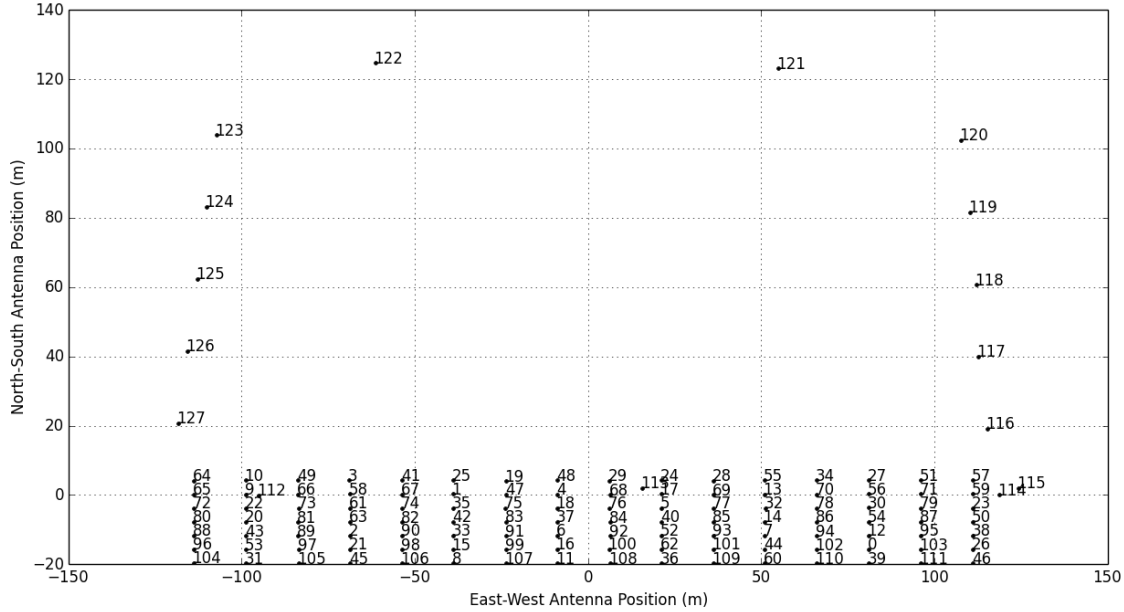


Figure 5.1: The PAPER-128 antenna layout. There are 112 antennas arranged in a grid layout which are used for power spectrum analyses. The addition of 16 outrigger antennas is used to increase *uv*-plane sampling for imaging analyses.

techniques that are currently being expanded upon for incorporation into HERA’s real-time processing system.

Additionally in this chapter, we process two epochs of PAPER-128 data (both from the first season) and show power spectrum results for each. We do not show results from the second season of data due to increased hardware failure that was experienced at the end of PAPER-128’s deployment. As such, the first season of PAPER-128 represents the bulk of the array’s sensitivity (though we note that the limits do not surpass those of PAPER-64, mostly due to having fewer days of data). Table 5.1 gives an overview of the PAPER-128 dataset analyzed in this thesis.

5.2 Quality Assurance

Post-processing of PAPER data relies heavily on the array’s redundancy, and any sources of non-redundancy have the potential to corrupt redundant calibration and power spectrum estimation. These sources of error — which span from the failure of analog or digital components to improper feed installation to the accidental deletion and subsequent recovery of data products — manifest themselves in corrupted data that can be found primarily along two main axes: the time-axis and the antenna-axis.

We next present metrics that we have developed to locate contaminated data along

Epoch	Dates	Number of Days Analyzed	Flagged Days	Flagged Antennas
1	Nov 2013 - Jan 2014 JDs 6617-6673	38	6647,6662,6664, 6665,6673	3,7,8,16,19,20, 27,28,34,53, 56,84,85,96,100 FX2: 2,10,15,22,31, 33,42,43,47,58, 64,72,91,97,105,107
2	Jan 2014 - March 2014 JDs 6678-6724	40	6692,6702,6704, 6706,6717,6730	3,7,16,27,34,56, 57,84,85,100,110

Table 5.1: An overview of the PAPER-128 data used for power spectrum analysis in this thesis.

these axes. We use the results of these metrics to remove specific days of data and specific antennas from our analysis prior to calibration in order to ensure robust calibration that is not influenced by outlier data.

5.2.1 Flagging Julian Dates

To better assess the variation of PAPER-128 data across its two-year deployment (which consists of 7+ individual epochs of data, where an epoch is characterized by the shut-down and subsequent re-starting of the correlator), we first investigate one-dimensional slices of compressed data that span the entire time axis but only one frequency channel. We choose channel 100 for this analysis, as its corresponding frequency of 150 MHz lies in the middle of our band (similar to PAPER-64, PAPER-128’s bandwidth consists of 203 frequency channels ranging from 100 to 200 MHz).

We look at the visibility amplitude of each day of data in an epoch as a function of LST, shown as the different colors in Figure 5.2. We designate a reference day to each epoch (a manually chosen “good” day), and flag days that differ from the reference day by more than 20%. After flagging, visibilities show good day-to-day agreement across an epoch (bottom row of Figure 5.2).

An example of data from a particularly “bad” day is shown in Figure 5.3. It is clear that Julian date 2456692 differs dramatically from reference day 2456680, as it contains many corrupted files throughout the day due to failure somewhere in the signal chain. This failure mode is often due to the accidental deletion and erroneous recovery of data (much of the season’s data was accidentally deleted prior to any of the work in this thesis), as well as hardware failures (e.g., loose cable connections) that result in lost sky fringes. From Table 5.1, we see that a total of 38 days pass our flagging metric for Epoch 1 and 40 days pass for Epoch 2 (both from PAPER-128’s first observing season), and a total of five and six days are flagged for each epoch, respectively.

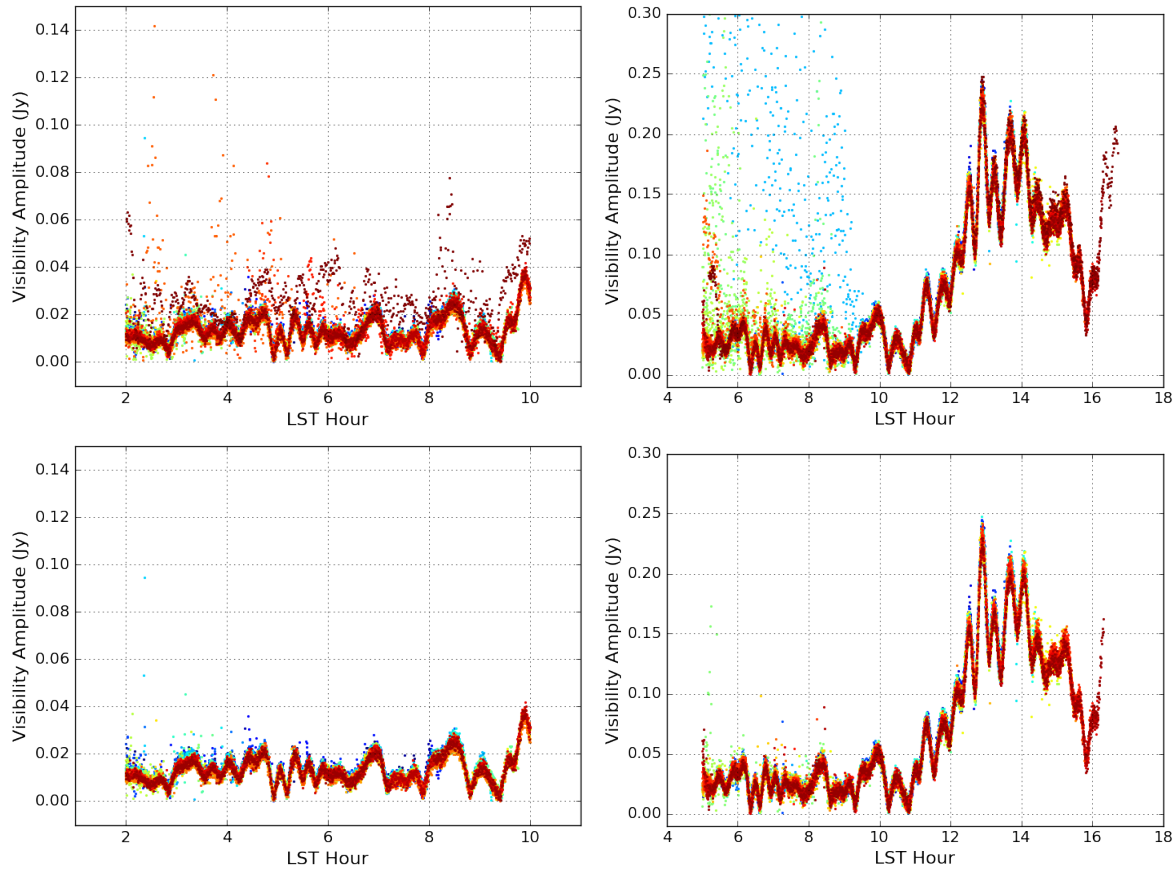


Figure 5.2: Visibility amplitudes as a function of LST for different Julian days of data (colors). The left column shows the data before (top) and after (bottom) the flagging of outlier days for Epoch 1. The right column shows similar data for Epoch 2. After flagging, visibilities show good day-to-day agreement across an epoch.

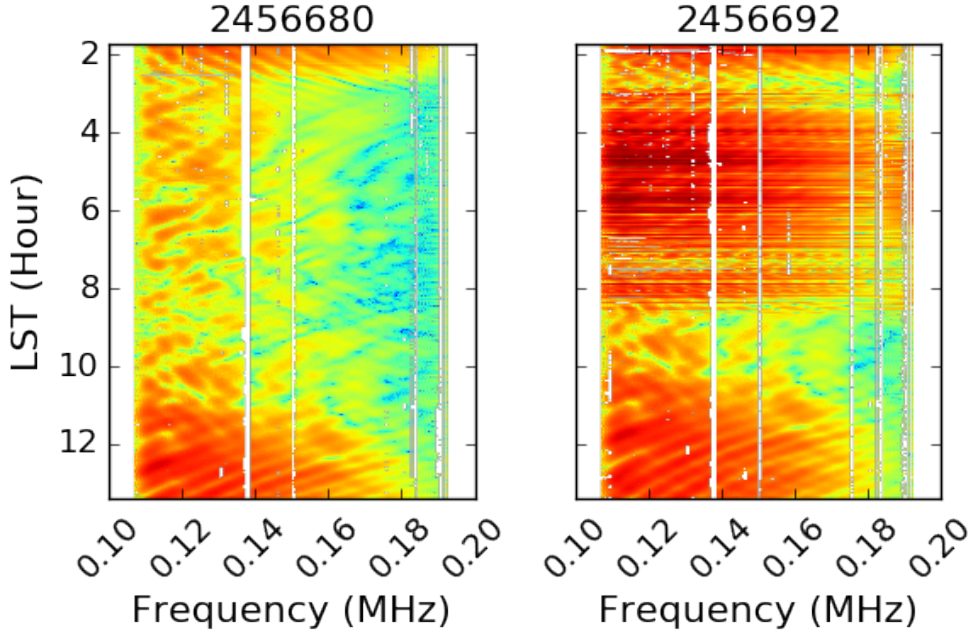


Figure 5.3: Waterfall plots of visibility amplitudes for a “good” reference day (left) in Epoch 2 and “bad” day (right). We exclude corrupted data for specific days found with our metric.

5.2.2 Flagging Antennas

There are a few types of failure modes for data associated with specific antennae. The first is if feeds are accidentally rotated by 90 degrees (or equivalently, the cables for the XX and YY polarizations are swapped). Consequently, visibilities involving a “cross-polarized” antenna exhibit visibility amplitudes that are more weakly correlated (lower amplitude) than what is expected for an XX or YY visibility (and similarly, XY and YX visibilities exhibit too high of an amplitude, or too strong of a correlation). In order to locate potentially cross-polarized antennae, we use the following metric:

$$M_i = \frac{\sum_{j,\nu,t} |V_{ij}|}{(N - 1)}, \quad (5.1)$$

where the visibility for baseline ij is summed for every j^{th} antenna, frequency ν , and time t , and N is the number of antennas. We compute this metric for all four polarizations (XX, XY, YX, YY). Next, for each night of data we form the polarization fraction quantity:

$$P_i = \frac{M_i^{XY} + M_i^{YX}}{M_i^{XX} + M_i^{YY}}. \quad (5.2)$$

We expect the numerator of this quantity to be higher than the denominator for cross-polarized antennae. In practice, we form polarization fractions for every antenna and flag

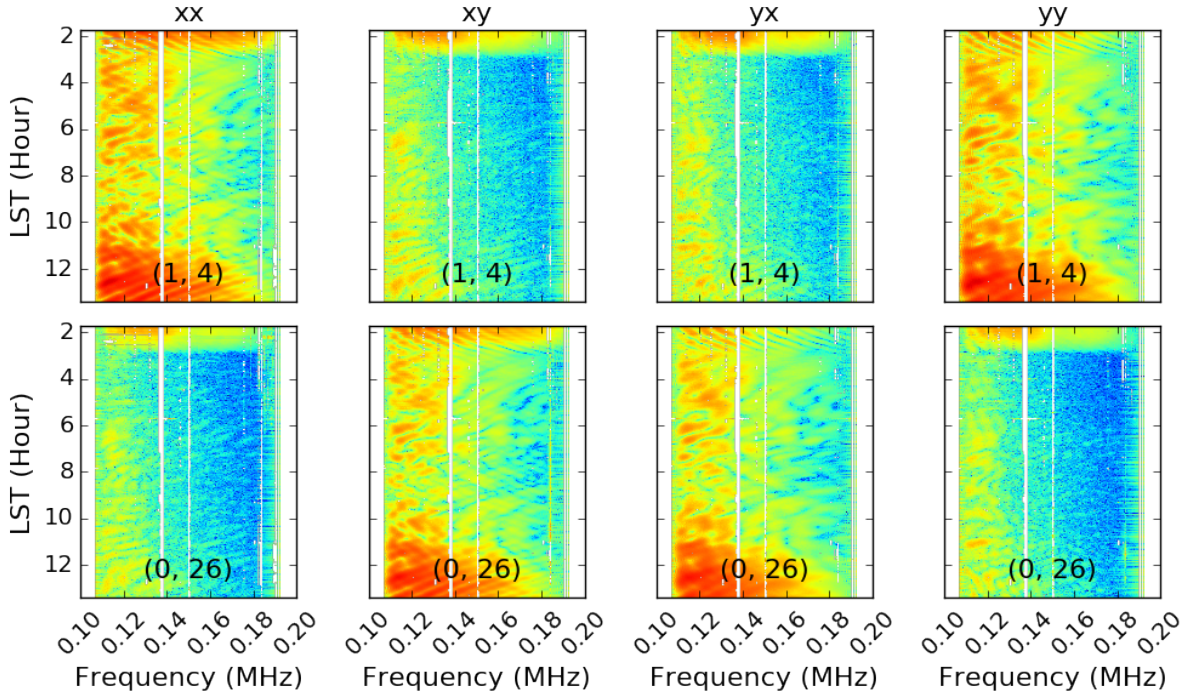


Figure 5.4: Waterfall plots of visibility amplitudes for four different polarizations and two different baselines. Antenna 26 is found to be cross-polarized because its feed was rotated by 90 degrees, and hence its “X” and “Y” polarization states are mis-labeled. Equation (5.2) captures visibility amplitudes like the ones shown here in order to automatically detect cross-polarized antennae.

those with high P_i values as being cross-polarized. We note that this metric works best for long baselines, where XX and XY visibilities are expected to have large differences in signal-to-noise over short distance scales. For short baselines (and large-scales), astrophysical polarization has been shown to be present in all polarization quantities, including the linear ones, thus bringing P_i closer to unity (Lenc et al. 2016).

Using this metric, we find six antennas to be cross-polarized in PAPER-128 observations (antennas 26, 34, 38, 46, 50, and 72). An example of visibilities containing antenna 26 is shown in Figure 5.4, and it is clear that the “X” and “Y” polarizations are swapped for baselines involving that antenna. We fix this issue, re-naming polarization states where necessary, for all the compressed PAPER-128 data before performing other quality assessment tests and calibration.

Another failure mode is an antenna that exhibits low amplitude, a fairly common occurrence as different electronic components can cause the temporary reduction or loss of power. A drastic example of this is when an entire correlator (FX2) was accidentally shut-off, cutting off connections to 16 antennas. The loss of those 16 antennas only affected Epoch 1, and the correlator was then re-started for Epoch 2.

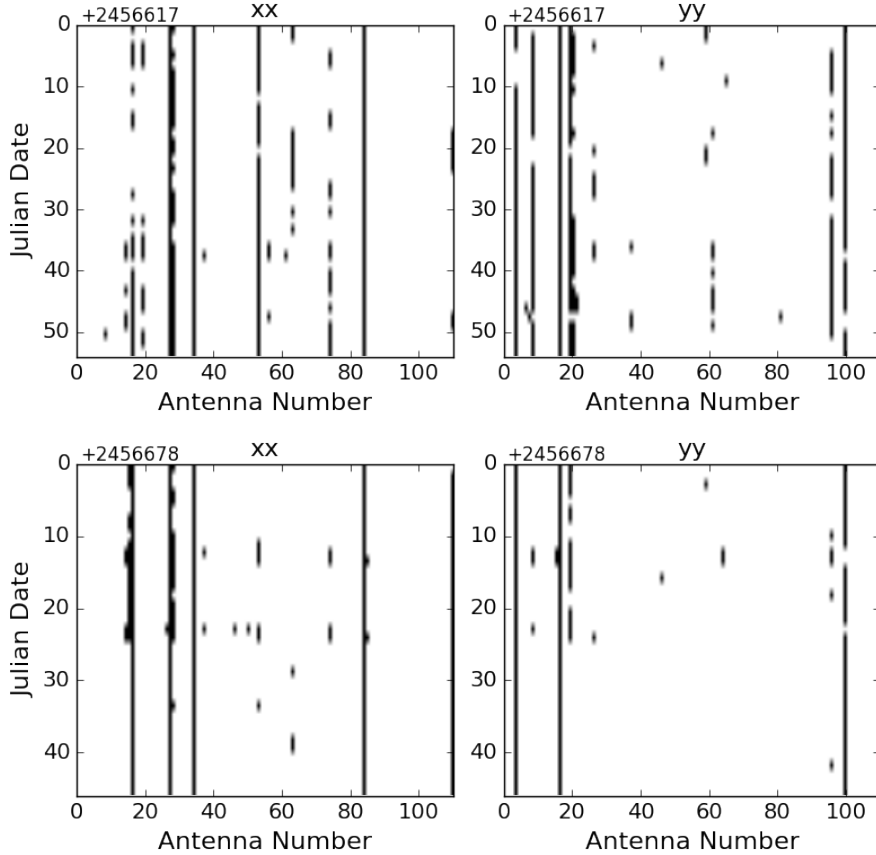


Figure 5.5: Flagged antennas, found using Equation (5.1), are marked in black for each antenna number (x-axis) and Julian date (y-axis). The left column shows flags for XX polarization, and the right column shows flags for YY polarization. The top row shows flags for Epoch 1 and the bottom row shows flags for Epoch 2. We remove antennas that are flagged greater than 50% of the time per epoch.

In order to find antennas with unusually low signals, we again employ Equation (5.1), computing the metric for every antenna. Comparing M_i across the entire array can reveal which antennas are consistently misbehaving. We then flag antennas with M_i values that are low by at least 1σ . Figure 5.5 shows these antenna flags across both epochs, and we remove all data associated with antennas that are flagged greater than 50% of the time (then for each epoch, we combine the flags for the XX and YY polarizations).

Almost all of the flagged antennas listed in Table 5.1 are found via the metric described above. However, we do note that a handful are found manually by visually inspecting visibility data and `Omnical` results. While our metric does a good job identifying antennas with low amplitudes, we found that there were certain antennas (usually one-off instances) with additional issues that do not fall under any of our previous metrics and would require a more sophisticated metric to be able to find automatically.

Finally, we highlight the importance of flagging antennas prior to redundant calibration by showing `FirstCal` phase solutions for a single antenna without flagging and with flagging (Figure 5.6, top). `Omnical` χ^2 results are also shown (bottom). These results depict how the quality of redundant calibration (the stability of the calibration solutions and level of redundancy) depends on the behavior of the antennas. It is evident that the `FirstCal` solutions are unstable from file to file without any initial antenna flagging (top left). Similarly, higher χ^2 values means that the `Omnical` model visibilities differ substantially from the gain-corrected measured visibilities, meaning redundant calibration is poor. It is obvious that pre-calibration flagging metrics are crucial in order to robustly calibrate PAPER-128 data.

5.3 Data Processing

We process both epochs of PAPER-128 data, closely following the PAPER-64 processing steps outlined in Chapter 3.1.2. One specific difference from the PAPER-64 pipeline is that we aggressively flag RFI prior to delay-filtering in order to prevent low levels of spectral structure from leaking into the EoR window. Because the overall quality of PAPER-128 data is in general lower than PAPER-64, we found that aggressive flagging methods are worthwhile in order to maximize signal-to-noise. To accomplish this, we first flag calibrated visibilities on a per-frequency, per-integration basis based on OMNICAL χ^2 values (using a 6σ deviation cutoff). This masks potentially problematic data identified from the redundant calibration solutions. In addition, we manually flag ten known channels containing RFI.

Delay-filtering proceeds identically to the PAPER-64 pipeline. We then bin both the foreground-containing and foreground-removed data by LST into separate datasets. For both these datasets, we form Stokes I using Equation (3.1).

Recalling that redundant calibration only solves for internal calibration parameters, absolute calibration remains needed. In the PAPER-64 analysis, a self-calibration method was used to solve for overall gain and phase calibration solutions (immediately after redundant calibration) (Ali et al. 2015). Trusting these solutions, we can then calibrate the PAPER-128 data to the calibrated PAPER-64 data. To do this, we use foreground-containing, LST-binned data for both PAPER-64 and PAPER-128 (where the PAPER-64 dataset is already calibrated) and look at a matching fiducial baseline for each. We align both datasets in LST and compute the ratio of the two for every time integration and frequency channel. We then average these ratios over time to yield a bandpass solution.

Mathematically, if the visibility data for PAPER-64 and PAPER-128 are written as the following complex numbers:

$$V_{64} = ae^{i\phi_a} \quad (5.3)$$

$$V_{128} = be^{i\phi_b}, \quad (5.4)$$

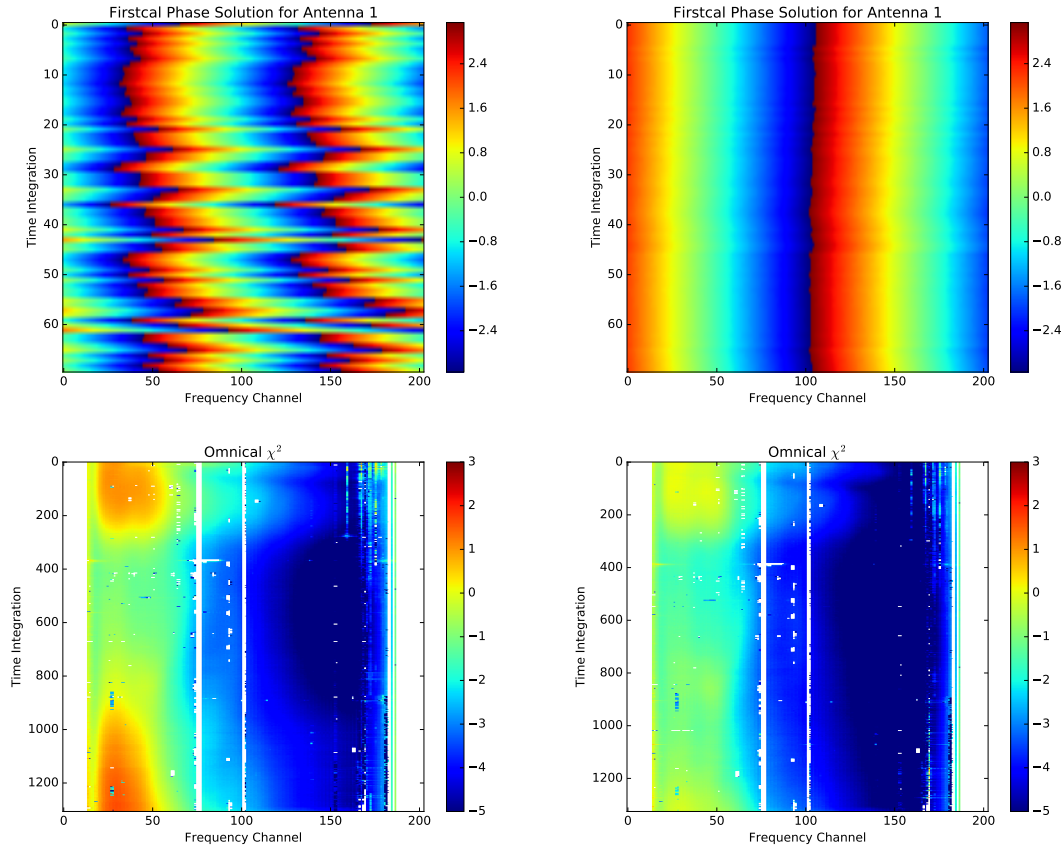


Figure 5.6: FirstCal phase solutions for Antenna 1 (Epoch 1, XX polarization) where no antennas are flagged (top left) and some antennas are flagged (via the methods described in Chapter 5.2.2, top right). Omnical χ^2 results are also shown for the two cases (bottom). We do not include any of the 16 dead antennas associated with correlator FX2. It is crucial to flag misbehaving antennas (especially extreme outlier antennas) prior to redundant calibration, motivating the development of automated quality assessment tools prior to the post-processing of data.

we solve for an overall gain correction factor as:

$$f_{gain} = \frac{a}{b} \quad (5.5)$$

and an overall phase factor as:

$$f_\phi = \phi_a - \phi_b. \quad (5.6)$$

Combining these two gives a bandpass solution (one number per frequency):

$$f = f_{gain} e^{if_\phi}. \quad (5.7)$$

Using this bandpass, we fit an eighth order polynomial to smooth the solutions and apply this multiplicative factor to the delay-filtered, LST-binned PAPER-64 data. We calibrate each epoch of data separately. We note that this coarse absolute calibration is only a rough calibration, and a more careful, sky-based calibration is recommended for precise results. However, using this simple calibration yields foreground data that agrees with the PAPER-64 data to within $\sim 20\%$.

Finally, the last step of processing is fringe-rate filtering, where an optimal filter is used to combine the data and filter out excess noise. PAPER-128 has an original integration time of 32 s, making the optimal filter length to be ~ 3910 s, slightly longer than that of PAPER-64. Armed with fringe-rate filtered, LST-binned datasets for both epochs, we proceed to power spectrum estimation.

5.4 Power Spectrum Limits

We form power spectrum estimates for both epochs of data and two frequency channel ranges: 139-149 MHz ($z=8.9$) and 154-164 MHz ($z=7.9$). Both bands consist of 21 channels (each 0.5 MHz) and are relatively absent of RFI. We focus only on one baseline-separation type, namely all 30 m East/West baselines (of which there are 51 in the first epoch and 79 in the second). Our power spectrum formalism follows the analysis outlined in Chapter 3 and uses all updated methods regarding bootstrapping and noise sensitivity estimation. Because empirical inverse covariance weighting is shown to be extremely lossy for fringe-rate filtered PAPER data (Chapter ??) and regularization techniques do not significantly improve power spectrum sensitivity (Chapter ??), we form unweighted limits ($\mathbf{C} \equiv \mathbf{I}$) in an effort to present straightforward, reliable results.

Figure 5.7 shows the power spectrum results for PAPER-128. The two epochs are displayed as columns and the two redshifts as rows. Black and gray data points represent positive and negative power spectrum values, respectively (calculated as the average power spectrum value over all baseline pairs), and they have 2σ error bars that are calculated from bootstrapping over baselines. The solid green curve is our theoretical prediction of our sensitivity, computed analytically using Equation (??). This sensitivity prediction is also plotted as gray shaded regions around the data points.

We note that our best limit is $(126.4 \text{ mK})^2$ at $k = 0.29 h \text{ Mpc}^{-1}$ and $z = 7.9$ (from Epoch 2). This is a factor of XXX higher than our best limit from PAPER-64 (which uses three baselines instead of just one). These limits are understandably comparable given that the PAPER-128 analysis uses fewer days of data (by a factor of ~ 2). While it's certainly possible that combining multiple epochs of data together (and using more baseline types) may yield better limits, we do not think this analysis is worthwhile as the second season of data is severely dominated by systematics. Instead, we look forward to exciting future results from HERA, knowing that many of the techniques developed for both PAPER-64 and PAPER-128 are being incorporated and improved upon.

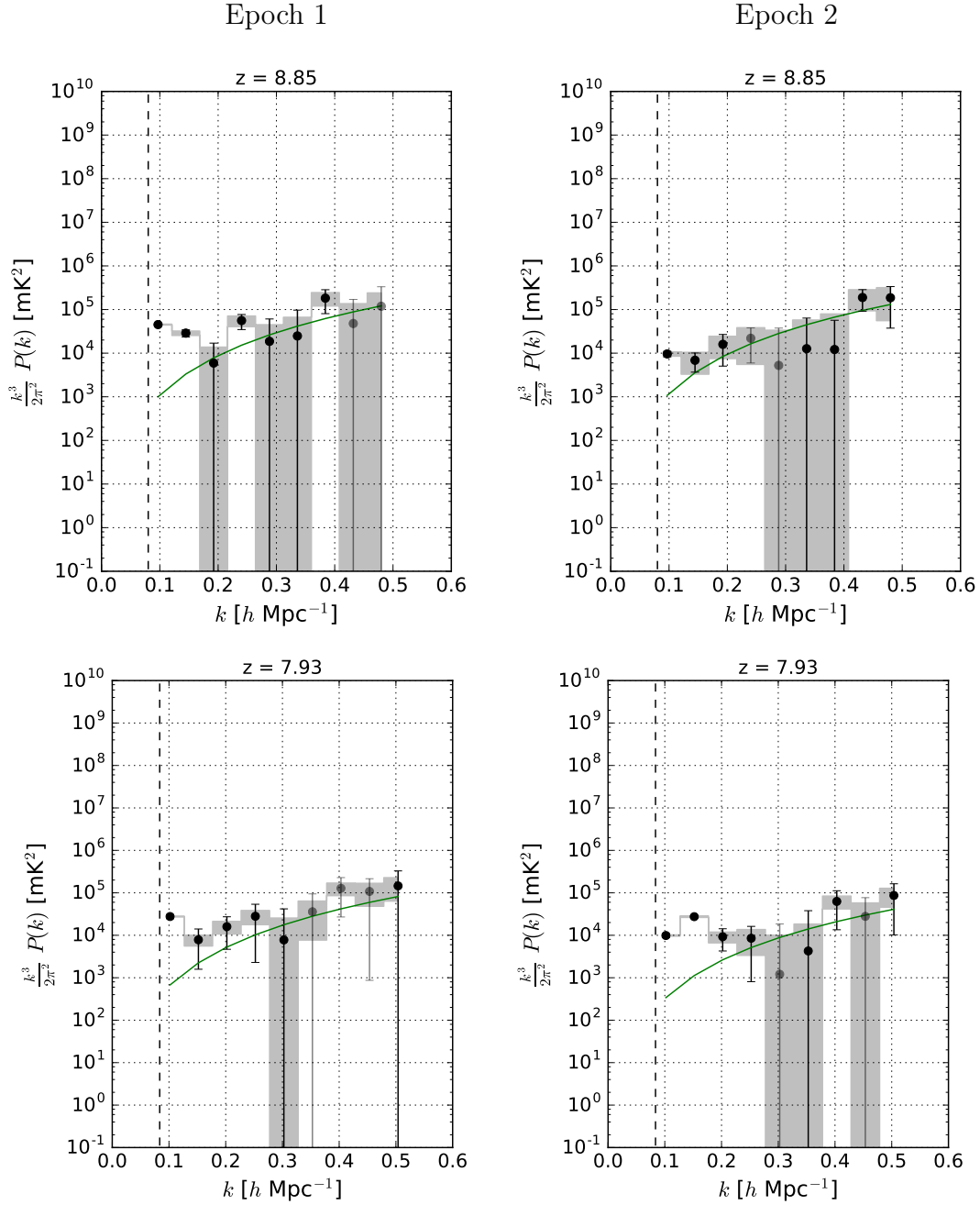


Figure 5.7: Power spectrum results for PAPER-128 season 1 data for two redshifts (rows) and two epochs (columns), using one baseline separation-type only (30 m East/West baselines). Black and gray points represent positive and negative power spectrum values, respectively, with 2σ error bars determined from bootstrapping. The 2σ theoretical noise sensitivity prediction is shown in green. Gray shaded regions correspond to theoretical errors on each data point.

Chapter 6

HERA

Chapter 7

Conclusion

Bibliography

- Ade, P., Bock, J., Bowden, M., et al. 2008, *Astrophysical Journal*, 674, 22
- Ade, P. A. R., Ahmed, Z., Aikin, R. W., et al. 2017, *Phys. Rev. D*, 96, 102003
- Ali, S. S., Bharadwaj, S., & Chengalur, J. N. 2008, *MNRAS*, 385, 2166
- Ali, Z. S., Parsons, A. R., Zheng, H., et al. 2015, *ApJ*, 809, 61
- Andrae, R. 2010, ArXiv e-prints, [arXiv:1009.2755 \[astro-ph.IM\]](https://arxiv.org/abs/1009.2755)
- Araujo, D., Bischoff, C., Brizius, A., et al. 2012, *The Astrophysical Journal*, 760, 145
- Barkana, R. 2009, *Monthly Notices of the Royal Astronomical Society*, 397, 1454
- . 2018, *Nature*, 555, 71
- Barkana, R., & Loeb, A. 2008, *Monthly Notices of the Royal Astronomical Society*, 384, 1069
- Beardsley, A. P., Hazelton, B. J., Sullivan, I. S., et al. 2016, *The Astrophysical Journal*, 833, 102
- Becker, R. H., Fan, X., White, R. L., et al. 2001, *AJ*, 122, 2850
- Bernardi, G., de Bruyn, A. G., Brentjens, M. A., et al. 2009, *A&A*, 500, 965
- Bernardi, G., de Bruyn, A. G., Harker, G., et al. 2010, *A&A*, 522, A67
- Bernardi, G., Greenhill, L. J., Mitchell, D. A., et al. 2013, *The Astrophysical Journal*, 771, 105
- Bernardi, G., Zwart, J. T. L., Price, D., et al. 2016, *MNRAS*, 461, 2847
- BICEP2 Collaboration, Keck Array Collaboration, Ade, P. A. R., et al. 2016, *ApJ*, 833, 228
- Bischoff, C., Brizius, A., Buder, I., et al. 2011, *The Astrophysical Journal*, 741, 111
- Bond, J. R., Jaffe, A. H., & Knox, L. 1998, *Phys. Rev. D*, 57, 2117
- Bowman, J. D., Morales, M. F., & Hewitt, J. N. 2009, *The Astrophysical Journal*, 695, 183
- Bowman, J. D., & Rogers, A. E. E. 2010, *Nature*, 468, 796
- Bowman, J. D., Rogers, A. E. E., Monsalve, R. A., Mozdzen, T. J., & Mahesh, N. 2018, *Nature*, 555, 67
- Burns, J. O., Lazio, J., Bale, S., et al. 2012, *Advances in Space Research*, 49, 433
- Chang, T.-C., Pen, U.-L., Bandura, K., & Peterson, J. B. 2010, *Nature*, 466, 463
- Chapman, E., Zaroubi, S., Abdalla, F. B., et al. 2016, *Monthly Notices of the Royal Astronomical Society*, 458, 2928
- Chapman, E., Abdalla, F. B., Harker, G., et al. 2012, *Monthly Notices of the Royal Astronomical Society*, 423, 2518
- Chiang, H. C., Ade, P. A. R., Barkats, D., et al. 2010, *The Astrophysical Journal*, 711, 1123
- Crites, A. T., Henning, J. W., Ade, P. A. R., et al. 2015, *The Astrophysical Journal*, 805, 36

- Das, S., Sherwin, B. D., Aguirre, P., et al. 2011a, *Physical Review Letters*, **107**, 021301
- Das, S., Marriage, T. A., Ade, P. A. R., et al. 2011b, *ApJ*, **729**, 62
- Datta, A., Bowman, J. D., & Carilli, C. L. 2010, *The Astrophysical Journal*, **724**, 526
- Datta, K. K., Jensen, H., Majumdar, S., et al. 2014, *MNRAS*, **442**, 1491
- de Oliveira-Costa, A., Tegmark, M., Gaensler, B. M., et al. 2008, *MNRAS*, **388**, 247
- DeBoer, D. R., Parsons, A. R., Aguirre, J. E., et al. 2017, *Publications of the Astronomical Society of the Pacific*, **129**, 045001
- Dillon, J. S., Liu, A., & Tegmark, M. 2013, *Phys. Rev. D*, **87**, 043005
- Dillon, J. S., & Parsons, A. R. 2016, *The Astrophysical Journal*, **826**, 181
- Dillon, J. S., Liu, A., Williams, C. L., et al. 2014, *Phys. Rev. D*, **89**, 023002
- Dillon, J. S., Neben, A. R., Hewitt, J. N., et al. 2015a, *Phys. Rev. D*, **91**, 123011
- Dillon, J. S., Tegmark, M., Liu, A., et al. 2015b, *Phys. Rev. D*, **91**, 023002
- Dodelson, S. 2003, Modern cosmology (San Diego, CA: Academic Press)
- Dodelson, S., & Schneider, M. D. 2013, *Phys. Rev. D*, **88**, 063537
- Efron, B., & Tibshirani, R. 1994, An Introduction to the Bootstrap, Chapman & Hall/CRC Monographs on Statistics & Applied Probability (Taylor & Francis)
- Ewall-Wice, A., Dillon, J. S., Liu, A., & Hewitt, J. 2017, *MNRAS*, **470**, 1849
- Fialkov, A., Barkana, R., Pinhas, A., & Visbal, E. 2014, *Monthly Notices of the Royal Astronomical Society: Letters*, **437**, L36
- Fialkov, A., Barkana, R., & Visbal, E. 2014, *Nature*, **506**, 197
- Furlanetto, S. R., Oh, S. P., & Briggs, F. H. 2006, *Phys. Rep.*, **433**, 181
- Ghosh, A., Bharadwaj, S., Ali, S. S., & Chengalur, J. N. 2011, *MNRAS*, **418**, 2584
- Haiman, Z., & Knox, L. 1999, in Astronomical Society of the Pacific Conference Series, Vol. 181, Microwave Foregrounds, ed. A. de Oliveira-Costa & M. Tegmark, 227
- Harker, G., Zaroubi, S., Bernardi, G., et al. 2009, *Monthly Notices of the Royal Astronomical Society*, **397**, 1138
- Hartlap, J., Simon, P., & Schneider, P. 2007, *A&A*, **464**, 399
- Hazelton, B. J., Morales, M. F., & Sullivan, I. S. 2013, *The Astrophysical Journal*, **770**, 156
- Hinshaw, G., Larson, D., Komatsu, E., et al. 2013, *ApJS*, **208**, 19
- Jacobs, D. C., Poher, J. C., Parsons, A. R., et al. 2015, *ApJ*, **801**, 51
- Jacobs, D. C., Hazelton, B. J., Trott, C. M., et al. 2016a, *ApJ*, **825**, 114
- . 2016b, *ApJ*, **825**, 114
- Jelić, V., Zaroubi, S., Labropoulos, P., et al. 2008, *MNRAS*, **389**, 1319
- Joachimi, B. 2017, *MNRAS*, **466**, L83
- Keating, G. K., Marrone, D. P., Bower, G. C., et al. 2016, *The Astrophysical Journal*, **830**, 34
- Kerrigan, J., Poher, J., Ali, Z., et al. 2018, ArXiv e-prints, [arXiv:1801.00460 \[astro-ph.IM\]](https://arxiv.org/abs/1801.00460)
- Kohn, S. A., Aguirre, J. E., Nunhokee, C. D., et al. 2016, *ApJ*, **823**, 88
- Koopmans, L., Pritchard, J., Meléma, G., et al. 2015, Advancing Astrophysics with the Square Kilometre Array (AASKA14), 1
- Lenc, E., Gaensler, B. M., Sun, X. H., et al. 2016, *The Astrophysical Journal*, **830**, 38
- Liu, A., Parsons, A. R., & Trott, C. M. 2014a, *Phys. Rev. D*, **90**, 023018

- . 2014b, *Phys. Rev. D*, **90**, 023019
- Liu, A., & Tegmark, M. 2011, *Phys. Rev. D*, **83**, 103006
- Liu, A., Tegmark, M., Bowman, J., Hewitt, J., & Zaldarriaga, M. 2009, *Monthly Notices of the Royal Astronomical Society*, **398**, 401
- Liu, A., Tegmark, M., Morrison, S., Lutomirski, A., & Zaldarriaga, M. 2010, *Monthly Notices of the Royal Astronomical Society*, **408**, 1029
- Loeb, A., & Furlanetto, S. 2013, *The First Galaxies in the Universe* (Princeton University Press)
- Lonsdale, C., J. Cappallo, R., F. Morales, M., et al. 2009, *Proceedings of the IEEE*, **97**, 1497
- Moore, D. F., Aguirre, J. E., Parsons, A. R., Jacobs, D. C., & Pober, J. C. 2013, *The Astrophysical Journal*, **769**, 154
- Morales, M. F., Bowman, J. D., & Hewitt, J. N. 2006, *The Astrophysical Journal*, **648**, 767
- Morales, M. F., & Wyithe, J. S. B. 2010, *ARA&A*, **48**, 127
- Neben, A. R., Bradley, R. F., Hewitt, J. N., et al. 2016, *The Astrophysical Journal*, **826**, 199
- Nunhokee, C. D., Bernardi, G., Kohn, S. A., et al. 2017, *The Astrophysical Journal*, **848**, 47
- Offringa, A. R., de Bruyn, A. G., & Zaroubi, S. 2012, *Monthly Notices of the Royal Astronomical Society*, **422**, 563
- Paciga, G., Albert, J. G., Bandura, K., et al. 2013a, *MNRAS*, arXiv:1301.5906 [astro-ph.CO]
- . 2013b, *MNRAS*, **433**, 639
- Padmanabhan, N., White, M., Zhou, H. H., & O'Connell, R. 2016, *MNRAS*, **460**, 1567
- Parsons, A., Pober, J., McQuinn, M., Jacobs, D., & Aguirre, J. 2012, *ApJ*, **753**, 81
- Parsons, A. R., & Backer, D. C. 2009, *The Astronomical Journal*, **138**, 219
- Parsons, A. R., Liu, A., Ali, Z. S., & Cheng, C. 2016, *ApJ*, **820**, 51
- Parsons, A. R., Pober, J. C., Aguirre, J. E., et al. 2012, *The Astrophysical Journal*, **756**, 165
- Parsons, A. R., Backer, D. C., Foster, G. S., et al. 2010, *AJ*, **139**, 1468
- Parsons, A. R., Liu, A., Aguirre, J. E., et al. 2014, *ApJ*, **788**, 106
- Patil, A. H., Yatawatta, S., Zaroubi, S., et al. 2016, *MNRAS*, **463**, 4317
- Patil, A. H., Yatawatta, S., Koopmans, L. V. E., et al. 2017, *ApJ*, **838**, 65
- Patra, N., Subrahmanyam, R., Sethi, S., Udaya Shankar, N., & Raghunathan, A. 2015, *ApJ*, **801**, 138
- Patra, N., Parsons, A. R., DeBoer, D. R., et al. 2018, *Experimental Astronomy*, **45**, 177
- Paz, D. J., & Sánchez, A. G. 2015, *MNRAS*, **454**, 4326
- Pearson, D. W., & Samushia, L. 2016, *MNRAS*, **457**, 993
- Peterson, U.-L. P. X.-P. W. J. 2004, ArXiv Astrophysics e-prints, astro-ph/0404083
- Petrovic, N., & Oh, S. P. 2011, *MNRAS*, **413**, 2103
- Planck Collaboration, Ade, P. A. R., Aghanim, N., et al. 2016, *A&A*, **594**, A13
- Pober, J. C., Parsons, A. R., Jacobs, D. C., et al. 2012, *AJ*, **143**, 53
- Pober, J. C., Parsons, A. R., Aguirre, J. E., et al. 2013, *The Astrophysical Journal Letters*, **768**, L36
- Pober, J. C., Parsons, A. R., DeBoer, D. R., et al. 2013, *AJ*, **145**, 65
- Pober, J. C., Liu, A., Dillon, J. S., et al. 2014, *ApJ*, **782**, 66
- Pober, J. C., Ali, Z. S., Parsons, A. R., et al. 2015, *ApJ*, **809**, 62

- Pober, J. C., Hazelton, B. J., Beardsley, A. P., et al. 2016, *ApJ*, 819, 8
- Pope, A. C., & Szapudi, I. 2008, *MNRAS*, 389, 766
- Pritchard, J. R., & Loeb, A. 2010, *Phys. Rev. D*, 82, 023006
- . 2012, *Reports on Progress in Physics*, 75, 086901
- Quenouille, M. H. 1949, *Ann. Math. Statist.*, 20, 355
- Robertson, B. E., Ellis, R. S., Furlanetto, S. R., & Dunlop, J. S. 2015, *ApJ*, 802, L19
- Roshi, D. A., & Perley, R. A. 2003, in Astronomical Society of the Pacific Conference Series, Vol. 306, New technologies in VLBI, ed. Y. C. Minh, 109
- Santos, M. G., Cooray, A., & Knox, L. 2005, *ApJ*, 625, 575
- Sellentin, E., & Heavens, A. F. 2016, *MNRAS*, 456, L132
- Sherwin, B. D., van Engelen, A., Sehgal, N., et al. 2017, *Phys. Rev. D*, 95, 123529
- Slatyer, T. R., & Wu, C.-L. 2018, *Phys. Rev. D*, 98, 023013
- Sokolowski, M., Tremblay, S. E., Wayth, R. B., et al. 2015, *PASA*, 32, e004
- Sullivan, I. S., Morales, M. F., Hazelton, B. J., et al. 2012, *The Astrophysical Journal*, 759, 17
- Switzer, E. R., Chang, T.-C., Masui, K. W., Pen, U.-L., & Voytek, T. C. 2015, *ApJ*, 815, 51
- Taylor, A., & Joachimi, B. 2014, *MNRAS*, 442, 2728
- Tegmark, M. 1997, *Phys. Rev. D*, 55, 5895
- Thompson, A. R., Moran, J. M., & Swenson, Jr., G. W. 2001, Interferometry and Synthesis in Radio Astronomy, 2nd Edition (Springer)
- Thyagarajan, N., Udaya Shankar, N., Subrahmanyam, R., et al. 2013, *ApJ*, 776, 6
- Thyagarajan, N., Jacobs, D. C., Bowman, J. D., et al. 2015, *The Astrophysical Journal*, 804, 14
- Tingay, S. J., Goeke, R., Bowman, J. D., et al. 2013, *PASA*, 30, 7
- Trott, C. M., Wayth, R. B., & Tingay, S. J. 2012, *ApJ*, 757, 101
- Trott, C. M., Pindor, B., Procopio, P., et al. 2016, *The Astrophysical Journal*, 818, 139
- Tukey. 1958, *Ann. Math. Statist.*, 29, 614
- van Haarlem, M. P., Wise, M. W., Gunst, A. W., et al. 2013, *A&A*, 556, A2
- Vedantham, H., Shankar, N. U., & Subrahmanyam, R. 2012, *The Astrophysical Journal*, 745, 176
- Vedantham, H. K., Koopmans, L. V. E., de Bruyn, A. G., et al. 2014, *MNRAS*, 437, 1056
- Voytek, T. C., Natarajan, A., Jáuregui García, J. M., Peterson, J. B., & López-Cruz, O. 2014, *ApJ*, 782, L9
- Wang, J., Xu, H., An, T., et al. 2013, *The Astrophysical Journal*, 763, 90
- Wang, X., Tegmark, M., Santos, M. G., & Knox, L. 2006, *ApJ*, 650, 529
- Weisz, D. R., & Boylan-Kolchin, M. 2017, *MNRAS*, 469, L83
- Wolz, L., Abdalla, F. B., Blake, C., et al. 2014, *Monthly Notices of the Royal Astronomical Society*, 441, 3271
- Wu, X. 2009, in Bulletin of the American Astronomical Society, Vol. 41, American Astronomical Society Meeting Abstracts #213, 474
- Zheng, H., Tegmark, M., Buza, V., et al. 2014, *Monthly Notices of the Royal Astronomical Society*, 445, 1084